THE MOTION OF MESOSCALE SNOWBANDS IN NORTHEAST U.S. WINTER STORMS

by

Jaymes S. Kenyon

A Thesis

Submitted to the University at Albany, State University of New York

in Partial Fulfillment of

the Requirements for the Degree of

Master of Science

College of Arts & Sciences

Department of Atmospheric and Environmental Sciences

2013

ABSTRACT

The distribution of snowfall accumulation attending winter storms is a product of both precipitation intensity and duration. Many heavy snowfall events are associated with distinct mesoscale snowbands that strongly modulate snowfall accumulation. Mesoscale snowbands are known to be favored within environments characterized by frontogenesis in the presence of weak moist symmetric or gravitational stabilities. Although the development of mesoscale snowbands often can be anticipated at 24−36-h ranges, anticipating band residence time at a fixed location remains a forecasting challenge. However, given that snowband residence time is related to characteristics of band motion, improved understanding of band motion presents an opportunity to improve snowfall accumulation forecasts.

This study investigates environmental attributes associated with specific snowband motion characteristics. A classification scheme for snowband motion is developed, wherein bands are categorized into four modes: laterally translating, laterally quasi-stationary, pivoting, and hybrid. Laterally translating bands exhibit predominantly cross-axis motion, thereby favoring quasi-uniform snowfall accumulation along their paths. In contrast, laterally quasi-stationary bands are characterized by near-zero cross-axis motion, favoring heavy snowfall accumulation along a narrow corridor that may extend for several hundred kilometers. Pivoting bands exhibit pronounced rotation such that heavy snowfall accumulation is particularly favored near the center of rotation. Finally, hybrid bands are dominated by along-axis motion, but with a concurrent cross-axis component of motion. Using archived WSR-88D data, snowband events in the

northeast U.S. between 2005 and 2010 have been subjectively identified and classified according to this scheme. Gridded data from the 0.5° resolution NCEP Climate Forecast System Reanalysis are used to identify environmental features associated with band motion characteristics.

Results indicate that patterns of the low-to-midlevel kinematic fields, temperature advection, along- and cross-isentrope projections of the *Q* vector, and vertical wind shear in the near-band environment are useful in distinguishing between snowband modes. Composite fields, case studies, and conceptual models are presented to illustrate synoptic-scale features associated with different snowband motion characteristics.

ACKNOWLEDGEMENTS

On the occasion of completing this M.S. thesis, which culminates my graduate studies, I would like to express my gratitude for the unwavering encouragement and support of my parents and family. Their love has been my greatest source of resilience in navigating each challenge during the varied chapters of my life. I am also indebted to my academic co-advisors, Profs. Dan Keyser and Lance Bosart. Not only are they exemplary scientists, but consummate teachers as well, and together have significantly fostered my development as a scientist. More importantly, they have broadened my sense of my own abilities, and for that I will always be grateful.

I also thank the faculty and staff of the UAlbany Department of Atmospheric and Environmental Sciences for their contagious enthusiasm for science and learning. Special thanks go to Ross Lazear and Kevin Tyle for their patient technical assistance. I also thank Barbara Zampella, Sandra George, Denise Church, Maria Moon, and Patti Seguin for their administrative support. Additionally, I am grateful for the friendship and camaraderie of my fellow graduate students, current and former.

My National Weather Service focal point, Mike Evans, provided very helpful advice and operational perspective during this project, as did Pete Banacos, Stacie Hanes, and Frank Nocera, who were valuable collaborators. I wish to thank Heather Archambault, Andrea Lang, Hannah Attard, and Anatha Aiyyer for their programming assistance.

I will remain ever grateful for all of my past teachers. They span my life from my early years in Eaton Rapids, Michigan, right up to graduate school, and their influence on

my life will endure always. Finally, I remember the men and women of the United States Air Force and the United States Army beside whom I was so proud and honored to serve, and with whom I will always share a special bond.

This research was supported by the National Oceanic and Atmospheric Administration (NOAA) grant NA01NWS4680002, awarded to the University at Albany, SUNY, as part of the Collaborative Science, Technology, and Applied Research (CSTAR) program.

J. S. K.

Albany, New York

December 2013

TABLE OF CONTENTS

Abstract ii

Acknowledgements iv

List of Tables viii

List of Figures ix

1. Introduction 1

1.1 Motivation 1

1.2 Literature Review 2

1.2.1 Mesoscale Precipitation Bands 2

1.2.2 Band Morphology 4

1.2.3 Band Evolution 7

1.2.4 Band Motion 11

1.3 Research Goals and Thesis Structure 13

2. Data and Methodology 20

2.1 Data Sources 20

2.2 Methodology 21

2.2.1 Snowband Identification and Categorization 21

2.2.2 Vector Frontogenesis and *Q*-vector Partitioning 25

2.2.3 Composite Analysis 29

2.2.4 Case Studies 30

2.2.5 Trajectory Calculations 30

3. Results 35

3.1 Snowband Identification and Categorization 35

3.2 Composite Analysis 35

3.2.1 Composite Members 35

3.2.2 Laterally Translating Category Composite 36

3.2.3 Laterally Quasi-Stationary Category Composite 39

3.2.4 Pivoting Category Composite 42

3.3 Case Studies 46

3.3.1 Laterally Translating Snowband 46

3.3.2 Laterally Quasi-Stationary Snowband 48

3.3.3 Pivoting Snowband 50

3.3.4 Hybrid Snowband 52

4. Discussion, Conclusions, and Suggestions for Future Work 89

4.1 Discussion 89

4.1.1 Composite Analysis 89

4.1.2 Case Studies 91

4.1.3 Diagnostic Methods 94

4.1.4 Applications of Research to Operational Forecasting 96

4.2 Conclusions 97

4.3 Suggestions for Future Work 100

References 105

Appendix 108

LIST OF TABLES

Table 1. Listing of study cases and their associated heavy snow dates.

LIST OF FIGURES

Fig. 1.1. Schematic cross section oriented normal to a frontal zone and its associated mesoscale precipitation band. Saturation equivalent potential temperature is shown by light dashed lines. The sloped region of frontogenesis is enclosed by a black ellipse, with the major axis of frontogenesis shown by a heavy dashed line and arrows denoting the sense of transverse circulation. The dash-dot region above 600 hPa encloses a region of dry advection, with the circled X indicating maximum flow into the cross section. A region of conditional instability is enclosed in a heavy dashed line on the right side of the schematic. Heavy precipitation (i.e., heavy snow) at the surface is shown by four stars along the *x*-axis [Fig. 15 in Moore et al. (2005)].

Fig. 1.2. Distribution of band axes relative to surface cyclone position (at the origin) for all single-banded events in the Novak et al. (2004) study. Radial distance is labeled in km [Fig. 4 in Novak et al. (2004)].

Fig. 1.3. Conceptual models for (a) single-banded and (b) nonbanded precipitation environments from Novak et al. (2004) [their Fig. 15].

Fig. 1.4. The Nicosia and Grumm (1999) conceptual model, describing the reduction of EPV_g* adjacent to a region of frontogenesis in the comma head region of a developing extratropical cyclone [Fig. 1.12 in Novak (2002)].

Fig. 1.5. Time series of midlevel ascent, frontogenesis, and conditional stability for a model-simulated snowband on 25–26 December 2002 [Fig. 16 in Novak et al. (2008)].

Fig. 1.6. Conceptual model depicting the life cycle of mesoscale bands in the comma head region of northeast U.S. cyclones. Environmental features before band formation, during band formation, and during band dissipation are shown in the top, middle, and bottom tiers, respectively. Panels (a), (c), and (e) are plan views; panels (b), (d), and (f) are corresponding cross-section views through end points "A" and "B." Cross-section views depict frontogenesis (red shading), potential temperature (green), upper-level jet (as labeled), and conditional instability (blue shading). Hydrometeor descent and growth are shown by snowflake symbols in (d) [Fig. 15 in Novak et al. (2010)].

Fig. 1.7. Schematic midlevel deformation paradigms of Banacos (2003), showing (a) deformation in association with strong extratropical cyclogenesis and (b) deformation in association with east–west frontal zones and weak cyclogenesis. Principle deformation zones are denoted by axes of alternating dots and x's, and scalloping denotes sense of upper-level cloud pattern. Dashed lines denote 700-hPa geopotential height. "WCB" and "CCB" in (a) indicate the warm conveyor belt and cold conveyor belt, respectively. Airmass regions are given by conventional two-letter designations. Boxed location designations are as follows: the leading "C", "N" and "W" denotes cold, neutral, and warm advection, respectively. The "c" and "f" refer to the cyclogenesis pattern in (a) or frontal pattern in (b), respectively. The numbers "1" and "2" are arbitrary designations that denote specific locations within each paradigm [Fig. 1 in Banacos (2003)].

Fig. 1.8. Schematic hodographs corresponding to the boxed locations in Fig. 1.7. "S" and "T" correspond to surface and tropopause, respectively [Fig. 3 in Banacos (2003)].

Fig. 2.1. Map showing the locations of 39 NWS first-order stations that were utilized in this study.

Fig. 2.2. Flowchart of the snowband motion classification scheme used in this study. The defining criteria for each motion category, along with schematic illustrations, are given in Fig. 2.3.

Fig. 2.3. Schematic representations of the four snowband motion categories and their defining criteria. The start of the 1-h period during which band motion is evaluated is denoted by t_0. See text for details.

Fig. 2.4. Illustration of a natural-coordinate partitioning of the Q vector into along- and cross-isentrope contributions following Keyser et al. (1988). See text for discussion.

Fig. 3.1. (a) Distribution of the 70 study cases between those with and without banded events. (b) The number of study cases across which a given banded event category was manifested. (c) The distribution of banded events by category, summed across all study cases.

Fig. 3.2. Laterally translating category composite (N = 17) (a) MSLP (black contours, hPa), 1000–500-hPa thickness (dashed contours, dam), and 250-hPa wind speed (fills, m s^{-1}); (b) 850–700-hPa layer-mean streamlines (black contours), temperature (red contours, °C), axes of dilatation [purple tick marks, length scaled by resultant deformation, reference axis (5×10^{-5} s^{-1}) at top right], and Petterssen frontogenesis [fills, K $(100\ km)^{-1}$ $(3\ h)^{-1}$]; (c) as in (b), except for the 700–500-hPa layer. In all panels, the heavy black dot marks the composite band centroid.

Fig. 3.3. Laterally translating category composite (N = 17) geopotential height (black contours, dam), temperature (red contours, °C), and relative humidity (fills, percent w.r.t. water, ice, or mixed phase, as determined by CFSR) at (a) 850 hPa; (b) 700 hPa; (c) 600 hPa; (d) 500 hPa; (e) 400 hPa; and (f) 300 hPa. In all panels, the heavy black dot marks the composite band centroid.

Fig. 3.4. Laterally translating category composite (N = 17) layer-mean streamlines (black contours), temperature (green contours, °C), and temperature advection [fills, K $(3\ h)^{-1}$] for the (a) 850–700-hPa layer and (b) 700–500-hPa layer. In both panels, the heavy black dot marks the composite band centroid.

Fig. 3.5. Profile at the band centroid of the laterally translating category composite (N = 17) plotted on a skew T–log$p$ diagram. Orange isotherms outline the dendritic growth zone (DGZ, defined as the layer of near-saturation between the −12 and −18°C isotherms). The associated hodograph is inset at top right with the curve labeled in km

MSL and the axes labeled in kt. Corresponding wind barbs (standard convention, in kt) are shown at right.

Fig. 3.6. Laterally translating category composite (N = 17) 700–500-hPa layer-mean (a) Q vectors (arrows, magnitudes $\geq 1 \times 10^{-10}$ K m^{-1} s^{-1}, reference vector at bottom right), Q-vector divergence (fills, 10^{-16} K m^{-2} s^{-1}), streamfunction (black contours, 10^6 m^2 s^{-1}), and temperature (green contours, °C); (b) as in (a) except for Q_s vectors; (c) as in (a), except for Q_n vectors; (d)–(f) as in (a)–(c), respectively, except for the 850–700-hPa layer mean. In all panels, the heavy dot (green or purple) marks the composite band centroid.

Fig. 3.7. Laterally translating category composite (N = 17) (a) 700–500-hPa layer-mean normalized Q_s (fills, 10^{-6} s^{-1}), temperature (dashed green contours, °C), and streamfunction (black contours, 10^6 m^2 s^{-1}); (b) as in (a), except for normalized Q_n; (c) and (d) as in (a) and (b), respectively, except for the 850–700-hPa layer mean. In all panels, the heavy black dot marks the composite band centroid.

Fig. 3.8. Laterally translating category composite (N = 17) 24-h backward kinematic trajectories arriving along the mean band axis at (a) 700 hPa and (b) 500 hPa. Trajectory pressure (hPa) is shown according to color bar.

Fig. 3.9. As in Fig. 3.2, except for the laterally quasi-stationary category composite (N = 8).

Fig. 3.10. As in Fig. 3.3, except for the laterally quasi-stationary category composite (N = 8).

Fig. 3.11. As in Fig. 3.4, except for the laterally quasi-stationary category composite (N = 8).

Fig. 3.12. As in Fig. 3.5, except for the laterally quasi-stationary category composite (N = 8).

Fig. 3.13. As in Fig. 3.6, except for the laterally quasi-stationary category composite (N = 8).

Fig. 3.14. As in Fig. 3.7, except for the laterally quasi-stationary category composite (N = 8).

Fig. 3.15. As in Fig. 3.8, except for the laterally quasi-stationary category composite (N = 8).

Fig. 3.16. As in Fig. 3.2, except for the pivoting category composite (N = 18). In all panels, the heavy black dot marks the composite pivot zone.

Fig. 3.17. As in Fig. 3.3, except for the pivoting category composite (N = 18). In all panels, the heavy black dot marks the composite pivot zone.

Fig. 3.18. As in Fig. 3.4, except for the pivoting category composite (N = 18). In both panels, the heavy black dot marks the composite pivot zone.

Fig. 3.19. As in Fig. 3.5, except for the pivoting category composite (N = 18).

Fig. 3.20. As in Fig. 3.6, except for the pivoting category composite (N = 18). In all panels, the heavy green dot marks the composite pivot zone.

Fig. 3.21. As in Fig. 3.7, except for the pivoting category composite (N = 18). In all panels, the heavy black dot marks the composite pivot zone.

Fig. 3.22. As in Fig. 3.8, except for the pivoting category composite (N = 18).

Fig. 3.23. Radar reflectivity (dB*Z*) at 0600 UTC 9 Dec 2009. Dash–dot pattern denotes the axis of the laterally translating snowband discussed in the text. The axis of the same snowband 1 h before (1 h after) the mosaic time is shown in dashed black (dashed red), as labeled.

Fig. 3.24. 24-h snowfall accumulation (cm) ending at 1200 UTC 9 Dec 2009.

Fig. 3.25. As in Fig. 3.2, except at 0600 UTC 9 Dec 2009. The reference axis of dilatation (top right) represents resultant deformation of $10 \times 10^{-5}\ s^{-1}$. In all panels, the heavy black dot marks the centroid of the laterally translating snowband.

Fig. 3.26. As in Fig. 3.3, except at 0600 UTC 9 Dec 2009. In all panels, the heavy black dot marks the centroid of the laterally translating snowband.

Fig. 3.27. As in Fig. 3.4, except at 0600 UTC 9 Dec 2009. In both panels, the heavy black dot marks the centroid of the laterally translating snowband.

Fig. 3.28. As in Fig. 3.5, except at the centroid of the laterally translating snowband at 0600 UTC 9 Dec 2009. Centroid location is shown by black dots in Figs. 3.25–3.27.

Fig. 3.29. As in Fig. 3.6, except at 0600 UTC 9 Dec 2009. *Q* vectors with magnitudes $\geq 2 \times 10^{-10}\ K\ m^{-1}\ s^{-1}$ are plotted. In all panels, the heavy dot (green or purple) marks the centroid of the laterally translating snowband.

Fig. 3.30. As in Fig. 3.8, except for parcels arriving along the laterally translating snowband at 0600 UTC 9 Dec 2009.

Fig. 3.31. Radar reflectivity (dB*Z*) at 0600 UTC 2 Mar 2009. Dash–dot pattern denotes the axis of the laterally quasi-stationary snowband discussed in the text. The axis of the same snowband 1 h before (1 h after) the mosaic time is shown in dashed black (dashed red), as labeled.

Fig. 3.32. 24-h snowfall accumulation (cm) ending at 1200 UTC 2 Mar 2009.

Fig. 3.33. As in Fig. 3.2, except at 0600 UTC 2 Mar 2009. The reference axis of dilatation (top right) represents resultant deformation of $10 \times 10^{-5}\ s^{-1}$. In all panels, the heavy black dot marks the centroid of the laterally quasi-stationary snowband.

Fig. 3.34. As in Fig. 3.3, except at 0600 2 Mar 2009. In all panels, the heavy black dot marks the centroid of the laterally quasi-stationary snowband.

Fig. 3.35. As in Fig. 3.4, except at 0600 2 Mar 2009. In both panels, the heavy black dot marks the centroid of the laterally quasi-stationary snowband.

Fig. 3.36. As in Fig. 3.5, except at the centroid of the laterally quasi-stationary snowband at 0600 UTC 2 Mar 2009. Centroid location is shown by black dots in Figs. 3.33–3.35.

Fig. 3.37. As in Fig. 3.6, except at 0600 UTC 2 Mar 2009. Q vectors with magnitudes $\geq 2 \times 10^{-10}$ K m^{-1} s^{-1} are plotted. In all panels, the heavy pink dot marks the centroid of the laterally quasi-stationary snowband.

Fig. 3.38. As in Fig. 3.8, except for parcels arriving along the laterally quasi-stationary snowband at 0600 UTC 2 Mar 2009.

Fig. 3.39. Radar reflectivity (dBZ) at 1200 UTC 12 Feb 2006. Dash–dot pattern denotes the axis of the pivoting snowband discussed in the text. The axis of the same snowband 2 h before (2 h after) the mosaic time is shown in dashed black (dashed red), as labeled. The pivot zone (labeled "PZ") at 1200 UTC is encircled in black.

Fig. 3.40. 24-h snowfall accumulation (cm) ending at 1800 UTC 12 Feb 2006.

Fig. 3.41. As in Fig. 3.2, except at 1200 UTC 12 Feb 2006. The reference axis of dilatation (top right) represents resultant deformation of 10×10^{-5} s^{-1}. In all panels, the heavy black dot marks the pivot zone of the pivoting snowband.

Fig. 3.42. As in Fig. 3.3, except at 1200 UTC 12 Feb 2006. In all panels, the heavy black dot marks the pivot zone of the pivoting snowband.

Fig. 3.43. As in Fig. 3.4, except at 1200 UTC 12 Feb 2006. In both panels, the heavy black dot marks the pivot zone of the pivoting snowband.

Fig. 3.44. As in Fig. 3.5, except at the pivot zone of the pivoting snowband at 1200 UTC 12 Feb 2006. Pivot zone location is shown by black dots in Figs. 3.41–3.43.

Fig. 3.45. As in Fig. 3.6, except at 1200 UTC 12 Feb 2006. Q vectors with magnitudes $\geq 2 \times 10^{-10}$ K m^{-1} s^{-1} are plotted. In all panels, the heavy pink dot marks the pivot zone of the pivoting snowband.

Fig. 3.46. As in Fig. 3.8, except for parcels arriving along the pivoting snowband at 1200 UTC 12 Feb 2006.

Fig. 3.47. Radar reflectivity (dBZ) at 1200 UTC 12 Dec 2008. Dash–dot pattern denotes the axis of the hybrid snowband discussed in the text. The axis of the same snowband 1 h before (1 h after) the mosaic time is shown in dashed black (dashed red), as labeled.

Fig. 3.48. 24-h snowfall accumulation (cm) ending at 1800 UTC 12 Dec 2008.

Fig. 3.49. As in Fig. 3.2, except at 1200 UTC 12 Dec 2008. The reference axis of dilatation (top right) represents resultant deformation of $10 \times 10^{-5}\ s^{-1}$. In all panels, the heavy black dot marks the centroid of the hybrid snowband.

Fig. 3.50. As in Fig. 3.3, except at 1200 UTC 12 Dec 2008. In all panels, the heavy black dot marks the centroid of the hybrid snowband.

Fig. 3.51. As in Fig. 3.4, except at 1200 UTC 12 Dec 2008. In both panels, the heavy black dot marks the centroid of the hybrid snowband.

Fig. 3.52. As in Fig. 3.5, except at the centroid of the hybrid snowband at 1200 UTC 12 Dec 2008. Centroid location is shown by black dots in Figs. 3.49–3.51.

Fig. 3.53. As in Fig. 3.6, except at 1200 UTC 12 Dec 2008. Q vectors with magnitudes $\geq 2 \times 10^{-10}\ K\ m^{-1}\ s^{-1}$ are plotted. In all panels, the heavy pink dot marks the centroid of the hybrid snowband.

Fig. 3.54. As in Fig. 3.8, except for parcels arriving along the hybrid snowband at 1200 UTC 12 Dec 2008.

Fig. 4.1. Conceptual models for (a) laterally translating snowbands, (b) laterally quasi-stationary snowbands, and (c) pivoting snowbands. Features are shown according to keys accompanying each panel; other symbols are conventional. Sense of band motion is shown by grey arrows in (a) and (b). "PZ" in (c) denotes pivot zone location, and encircling grey arrow indicates sense of band rotation. Note that streamlines and frontogenesis are depicted for the 850–700-hPa layer in (a) and (c), but for the 700–500-hPa layer in (b). In each panel, hodographs at locations marked "X" are shown at bottom right, where "S" and "T" correspond to surface and tropopause, respectively.

1. Introduction

1.1 Motivation

In the most rudimentary sense, quantitative precipitation forecasting requires assessment of the expected *rate* and *duration* of precipitation (Doswell et al. 1996). Cold-season precipitation in the northeast U.S. frequently exhibits mesoscale organization (e.g., Novak et al. 2004; Greenstein 2006) such that mesoscale precipitation features may significantly modulate precipitation accumulation. A particular mode of mesoscale precipitation organization, so-called *mesoscale precipitation bands* (or *mesoscale banded precipitation*), is commonly observed in conjunction with northeast U.S. cyclones (Novak et al. 2004; Greenstein 2006). Although the likelihood of mesoscale precipitation band development can often be ascertained at 24–48-h forecast ranges, quantitative forecasts of band-attributable precipitation can be difficult beyond 12 h (Novak et al. 2006, 2010; Evans and Jurewicz 2009). Thus, the limited predictability of mesoscale precipitation bands poses a particular operational forecasting challenge.

Mesoscale precipitation bands are distinguished by precipitation organized along coherent, quasi-linear horizontal axes, and therefore exhibit inherently high aspect ratios (length-to-width) in plan-view radar reflectivity observations. Because of this intrinsic geometry of mesoscale precipitation bands, the geographic distribution of precipitation accumulation may be strongly influenced by band motion characteristics. That is, for a band of a given intensity, shape, and size, the relative magnitudes of along- and cross-axis speed will influence whether pronounced precipitation accumulation gradients are likely. In cases of significant cross-axis band motion, a relatively uniform geographic

distribution of band-attributable precipitation is favored, as band residence time over traversed locations will tend to be relatively brief. In contrast, small cross-axis band motion will favor a sharp gradient of precipitation accumulation, as band residence time will be prolonged along an axis-parallel corridor.

The foregoing considerations of the predictability of mesoscale precipitation bands and the significance of their motion characteristics suggest a scientific opportunity. Whereas quantitative forecasts of banded precipitation accumulation may be difficult at medium forecast ranges (i.e., 12 h and beyond), the characteristic *distribution* of banded precipitation accumulation (i.e., spatially uniform or spatially varying) may be predictable at these medium forecast ranges if band motion attributes can be linked to synoptic- and sub-synoptic-scale features. Forecaster anticipation of band motion characteristics may help inform warning decisions and may also aid in the identification of meteorological situations that are particularly prone to errors in precipitation accumulation forecasts. Thus, a specialized treatment of mesoscale precipitation band motion may be beneficial for operational forecasting interests, and therefore motivates this research.

1.2 Literature Review

1.2.1 Mesoscale Precipitation Bands

A considerable body of theoretical, observational, and idealized modeling studies has demonstrated that mesoscale precipitation bands are attributable to frontogenesis in the presence of weak moist symmetric stability (e.g., Emanuel 1985; Sanders and Bosart

1985; Thorpe and Emanuel 1985; Xu 1992; Moore and Lambert 1993; Nicosia and Grumm 1999; Novak et al. 2004; Moore et al. 2005). The dynamical basis for this linkage is contained in the so-called Sawyer–Eliassen equation (Sawyer 1956; Eliassen 1962), which describes the transverse ageostrophic circulation that arises in response to frontogenesis when the basic-state flow is constrained by approximate thermal wind balance. By intensifying (weakening) the horizontal temperature gradient, frontogenesis (frontolysis) perturbs the environment from thermal wind balance, yielding a thermally direct (indirect) transverse circulation in a plane normal to the thermal wind (i.e., approximately normal to the frontal zone). The vertical and horizontal branches of this circulation, linked by mass continuity, act to readjust the mass and momentum distribution back towards a state of thermal wind balance through adiabatic temperature adjustments and ageostrophic horizontal accelerations. The ascending branch of this circulation is of particular interest, where precipitation production (or enhancement) may occur within an elongated region approximately parallel to the thermal wind. Thus, mesoscale precipitation bands are manifestations of ageostrophic circulations that are forced by frontogenesis, as illustrated schematically in Fig. 1.1. Note that other forms of mesoscale precipitation may exhibit band-like characteristics, such as lake-effect precipitation and orographically forced precipitation. However, this research is concerned only with mesoscale precipitation bands that are associated with frontogenesis.

According to the Sawyer–Eliassen equation, the environmental symmetric stability (as encapsulated by the dry or moist potential vorticity) serves to modulate the strength of the transverse ageostrophic circulation that arises in response to frontogenesis. Emanuel (1985) demonstrated that when symmetric stability is small on the warm side of

a frontogenesis axis relative to the cold side, the ascending (descending) branches of the circulation are horizontally narrow (broad), thereby yielding a transverse circulation with a concentrated, intense updraft. The idealized modeling study of Xu (1992) suggested that regions of negative moist potential vorticity (associated with moist symmetric instability) in viscous semigeostrophic flow favor the development of multiple finescale front-parallel updrafts as opposed to single updrafts. The role of symmetric stability in modulating the atmospheric response to frontogenesis within the framework of the Sawyer–Eliassen equation is further emphasized in the review of Schultz and Schumacher (1999), who note that forced slantwise ascent from frontogenesis can yield mesoscale precipitation bands even when the atmosphere is stable to moist slantwise parcel displacements. Note that moist gravitational instabilities (i.e., conditional instability and potential instability) are special cases of moist symmetric instabilities (i.e., conditional symmetric instability and potential symmetric instability, respectively), as discussed by Schultz and Schumacher (1999).

1.2.2 Band Morphology

Numerous observational studies have examined the occurrence of mesoscale precipitation bands in relation to larger-scale features. Using radar reflectivity observations, Houze et al. (1976) documented mesoscale rainbands in association with 11 extratropical cyclones in the Pacific Northwest, and suggested that mesoscale precipitation bands are common substructures of extratropical cyclones worldwide. Further, Houze et al. (1976) developed a six-category band classification scheme that

categorized bands according to their location with respect to surface fronts and found a tendency for rainbands to be oriented approximately parallel to surface fronts.

Martin (1998a,b) analyzed an intense mesoscale snowband that developed in the comma head region of a moderately strong, warm-occluded continental cyclone. Drawing from the "three front model" of the Canadian Meteorological Service (Galloway 1958, 1960), Martin (1998a,b) identified a "trough of warm air aloft" (or *trowal*) within the warm-occluded region of the cyclone, distinguished by a sloping wedge of high equivalent potential temperature (θ_e) air wrapped around the cyclone. Despite the unremarkable cyclone intensity [attaining a minimum mean sea level pressure (MSLP) of ~997 hPa], Martin (1998b) found that strong frontogenesis along the warm-frontal region of the cyclone yielded intense mesoscale ascent of high-θ_e air along the trowal axis, thereby contributing to a band of heavy snow. Martin (1998a) also suggested that an upper-level "treble clef" (or "hook") horizontal potential vorticity (PV) distribution is sufficient to infer the presence of a warm occlusion and associated trowal, although a trowal may also be present in nonoccluded cyclones. For example, Moore (2005) investigated a heavy mesoscale snowband associated with a trowal in a nonoccluded cyclone. Similar to Martin (1998a,b), Moore (2005) attributed the snowband to a zone of robust ascent along a trowal axis immediately adjacent to a midlevel frontogenesis region.

Jurewicz and Evans (2004) analyzed two eastern U.S. snowstorms that exhibited pronounced mesoscale snowbands within dissimilar synoptic environments. The first case (6–7 January 2002) featured a prominent snowband and weaker finescale bands embedded within a region of moderate nonbanded precipitation. This case was

associated with strong quasigeostrophic (QG) forcing for ascent and rapid cyclogenesis. The second case (19–20 January 2002) exhibited a single snowband embedded within a broken area of light nonbanded precipitation and was associated with modest QG forcing for ascent and weak cyclogenesis. Despite these synoptic-scale environmental differences, Jurewicz and Evans (2004) found that frontogenesis and weak moist symmetric stability were common environmental attributes of both events. Thus, as with the aforementioned case studies of Martin (1998a,b) and Moore (2005), Jurewicz and Evans (2004) demonstrated that rapid cyclogenesis is not required for the development of mesoscale precipitation bands.

Using the comprehensive observational dataset afforded by the modern WSR-88D radar network, Novak (2002) conducted a climatological and composite study of mesoscale precipitation bands in northeast U.S. extratropical cyclones. Influenced by the rainband classification scheme of Houze et al. (1976), Novak (2002) developed a band classification scheme by which mesoscale precipitation bands spanning five cold seasons were categorized according to their radar reflectivity presentation. Although the most commonly observed bands in this scheme, so-called "single bands," were found to occur most frequently in the comma head region of cyclones, single bands were also observed in other cyclone-relative locations, as shown in Fig. 1.2. Regardless of the cyclone-relative locations of single bands, composites of single-banded events exhibited deep-layer frontogenesis and weak moist symmetric stability, suggesting that single bands were generally forced by transverse ageostrophic circulations resulting from frontogenesis (Novak 2002). In general, single-banded events were associated with relatively deep cyclones (in terms of MSLP and vertical extent) beneath dual upper-level

jet structures, with the bands tending to align with the characteristic "S"-shaped horizontal thermal structure of the disturbance (Novak 2002), similar to the finding of Houze et al. (1976) for Pacific Northwest cyclones and consistent with the predictions of the Sawyer–Eliassen equation (Novak 2002).

Novak (2002) retained nonbanded precipitation events for comparative assessment against single-banded events. Although nonbanded precipitation events also exhibited regions of midlevel frontogenesis, the frontogenesis in nonbanded precipitation events tended to be weaker, more gently sloped in the vertical, and embedded in greater conditional stability than single-banded events (Novak 2002). Nonbanded precipitation events also were generally found to be associated with relatively weak and shallow cyclones in advance of confluent midlevel troughs and beneath the equatorward entrance regions of downstream upper-level jets. These large-scale environmental distinctions between single-banded and nonbanded precipitation events are summarized by the Novak (2002) conceptual models shown in Figs. 1.3a and 1.3b, respectively.

1.2.3 Band Evolution

Given that the fundamental dynamical processes leading to mesoscale precipitation bands are relatively well understood, and a variety of large-scale environmental contexts associated with bands have been extensively documented, several recent studies have investigated the life cycles of mesoscale precipitation bands. In particular, characterizing the evolution of mesoscale precipitation bands in relation to changes in forcing and stability has been an objective of contemporary research.

In an analysis of three northeast U.S. snowstorms with mesoscale snowbands in the cyclone comma head region, Nicosia and Grumm (1999) found that band development coincided with the intensification of midlevel frontogenesis and the reduction of geostrophic saturation equivalent PV (EPV_g*) to strongly negative values. Drawing from the results of Bennetts and Hoskins (1979), who demonstrated that equivalent PV (EPV) is reduced following the flow when the thermal wind vector projects along the three-dimensional moisture gradient, Nicosia and Grumm (1999) proposed a conceptual model for the reduction of EPV_g* along the dry slot–comma head interface of developing cyclones (Fig. 1.4). Nicosia and Grumm (1999) suggested that band development occurs when EPV_g* becomes significantly reduced adjacent to a zone of midlevel frontogenesis. Moreover, they proposed that a positive feedback exists between frontogenesis and moist symmetric stability, as follows: (1) Frontogenesis forces a secondary circulation that intensifies the vertical wind shear. (2) In turn, increased vertical wind shear spurs an increase in differential horizontal moisture advection within the region where the cyclone dry slot overruns the moist, low-level cold conveyor belt (Carlson 1980), decreasing the conditional stability [i.e., steepening surfaces of saturation equivalent potential temperature (θ_{es})] in this region. (3) Additionally, increased vertical wind shear necessitates a decrease in inertial stability (i.e., the flattening of geostrophic absolute momentum surfaces). (4) Simultaneous reductions in both conditional stability and inertial stability necessitate a reduction in conditional symmetric stability (and EPV_g*). (5) Reduced conditional symmetric stability yields increased ascent, thereby increasing the low-level convergence, further increasing the frontogenesis in (1) above. From this synergistic frontogenesis–stability

relationship, Nicosia and Grumm (1999) hypothesized that EPV_g* could attain strongly negative values such that long-lived mesoscale precipitation bands could be maintained. As the parent cyclone matured, Nicosia and Grumm (1999) postulated that the attendant mesoscale precipitation band would become displaced from the zone of EPV_g* reduction, such that the band would deplete environmental moist symmetric instability and dissipate.

Novak et al. (2008) utilized high-resolution observations and model simulations to investigate the evolution of an intense mesoscale snowband over the northeast U.S. on 25–26 December 2002. They found that conditional instability was present ~1.5 h *prior* to band formation, and that band formation was followed by increases in both frontogenesis and conditional stability (Fig. 1.5). Furthermore, maximum ascent occurred during band formation, with increased stability likely tempering the transverse ageostrophic circulation thereafter. Band dissipation was found to occur as frontogenesis weakened in the cyclone comma head region, coincident with a reduction in midlevel deformation as the parent cyclone matured. Interestingly, Novak et al. (2008) observed only slightly negative saturation equivalent PV (EPV*) throughout the band evolution, a finding which may appear to contrast with Nicosia and Grumm (1999), who observed strongly negative EPV_g* during band formation. However, Novak et al. (2008) note that EPV*, calculated from the total wind, is less susceptible to attaining strongly negative values than EPV_g*.

Motivated by the conclusions of Novak et al. (2008), Novak et al. (2009) reexamined the 25–26 December 2002 snowstorm along with two other northeast U.S. cyclones that exhibited mesoscale snowbands in the comma head. Using piecewise PV

inversion, band formation and dissipation in all three cases were found to occur in conjunction with changes in frontogenesis induced by diabatic PV anomalies resulting from latent heat release. Further, in agreement with Novak et al. (2008), conditional stability attained minimum values prior to band formation for all cases. The antecedent stability reduction was attributed to differential horizontal temperature advection occurring away from the dry slot region, rather than differential horizontal moisture advection in the vicinity of the dry slot as proposed by Nicosia and Grumm (1999). Band formation was generally followed by a period of stabilization, and band dissipation was attributed to the emergence of diabatic PV anomalies that reduced deformation and frontogenesis, similar to the results of Novak et al. (2008)

Novak et al. (2010) conducted a composite analysis of 36 mesoscale precipitation band events that occurred in cyclone comma head regions. Consistent with Novak et al. (2008) and Novak et al. (2009), a general band life cycle was found and was tied to common evolutions in midlevel frontogenesis and stability. Prior to band formation, conditional stability was generally found to decrease as midlevel frontogenesis intensified. The increase in frontogenesis was linked to the emergence of an inverted midlevel geopotential height trough beneath the western flank of a developing upper-level PV hook (Figs. 1.6a,c and b,d). As emphasized by Martin (1998a,b), the PV hook heralds the development of a warm occlusion and associated trowal. During band formation, mesoscale precipitation bands were generally found along a midlevel frontogenesis region near a trowal axis and PV hook (Figs. 1.6c,d). Further, during band formation, Novak et al. (2010) found that conditional symmetric instability was less common than conditional instability in the cyclone comma head. The growth of diabatic

PV anomalies east of the band induced a kinematic field that reduced frontogenesis amid stronger conditional stability, leading to band dissipation (Figs. 1.6e,f).

1.2.4 Band Motion

The topic of band evolution concerns temporal changes in band structure and intensity. Closely related—and complementary—to band evolution is *band motion*, which concerns temporal changes in band position. Motivation for the topic of band motion was provided in section 1.1; this section will summarize results from literature that pertain to band motion.

Several studies have suggested that mesoscale precipitation bands behave like material bodies that are advected by the ambient environmental flow. For example, in their study of rainbands over the Pacific Northwest, Houze et al. (1976) observed that bands tended to move with the mean flow in the 850–700-hPa layer. Drawing from linear perturbation theory of symmetric instability, Seltzer et al. (1985) hypothesized that mesoscale precipitation bands will tend to move with the mean cross-band component of the flow, and observed this motion in sample of bands over the northeast U.S. [see also Schultz and Schumacher (1999), their section 6].

Given the association between mesoscale precipitation bands, frontogenesis, and deformation, Banacos (2003) proposed a linkage between the motion of large-scale deformation zones and the motion of their attendant mesoscale precipitation bands. Specifically, Banacos (2003) hypothesized that regions of frontogenesis within deformation zones that translate in a direction across their axes of dilatation will favor

cross-axis band motion and relatively brief banded precipitation at a fixed location. Conversely, regions of frontogenesis within nontranslating deformation zones will favor quasi-stationary mesoscale precipitation bands that yield distinct precipitation accumulation gradients. Banacos (2003) described two major paradigms of large-scale deformation and suggested that nontranslating deformation zones may occur with either paradigm, namely: (1) deformation occurring with strong extratropical cyclogenesis (Fig. 1.7a) and (2) deformation occurring within east–west frontal zones with minimal surface cyclogenesis (Fig. 1.7b). In both paradigms, Banacos (2003) emphasized that nontranslating deformation zones are frequently associated with distinct midlevel col regions that are characterized by straight hodographs that intercept the origin with implied deep-layer neutral temperature advection (e.g., the hodographs labeled "Nc" and "Nf" in Fig. 1.8). Thus, Banacos (2003) suggested that vertical wind profiles are useful in identifying regions where locally persistent mesoscale precipitation bands are favored.

In a study of mesoscale precipitation bands in northeast U.S. winter storms, Novak (2002) noted that 62% of single bands in the northwest quadrants of cyclones exhibited a distinct "pivot point," with the bands having rotated as they translated with the parent system. This pivot point was shown to be a favored region for heavy precipitation accumulation, where band residence time was locally prolonged. Further, single bands in the northeast and southeast quadrants (see Fig. 1.2) tended to move with the midlevel environmental flow (Novak 2002). Novak (2002) found a good correspondence between band motion and the evolution of the midlevel frontogenesis field, but suggested that additional analysis of pivoting band motion should be considered in future research for the benefit of operational forecasting interests.

1.3 Research Goals and Thesis Structure

The overarching goal of this research is to improve forecasts of heavy snowfall events in the northeast U.S. To this end, this research will investigate synoptic and mesoscale features associated with various snowband motion characteristics and will emphasize diagnostic fields that are routinely available to operational meteorologists.

This study will begin by amassing a suitable body of study cases (i.e., heavy snow-producing weather systems), which, when coupled with radar reflectivity observations and gridded reanalysis data, will provide a basis for further analysis. A classification scheme that accounts for important snowband motion distinctions will be proposed, from which a systematic categorization of the study cases will follow. Using the categorized mesoscale snowband events, composite calculations will permit the identification of common environmental attributes associated with each category. Case study analysis will be presented to supplement the results of the composite analysis. Finally, results will be synthesized into conceptual models with the aim of aiding forecasters in assessing impending heavy snow situations and making important distinctions concerning likely snowband motion and its effect on snowfall accumulation.

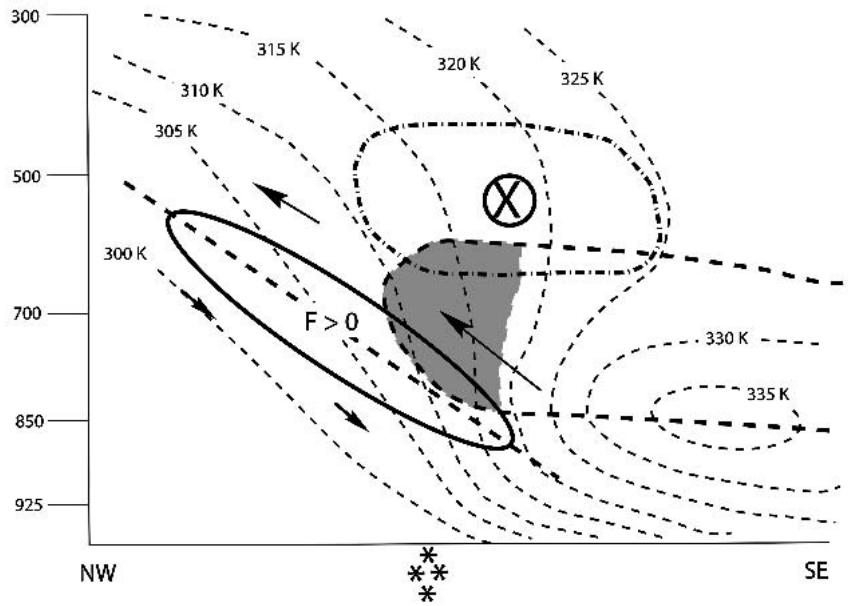

Fig. 1.1. Schematic cross section oriented normal to a frontal zone and its associated mesoscale precipitation band. Saturation equivalent potential temperature is shown by light dashed lines. The sloped region of frontogenesis is enclosed by a black ellipse, with the major axis of frontogenesis shown by a heavy dashed line and arrows denoting the sense of transverse circulation. The dash-dot region above 600 hPa encloses a region of dry advection, with the circled X indicating maximum flow into the cross section. A region of conditional instability is enclosed in a heavy dashed line on the right side of the schematic. Heavy precipitation (i.e., heavy snow) at the surface is shown by four stars along the *x*-axis [Fig. 15 in Moore et al. (2005)].

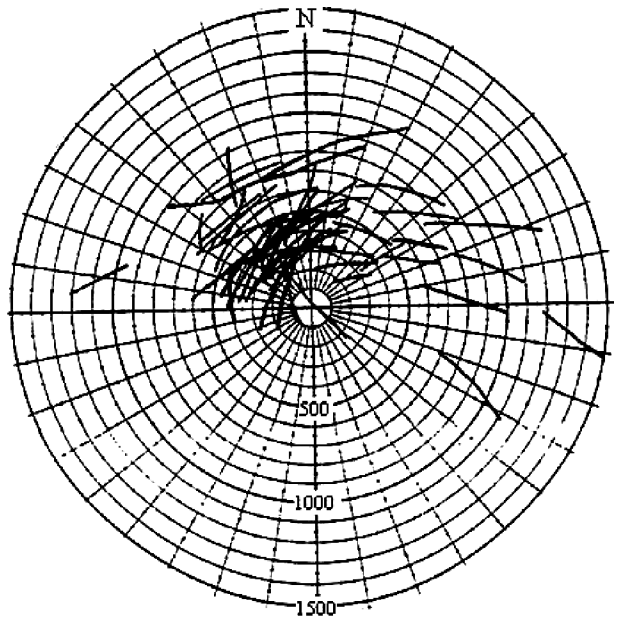

Fig. 1.2. Distribution of band axes relative to surface cyclone position (at the origin) for all single-banded events in the Novak et al. (2004) study. Radial distance is labeled in km [Fig. 4 in Novak et al. (2004)].

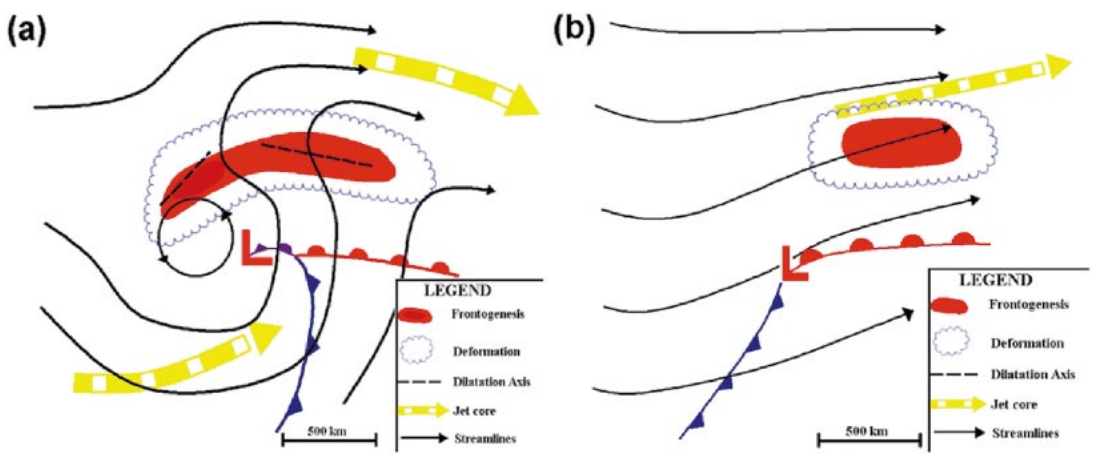

Fig. 1.3. Conceptual models for (a) single-banded and (b) nonbanded precipitation environments from Novak et al. (2004) [their Fig. 15].

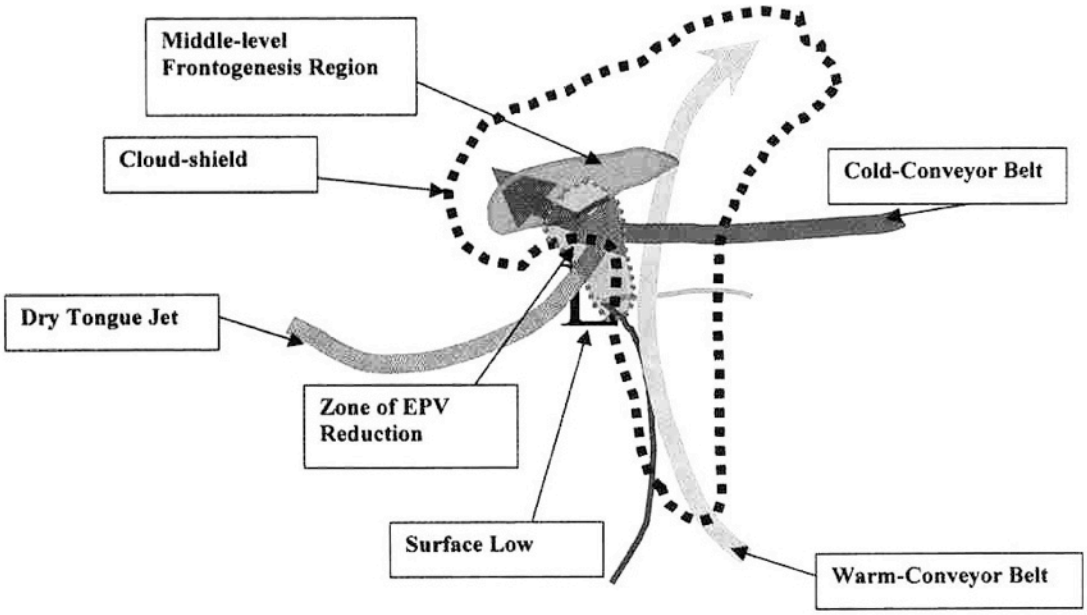

Fig. 1.4. The Nicosia and Grumm (1999) conceptual model, describing the reduction of EPV_g* adjacent to a region of frontogenesis in the comma head region of a developing extratropical cyclone [Fig. 1.12 in Novak (2002)].

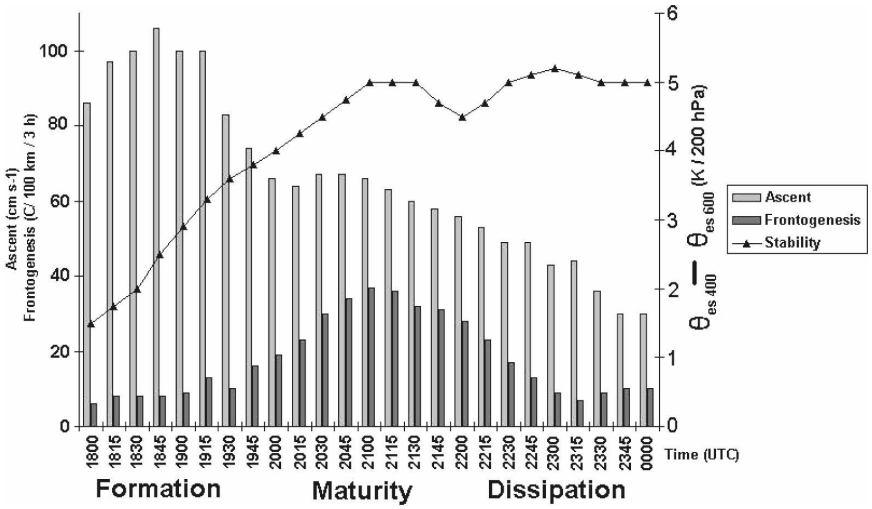

Fig. 1.5. Time series of midlevel ascent, frontogenesis, and conditional stability for a model-simulated snowband on 25–26 December 2002 [Fig. 16 in Novak et al. (2008)].

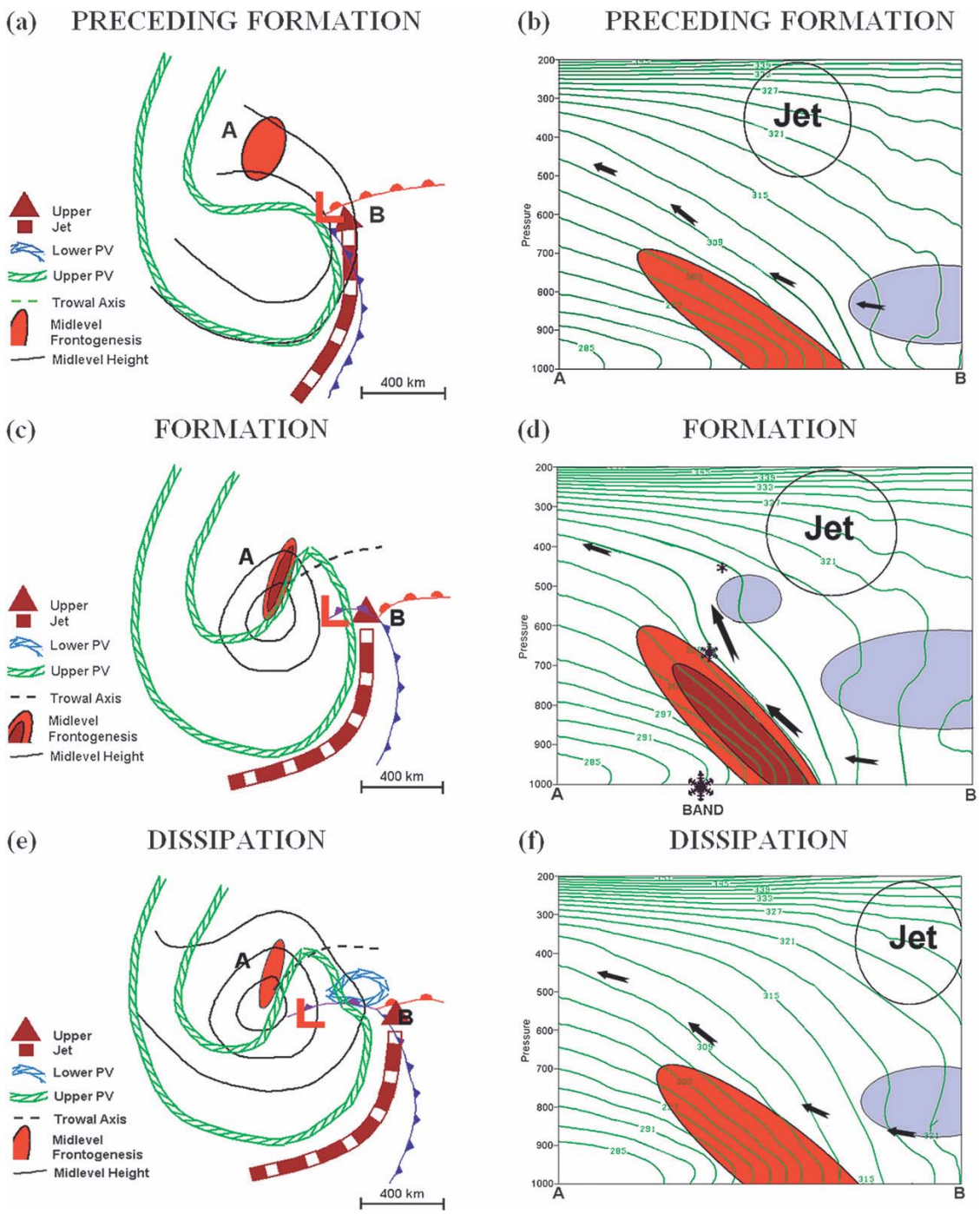

Fig. 1.6. Conceptual model depicting the life cycle of mesoscale bands in the comma head region of northeast U.S. cyclones. Environmental features before band formation, during band formation, and during band dissipation are shown in the top, middle, and bottom tiers, respectively. Panels (a), (c), and (e) are plan views; panels (b), (d), and (f) are corresponding cross-section views through end points "A" and "B." Cross-section views depict frontogenesis (red shading), potential temperature (green), upper-level jet (as labeled), and conditional instability (blue shading). Hydrometeor descent and growth are shown by snowflake symbols in (d) [Fig. 15 in Novak et al. (2010)].

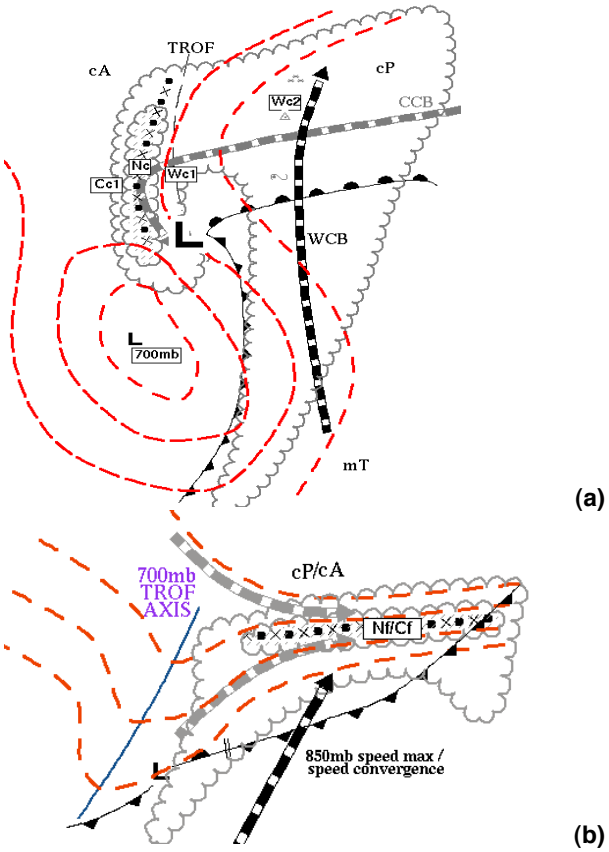

Fig. 1.7. Schematic midlevel deformation paradigms of Banacos (2003), showing (a) deformation in association with strong extratropical cyclogenesis and (b) deformation in association with east–west frontal zones and weak cyclogenesis. Principle deformation zones are denoted by axes of alternating dots and x's, and scalloping denotes sense of upper-level cloud pattern. Dashed lines denote 700-hPa geopotential height. "WCB" and "CCB" in (a) indicate the warm conveyor belt and cold conveyor belt, respectively. Airmass regions are given by conventional two-letter designations. Boxed location designations are as follows: the leading "C", "N" and "W" denotes cold, neutral, and warm advection, respectively. The "c" and "f" refer to the cyclogenesis pattern in (a) or frontal pattern in (b), respectively. The numbers "1" and "2" are arbitrary designations that denote specific locations within each paradigm [Fig. 1 in Banacos (2003)].

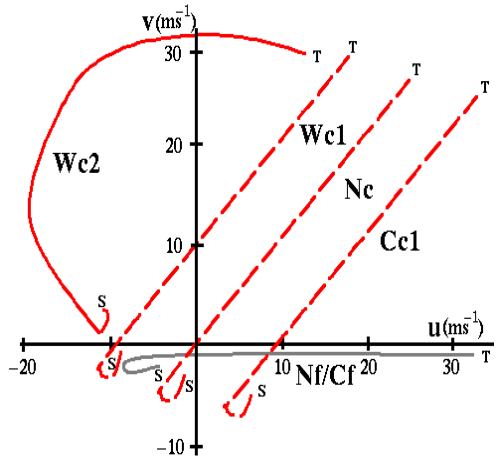

Fig. 1.8. Schematic hodographs corresponding to the boxed locations in Fig. 1.7. "S" and "T" correspond to surface and tropopause, respectively [Fig. 3 in Banacos (2003)].

2. Data and Methodology

2.1 Data Sources

In order to assemble a suitable collection of mesoscale snowband events for further study, the daily climatological records of 39 National Weather Service (NWS) first-order stations throughout the northeast U.S. were queried for occurrences of heavy snow accumulation during the 6-yr period spanning 2005–2010. For purposes of this search (aided by the Northeast Regional Climate Center, http://www.nrcc.cornell.edu/), heavy snow accumulation was defined as accumulation ≥ 6 in. (15.2 cm) during a calendar day. Locations of the stations included in this search are shown in Fig. 2.1. Using this criterion, 136 dates were identified on which heavy snow accumulation occurred at one or more stations, and these dates were deemed *heavy snow dates*.

For each heavy snow date, archived radar data from 20 WSR-88D sites were obtained from the National Climatic Data Center. Utilizing the base reflectivity product from 0.5° elevation scans, radar reflectivity mosaics were constructed using the GDRADR program of the General Meteorological Package (GEMPAK; desJardins et al. 1991). Reflectivity mosaics were mapped at 15-min time intervals using a 5-dB*Z* contouring interval with ~1-km horizontal resolution, then animated in sequence to facilitate the identification and tracking of mesoscale precipitation features. As a quality control measure, single-site reflectivity scans were included in the mosaic only if they were completed within the 15-min period ending at the mosaic time. If multiple scans were completed at a single site within this 15-min period, the most recent (latest) scan was utilized in the mosaic. Additionally, reflectivity mosaics were overlaid with standard

present weather symbols representing hourly METAR reports of surface observations taken in the U.S. and Canada (courtesy of Iowa State University, http://mesonet.agron.iastate.edu/archive/).

Animated reflectivity mosaics and first-order station records for all 136 heavy snow dates were then subjectively examined for evidence of lake effect snow activity. Based on this inspection, 40 heavy snow dates were deemed to be solely attributable to lake effect snow and were removed from further study, leaving 96 heavy snow dates. Numerous groups of consecutive heavy snow dates were ascribed to single precipitation systems based on subjective assessment, such that the 96 heavy snow dates could be organized into 70 *study cases* as shown in Table 1. Thus, each study case may be regarded as corresponding to a weather system that produced heavy snow accumulation (excluding lake effect snow) in the northeast U.S. during the 2005–2010 study period.

For each study case, gridded Climate Forecast System Reanalysis (CFSR; Saha and Coauthors 2010) data were obtained from the National Operational Model Archive and Distribution System (NOMADS; http://nomads.ncdc.noaa.gov/). The CFSR is a global dataset with 0.5° latitude–longitude spatial resolution and 6-h temporal resolution. Using the CFSR dataset, all diagnostic fields in this study have been calculated and plotted by means of GEMPAK applications.

2.2 Methodology

2.2.1 Snowband Identification and Categorization

For each of the 70 study cases, animated reflectivity mosaics and hourly surface observations were used to identify mesoscale snowbands within the reflectivity mosaic domain. Only precipitation structures that were present within the mosaic domain at a 6-h *evaluation time* (i.e., 0600, 1200, 1800, or 0000 UTC, in that sequence) were considered. Snowbands were identified when the following criteria were satisfied:

1) Aspect ratio (length-to-width) of 4:1 or greater in reflectivity mosaics.
2) Reflectivity ≥ 25 dB*Z* along ≥ 50% of the band axis and ≥ 10 dB*Z* over the background reflectivity.
3) Persistence of criteria (1) and (2) for ≥ 3 h. This persistence period may begin at, be inclusive of, or end at the evaluation time.
4) Observed snow at the surface (per hourly surface observations) at any time within the period satisfying criterion (3) and along any segment of the band[1].

Criteria (2) and (3), requiring minimum band intensity and longevity, are similar to the criteria employed by Novak et al. (2004) in their descriptions of "single" and "multi" bands. The presence of a snowband within the reflectivity mosaic domain at a 6-h evaluation time constituted a *banded event*, uniquely identified by a specific time and location. Note that simultaneous banded events were observed (i.e., multiple snowbands present in the mosaic domain at a given evaluation time). Likewise, sequential banded events attributable to a single snowband were observed (i.e., a snowband persisting

[1] By this criterion, all identified snowbands produced surface reports of snow, but precipitation type associated with "snowbands" was not restricted to snow alone. Note that snowbands were not required to traverse first-order stations that reported heavy snow accumulation.

across more than one evaluation time). If no snowband was present within the mosaic domain at an evaluation time, that time was deemed *nonbanded or weakly banded*.

In order to proceed with a systematic investigation of snowband motion, a subjective band motion classification scheme was developed. The intent of this scheme was to classify a large population of banded events within relatively few categories while making operationally meaningful distinctions concerning snowband motion. The resulting classification scheme includes four categories of snowband motion: *laterally translating*, *laterally quasi-stationary*, *hybrid*, and *pivoting*. These snowband motion categories within the hierarchy of study cases and banded events are shown in Fig. 2.2. Before discussing the details of the classification procedure, the following descriptions of each motion category are given:

- *Laterally translating* snowbands exhibit predominantly cross-axis motion, thereby favoring uniform snowfall accumulation within the regions they traverse.
- *Laterally quasi-stationary* snowbands exhibit near-zero cross-axis motion, favoring heavy snowfall accumulation along a narrow, along-axis corridor.
- *Hybrid* snowbands are dominated by along-axis motion, but with a concurrent cross-axis component of motion, favoring snowfall accumulation on an intermediate spatial scale.
- *Pivoting* snowbands exhibit pronounced rotation such that a segment of the band near the center of rotation exhibits near-zero cross-axis motion. This segment of the band is termed the *pivot zone*, where heavy snowfall accumulation is particularly favored.

The following procedure was utilized to categorize snowband motion for each banded event:

1) A suitable 1-h period was subjectively chosen during which band motion could be observed using an animated reflectivity mosaic. Preferentially, this period was chosen so that it was temporally centered on the aforementioned 6-h evaluation time (i.e., spanning 30 min before to 30 min after the evaluation time). However, if during this period snowband criteria were not satisfied, band intensity changes were rapid, or the band was near the edge of the mosaic domain, the 1-h period was adjusted either forward or backward. At most, the 1-h period could begin 1 h before the evaluation time or end 1 h after the evaluation time. If significant radar coverage gaps (spatial or temporal) precluded satisfactory tracking of the candidate snowband, the banded event was deemed *unclassifiable*.
2) A radar reflectivity value most representative of the band outline during this 1-h period was chosen (to the nearest 5 dB*Z*). This value was chosen so as to be high enough to clearly distinguish the band from its background, but low enough to be relatively insensitive to transient band intensity changes. Typically, the 20-dB*Z* value provided a satisfactory band outline.
3) If pivoting motion was observed during this 1-h period (Fig. 2.3, lower right panel), the band was assigned to the pivoting category. The location of the pivot zone at the evaluation time was recorded (to the nearest 0.2° of latitude–longitude) along with the azimuthal orientation of the band (to the nearest 5°) at the pivot zone.

4) If nonpivoting motion was observed during the 1-h period, band centroid positions were fixed at the starting and ending times by locating the approximate midpoint of the band axis as given by the band outline. From these position fixes, a 1-h centroid displacement vector was constructed. Next, the angle between this vector and the line tangent to the band axis at the initial position of the centroid was measured to the nearest 10° (denoted as angle δ), such that δ provided a metric of relative cross-axis motion. The band was then categorized as laterally translating if $45° < \delta \leq 90°$ (Fig. 2.3, top left panel), hybrid if $10° \leq \delta \leq 45°$ (Fig. 2.3, top right panel), or laterally quasi-stationary if $0° \leq \delta < 10°$ (Fig. 2.3, bottom left panel). The location of the centroid at the evaluation time and the azimuthal orientation of the band at the centroid were also recorded.

2.2.2 Vector Frontogenesis and Q-vector Partitioning

As noted in section 1.2.1, mesoscale precipitation bands that are forced by frontogenesis tend to be oriented approximately parallel to midlevel isentropes. Given this relationship, diagnostics that relate to temporal changes in the horizontal potential temperature field are of particular interest for the problem of band motion. One such diagnostic is the so-called Q vector. In the nondivergent flow framework, the Q vector is defined as the temporal rate of change of the *vector* horizontal potential temperature gradient following a trajectory defined by the nondivergent flow [cf. Keyser et al. (1988, p. 763)], i.e.,

$$\mathbf{Q} = \frac{D}{Dt_\psi}\boldsymbol{\nabla}_p\theta, \qquad (1)$$

where θ is the potential temperature, the subscript ψ denotes evaluation in the nondivergent flow framework, and the subscript p denotes differentiation on an isobaric surface. The use of the nondivergent wind in place of the geostrophic wind for QG diagnostics was advocated by Galarneau and Keyser (2008), who suggested that the nondivergent wind provides a better representation of the balanced wind in curved flow than either the geostrophic wind or total wind. According to (1), the Q vector may be regarded as a vector generalization of the Petterssen frontogenesis function (Keyser et al. 1988) applied to the nondivergent flow. The QG omega equation for isentropic, frictionless flow may be written in terms of the Q vector [following Keyser et al. (1988)] as

$$\left(\sigma\boldsymbol{\nabla}_p^2 + f_0^2\frac{\partial^2}{\partial p^2}\right)\omega = -2h\boldsymbol{\nabla}_p \cdot \mathbf{Q}, \qquad (2)$$

where $\sigma = -h[d\Theta(p)/dp]$ is a pressure-dependent reference static stability, $h = (R/p_0)(p_0/p)^{c_v/c_p}$, p_0 is a reference pressure (1000 hPa), and f_0 is a reference Coriolis parameter. According to (1) and (2), Q-vector convergence (divergence) indicates forcing for ascent (descent) by the nondivergent flow.

In order to separately evaluate the temporal rates of change of the *magnitude* and *direction* of the horizontal potential temperature gradient that are encapsulated in (1), a natural-coordinate partitioning of the Q vector is employed following Keyser et al. (1988). First, the local orientation of the horizontal potential temperature gradient is used to define a unit vector **n**:

$$\mathbf{n} = -\left|\boldsymbol{\nabla}_p\theta\right|^{-1}\boldsymbol{\nabla}_p\theta, \qquad (3)$$

which is directed normal to the local isentrope toward colder air. A second unit vector **s**, which is orthogonal to **n**, is defined as

$$\mathbf{s} = \mathbf{n} \times \mathbf{k}, \qquad (4)$$

such that **s** is directed tangent to the local isentrope with cold air on the left. Unit vectors **s** and **n** are then used to define a natural coordinate system (s, n) in which the Q vector is partitioned into along- and across-isentrope contributions:

$$\mathbf{Q} = Q_n\mathbf{n} + Q_s\mathbf{s}, \qquad (5)$$

or

$$\mathbf{Q} = \mathbf{Q}_{\boldsymbol{n}} + \mathbf{Q}_{\boldsymbol{s}}, \qquad (6)$$

where $\mathbf{Q}_{\boldsymbol{n}} = Q_n\mathbf{n}$ and $\mathbf{Q}_{\boldsymbol{s}} = Q_s\mathbf{s}$. This natural-coordinate partitioning is illustrated schematically in Fig. 2.4. The scalar quantity Q_n is the *frontogenetical* component of $\mathbf{Q}$ and quantifies the temporal rate of change of the *magnitude* of the horizontal potential temperature gradient as effected by the nondivergent flow. Frontogenesis (frontolysis) by the nondivergent flow is indicated by $Q_n < 0$ ($Q_n > 0$), such that $\mathbf{Q}_{\boldsymbol{n}}$ is directed towards warmer (colder) air. The scalar quantity Q_s is the *rotational* component of $\mathbf{Q}$ and quantifies the temporal rate of change of the *direction* of the horizontal potential temperature gradient as effected by the nondivergent flow. Rotation of the potential temperature gradient is sometimes referred to as *rotational frontogenesis*. Counterclockwise (clockwise) rotation of the horizontal potential temperature gradient by the nondivergent flow is indicated by $Q_s > 0$ ($Q_s < 0$), such that $\mathbf{Q}_{\boldsymbol{s}}$ is directed downshear (upshear). Adapting Eqs. (2.10a) and (2.10b) in Keyser et al. (1988) for the nondivergent framework, diagnostic equations for the scalars Q_n and Q_s may be written respectively as

$$Q_n = -\frac{1}{2}\left|\nabla_p\theta\right|E_\psi \cos 2\beta, \qquad (7)$$

and

$$Q_s = \frac{1}{2}\left|\nabla_p\theta\right|\left(\zeta_\psi + E_\psi \sin 2\beta\right), \qquad (8)$$

where ζ_ψ and E_ψ are the relative vorticity and resultant deformation, respectively, of the nondivergent flow and β is angle between the axis of dilatation defined by the nondivergent flow and the orientation of the local isentrope. According to (7), intensification or weakening of the horizontal potential temperature gradient by the nondivergent flow is accomplished only by horizontal deformation. However, (8) indicates that relative vorticity and/or horizontal deformation may effect a rotation of the horizontal potential temperature gradient by the nondivergent flow.

According to (7) and (8), the magnitudes of Q_n and Q_s are strongly dependent on the magnitude of the horizontal potential temperature gradient. In order to isolate the *kinematic* contributions to both frontogenesis and rotational frontogenesis by the nondivergent wind, equations for *normalized* Q_n $\left(\tilde{Q}_n\right)$ and *normalized* Q_s $\left(\tilde{Q}_s\right)$ may be written respectively [cf. Schultz (2004)] as:

$$\tilde{Q}_n = \left|\nabla_p\theta\right|^{-1} Q_n, \qquad (9)$$

and

$$\tilde{Q}_s = \left|\nabla_p\theta\right|^{-1} Q_s. \qquad (10)$$

$-\tilde{Q}_n$ is the fractional Lagrangian rate of change of the magnitude of the horizontal potential temperature gradient by the nondivergent flow, whereas $\tilde{Q}_s$ is the Lagrangian rate of change of the direction of the horizontal potential temperature gradient by the

nondivergent flow [see Keyser et al. (1988, p. 764)]. Note that these normalized quantities have the same dimensions as both horizontal deformation and relative vorticity.

In this study, Q vectors were calculated from Gaussian-smoothed nondivergent wind and potential temperature fields using the "GWFS" filtering function included in the GEMPAK diagnostic suite. GWFS filter weights for nondivergent wind components and potential temperature were set at 15 and 25, respectively. The effect of this smoothing was to suppress short-wavelength signals in the resulting diagnostic fields.

2.2.3 Composite Analysis

Composite averages of diagnostic fields were calculated for the laterally translating, laterally quasi-stationary, and pivoting band motion categories in order to ascertain the common environmental attributes associated with each category. Given that the banded events belonging to a given category were observed in locations throughout the reflectivity mosaic domain, an event-centered compositing approach was utilized. In this scheme, event centers were defined as the *band centroid* for laterally translating and laterally quasi-stationary bands and the *pivot zone* for pivoting bands. For each composite category, only those bands whose azimuthal orientations were within 20° of the category mean were retained for compositing. This restriction ensured that along- and across-band variations in the diagnostic fields would not become overly smoothed in the composite field due to large differences in member band orientations. Composite calculations then proceeded by re-centering events onto Albany, NY (chosen arbitrarily), and then averaging variables across member events. Composites of *derived* variables

(e.g., Petterssen frontogenesis, Q vectors) were obtained by first calculating the variable for each event and then averaging the variable across member events.

2.2.4 Case Studies

Representative banded events that typify each composite category were subjectively chosen as case studies based on the resemblance of their diagnostic fields to the corresponding composites. Although composites of hybrid snowband events were not calculated, a hybrid snowband event was also chosen for a case study. Snowfall accumulation maps for all case studies were obtained from the National Operational Hydrologic Remote Sensing Center (NOHRSC, http://www.nohrsc.noaa.gov/).

2.2.5 Trajectory Calculations

Kinematic backward trajectories were calculated for each case study by linearly interpolating the 6-h CFSR total kinematic fields (i.e., u, v, and ω) in both space and time. Trajectories were initialized from endpoints spaced ~20 km apart along the band axes. Similarly, *composite* kinematic backward trajectories were calculated using a sequence of time-lagged composite kinematic fields at 6-h intervals, and then linearly interpolating the composite fields in both space and time. The endpoints for composite kinematic trajectories were spaced ~20 km apart along the category-mean band axes.

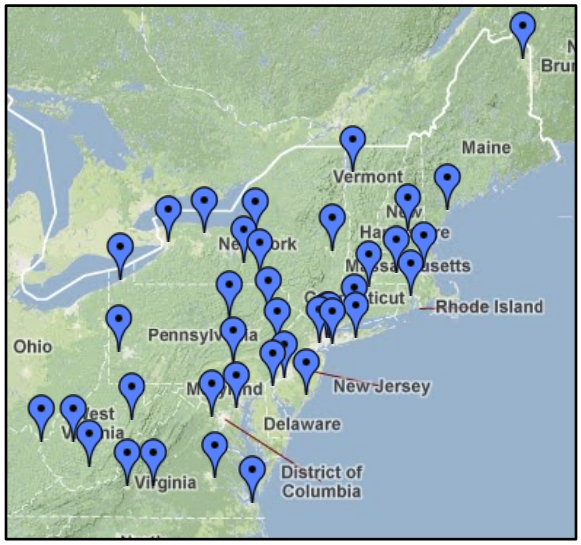

Fig. 2.1. Map showing the locations of 39 NWS first-order stations that were utilized in this study.

Table 1. Listing of study cases and their associated heavy snow dates.

Case No.	Heavy Snow Date(s)	Case No.	Heavy Snow Date(s)
1	5 Jan 2005	41	13 Feb 2008
	6 Jan 2005		
2	19 Jan 2005		
	20 Jan 2005	42	22 Feb 2008
3	22 Jan 2005	43	26 Feb 2008
	23 Jan 2005		27 Feb 2008
4	26 Jan 2005	44	1 Mar 2008
5	10 Feb 2005	45	7 Mar 2008
	11 Feb 2005		8 Mar 2008
6	21 Feb 2005	46	20 Mar 2008
7	24 Feb 2005	47	25 Nov 2008
8	28 Feb 2005	48	12 Dec 2008
	1 Mar 2005	49	19 Dec 2008
9	8 Mar 2005	50	21 Dec 2008
10	11 Mar 2005		22 Dec 2008
	12 Mar 2005	51	10 Jan 2009
11	23 Mar 2005		11 Jan 2009
12	3 Apr 2005	52	18 Jan 2009
13	9 Dec 2005	53	28 Jan 2009
14	16 Dec 2005	54	3 Feb 2009
15	25 Dec 2005	55	22 Feb 2009
	26 Dec 2005		23 Feb 2009
16	3 Jan 2006	56	2 Mar 2009
17	23 Jan 2006	57	22 Oct 2009
18	11 Feb 2006	58	9 Dec 2009
	12 Feb 2006	59	18 Dec 2009
19	25 Feb 2006		19 Dec 2009
20	2 Mar 2006		20 Dec 2009
21	4 Mar 2006	60	23 Dec 2009
22	6 Feb 2007	61	2 Jan 2010
23	14 Feb 2007		3 Jan 2010
24	2 Mar 2007	62	9 Jan 2010
25	16 Mar 2007	63	18 Jan 2010
	17 Mar 2007	63	30 Jan 2010
26	4 Apr 2007	64	5 Feb 2010
	5 Apr 2007		
27	13 Apr 2007		6 Feb 2010
28	16 Apr 2007	65	9 Feb 2010
	17 Apr 2007		10 Feb 2010
29	3 Dec 2007	66	16 Feb 2010
30	5 Dec 2007	67	23 Feb 2010
31	13 Dec 2007		24 Feb 2010
32	16 Dec 2007	68	25 Feb 2010
	17 Dec 2007		26 Feb 2010
33	20 Dec 2007	69	16 Dec 2010
34	31 Dec 2007	70	26 Dec 2010
35	1 Jan 2008		27 Dec 2010
36	14 Jan 2008		
37	18 Jan 2008		
38	2 Feb 2008		
39	5 Feb 2008		
40	6 Feb 2008		

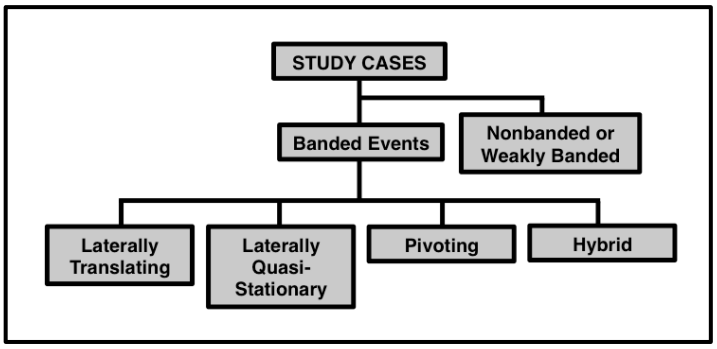

Fig. 2.2. Flowchart of the snowband motion classification scheme used in this study. The defining criteria for each motion category, along with schematic illustrations, are given in Fig. 2.3.

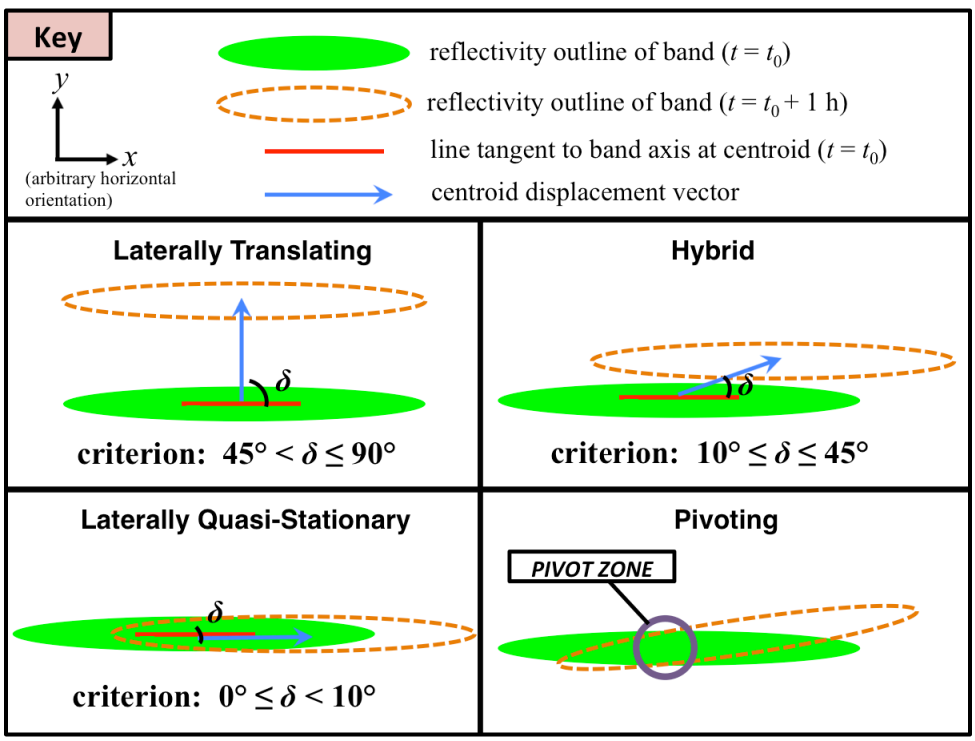

Fig. 2.3. Schematic representations of the four snowband motion categories and their defining criteria. The start of the 1-h period during which band motion is evaluated is denoted by t_0. See text for details.

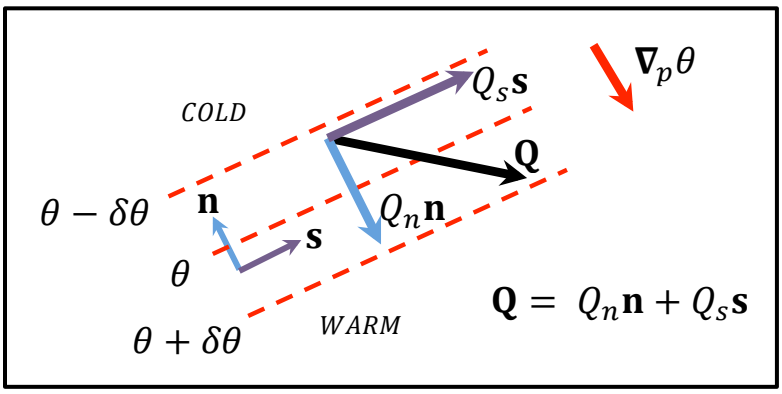

Fig. 2.4. Illustration of a natural-coordinate partitioning of the Q vector into along- and cross-isentrope contributions following Keyser et al. (1988). See text for discussion.

3. Results

3.1 Snowband Identification and Categorization

The snowband identification criteria discussed in section 2.2.1 were applied to the 70 study cases at 6-h evaluation times. Of these cases, 36 cases were deemed *nonbanded or weakly banded* for their entirety, with the remaining 34 cases each containing at least one banded event (Fig. 3.1a). The snowband motion classification scheme was then applied to these 34 study cases, with the results of this categorization summarized in Fig. 3.1b. Because some study cases contained multiple banded events of different categories, the cases in Fig. 3.1b do not sum to 34. The overall distribution of banded events after summing across all study cases is shown in Fig. 3.1c. Pivoting snowband events were the most commonly observed, with 26 pivoting snowband events identified across 16 study cases. Hybrid snowband events were the most rarely observed, with seven hybrid snowband events identified across six study cases. Five snowband events in four study cases were deemed unclassifiable. A detailed catalog of all banded events in the laterally translating, laterally quasi-stationary, hybrid, and pivoting categories is found in the Appendix.

3.2 Composite Analysis

3.2.1 Composite Members

As discussed in section 2.2.3, only banded events in the laterally translating, laterally quasi-stationary, and pivoting categories whose band azimuthal orientations

were within 20° of their respective category mean were included in event-centered composite calculations. After applying this restriction, 17 of the 19 laterally translating banded events (89%), eight of the nine laterally quasi-stationary banded events (89%), and 18 of the 26 pivoting banded events (69%) were retained for compositing. Seven hybrid banded events were observed within relatively dissimilar synoptic-scale settings. For this reason, composite calculations for the hybrid category were not performed.

All member bands in the laterally translating composite were observed to move in a north or northeastward direction towards lower 1000–500-hPa thickness. Member bands in the laterally quasi-stationary composite moved northeastward with lower 1000–500-hPa thickness toward their left. Finally, all member bands in the pivoting composite were observed to rotate counterclockwise with lower 1000–500-hPa thickness on their northwestern side.

3.2.2 Laterally Translating Category Composite

The band centroid of the composite laterally translating snowband is located ~800 km east-northeast of a sub-1004-hPa surface cyclone (Fig. 3.2a). This mean cyclone is favorably positioned for deepening via the implied advection of 1000–500-hPa cyclonic thermal vorticity by the 1000–500-hPa thermal wind atop the surface cyclone center. Isopleths of 1000–500-hPa thickness near the band centroid imply a mean WNW–ESE band orientation, consistent with the mean azimuthal orientation obtained from observational measurements of composite-member bands (see Appendix). The inferred band axis is found beneath the equatorward entrance region of a 70–80 m s^{-1} upper-level jet streak, where deep-layer ascent is favored. In the middle troposphere, a closed 850–

700-hPa cyclonic circulation is located ~1000 km west of the band centroid (Fig. 3.2b). A region of frontogenesis is found near the band axis within both the 850–700-hPa and 700–500-hPa layers (Figs. 3.2b,c) with an implied vertical tilt of the frontogenesis axis towards colder air. This frontogenesis is associated with deformation amid diffluent flow in both the 850–700-hPa and 700–500-hPa layers, along with pronounced across-band low-to-midlevel flow. Given the thickness isopleth orientation noted above, the presence of composite low-to-midlevel frontogenesis along the inferred band axis provides evidence that composite-member snowbands were forced (at least in part) by frontogenesis. Composite plots of relative humidity indicate that the inferred band is positioned near the northeastern edge of near-saturation at 850 hPa (Fig. 3.3a) but well within a region of near-saturation through the 700–400-hPa layer (Figs. 3.3b–f), far removed from the composite dry slot to its southwest. Consistent with this horizontal relative humidity distribution, reflectivity mosaics indicated that laterally translating snowbands were often embedded in nonbanded precipitation.

Composite plots of temperature advection indicate that the laterally translating band centroid is located ~250 km to the cold side of a pronounced 850–700-hPa warm advection maximum (Fig. 3.4a). Somewhat weaker warm advection is found along the inferred band axis within both the 850–700-hPa and 700–500-hPa layers (Figs. 3.4a,b). Consistent with thermal wind considerations, the composite vertical wind profile at the laterally translating band centroid is characterized by deep-layer veering with height (Fig. 3.5). Additionally, the composite hodograph exhibits pronounced clockwise curvature below 2 km MSL, but is approximately straight above this level (Fig. 3.5, inset).

The composite thermodynamic profile at the laterally translating snowband centroid (Fig. 3.5) contains a dendritic growth zone (DGZ, defined as the layer of near-saturation between the −12 and −18°C isotherms) through a ~100-hPa depth. Dendritic crystals descending through this layer are therefore subjected to a prolonged period of efficient growth via deposition, thereby contributing to high snowfall accumulation rates near the composite band centroid.

Q vector calculations indicate that the composite laterally translating snowband is located within a region of strong QG forcing for ascent (i.e., *Q*-vector convergence) in both the 700–500-hPa and 850–700-hPa layers (Figs. 3.6a,d). This forcing for ascent likely contributes to widespread cloud and precipitation production in the presence of deep-layer moisture. Partitioning of the *Q* vector into along- and across-isentrope contributions indicates that both Q_s- and Q_n-vector convergence contribute to forcing for ascent near the inferred snowband in both the 700–500-hPa layer (Figs. 3.6b,c) and 850–700-hPa layer (Figs. 3.6e,f). The largest Q_s vectors along inferred band axis are found near its upshear and downshear flanks where they are oppositely directed and convergent (Figs. 3.6b,e). Q_n vectors along the band axis are directed towards warmer air (indicating frontogenesis by the nondivergent wind) and convergent (Figs. 3.6c,f).

The composite fields of normalized Q_s and normalized Q_n are shown in Fig. 3.7. Positive (negative) normalized Q_s is found in the region generally upshear (downshear) of the composite band centroid (Figs. 3.7a,c), indicating that normalized Q_s contributes to counterclockwise (clockwise) rotation of isentropes in these respective regions. Normalized Q_n is most negative on the cold side of the band axis, where it contributes

most strongly to frontogenesis in the 700–500-hPa and 850–700-hPa layers (Figs. 3.7b,d).

Composite 24-h backward kinematic trajectories ending at 11 locations along the mean band axis at 700 hPa and 500 hPa are shown in Figs. 3.8a and 3.8b, respectively. Both panels depict a group of parcels (a "parcel cluster") emanating from the lower troposphere near water vapor source regions (i.e., the southeast U.S. and Gulf of Mexico coast) and ascending as they approach the axis of the mean laterally translating snowband. As they ascend, the parcel clusters generally undergo elongation in the across-trajectory direction, more notably the parcel cluster arriving at 700 hPa (Fig. 3.8a). This across-trajectory elongation is consistent with the effect of time-integrated deformation within a diffluent airstream. Veering of trajectory orientation with height near their termini is consistent with the 700–500-hPa warm advection depicted in Fig. 3.4b.

3.2.3 Laterally Quasi-Stationary Category Composite

The centroid of the composite laterally quasi-stationary snowband is located ~700 km north of a sub-1004-hPa surface cyclone (Fig. 3.9a). As with the mean cyclone in the laterally translating category composite, this cyclone is favorably positioned for deepening, given the implied advection of 1000–500-hPa cyclonic thermal vorticity by the 1000–500-hPa thermal wind over the cyclone center. 1000–500-hPa thickness isopleths imply a mean southwest–northeast band orientation, consistent with observations of composite-member bands (see Appendix). Similar to the composite

laterally translating snowband, the composite laterally quasi-stationary snowband is situated beneath the equatorward entrance region of an upper-level jet streak. However, the jet maximum is ~10 m s^{-1} weaker (60–70 m s^{-1}) in the laterally quasi-stationary category composite and is oriented southwest–northeast (Figs. 3.2a, 3.9a). The closed surface cyclone "opens up" to a mean short-wave trough in the 850–700-hPa and 700–500-hPa layers (Figs. 3.9b,c). These layers both exhibit regions of frontogenesis along the inferred band axis, with a vertical tilt of the frontogenesis axis towards colder air also apparent. In contrast to the laterally translating category composite, where frontogenesis is associated with *diffluent* flow, frontogenesis in the laterally quasi-stationary category composite is associated with deformation amid *confluent* southwesterly low-to-midlevel flow (Figs. 3.2b,c, 3.9b,c). Composite plots of relative humidity (Fig. 3.10) reveal the presence of near-saturation in the 850–300-hPa layer along the inferred band axis and on its warm side. However, a pronounced horizontal gradient of relative humidity at 700 hPa and 600 hPa is found immediately to the cold side of the band axis (Figs. 3.10b,c). Consistent with this horizontal relative humidity distribution, reflectivity mosaics indicated that precipitation coverage was often quite limited on the cold sides of laterally quasi-stationary snowbands.

Weak/neutral composite temperature advection is found along the laterally quasi-stationary band axis in the 850–700-hPa layer (Fig. 3.11a). Within this layer, the band axis approximately delineates regions of temperature advection of opposite sign, with warm (cold) advection generally on the warm (cold) side of the inferred snowband. Farther aloft, in the 700–500-hPa layer, weak warm advection is found along the inferred band axis (Fig 3.11b). Still, the temperature advection distribution in this layer resembles

that of the 850–700-hPa layer, with a broad warm–cold advection dipole approximately oriented in the across-isotherm (and across-band) direction. Consistent with weak/neutral low-to-midlevel temperature advection and thermal wind considerations, the composite hodograph at the band centroid is approximately straight and radially oriented (Fig. 3.12, inset). The composite thermodynamic profile at the laterally quasi-stationary snowband centroid contains a DGZ through a ~90-hPa layer (Fig. 3.12), slightly shallower than the ~100-hPa DGZ at the composite laterally translating snowband centroid (Figs. 3.5, 3.12).

Q vector calculations indicate that the composite laterally quasi-stationary snowband is situated within a region of QG forcing for ascent in both the 700–500-hPa and 850–700-hPa layers (Figs. 3.13a,d). However, QG forcing for ascent at the band centroid is weaker than at the composite laterally translating band centroid (Figs. 3.6a,d, 3.13a,d). Q_s vectors in the 700–500-hPa and 850–700-hPa layers are small in magnitude along and near the inferred band axis, indicating weak rotational frontogenesis by the nondivergent wind (Figs. 3.13b,e). Q_n vectors in these layers are frontogenetical along the band axis and contribute to a band-parallel region of Q_n-vector convergence in both layers (Figs. 3.13c,f).

Composite fields of normalized Q_s and normalized Q_n are shown in Fig. 3.14. Within the 700–500-hPa and 850–700-hPa layers, normalized Q_s contributes to weak rotation of the horizontal potential temperature gradient along and near the inferred laterally quasi-stationary snowband (Figs. 3.14a,c). The contribution of normalized Q_n towards frontogenesis is largest on the cold side of the band axis in the 700–500-hPa layer (Fig. 3.14b) and on the warm side of the band axis in the 850–700-hPa layer (Fig. 3.14d).

Composite 24-h backward kinematic trajectories ending at 11 locations along the mean laterally quasi-stationary snowband axis are shown in Fig. 3.15. Similar to the laterally translating category composite, parcel clusters arrive at the snowband after undergoing ascent in southwesterly flow (Figs. 3.8, 3.15). However, whereas parcel clusters in the laterally translating category composite undergo elongation in the *across-trajectory* direction (Fig. 3.8), parcel clusters in the laterally quasi-stationary category composite undergo elongation mainly in the *along-trajectory* direction, consistent with the effect of time-integrated deformation within a confluent airstream.

3.2.4 Pivoting Category Composite

The *pivot zone* of the composite pivoting snowband is located ~350 km northwest of a relatively strong (sub-994-hPa) surface cyclone (Fig. 3.16a). As with the mean cyclones in the laterally translating and laterally quasi-stationary category composites, this cyclone is favorably situated for deepening via the implied advection of 1000–500-hPa cyclonic thermal vorticity by the 1000–500-hPa thermal wind. The isopleths of 1000–500-hPa thickness indicate that the composite pivot zone is found near the inflection point of a well-developed "S"-shaped thickness field. A mean southwest–northeast band orientation is also implied, in agreement with observations of composite-member pivoting snowbands (see Appendix). The inferred axis of the composite pivoting snowband is somewhat farther removed from the upper-level jet axis than the laterally translating and laterally quasi-stationary band axes (Figs. 3.2a, 3.9a, 3.16a). However, the composite surface cyclone is situated beneath the poleward exit region of a

mean upper-level jet streak (Fig. 3.16a). A mean closed circulation extends upward to the 850–700-hPa layer, where it is positioned ~200 km to the south of the composite pivot zone (Fig. 3.16b). Farther aloft, this circulation "opens up" to a composite negatively tilted short-wave trough in the 700–500-hPa layer (Fig. 3.16c). Both the 850–700-hPa and 700–500-hPa layers exhibit regions of pronounced frontogenesis, with a steeply sloped (i.e., approximately upright) axis of maximum frontogenesis between these layers (Figs. 3.16b,c). This frontogenesis is found within a region of strong deformation amid flow that is generally diffluent in both layers and strongly curved in the 850–700-hPa layer. Note that the composite pivot zone is located within the upshear portion of the frontogenesis region in both the 850–700-hPa and 700–500-hPa layers.

Composite relative humidity plots reveal the presence of near-saturation through the 850–400-hPa layer along the inferred band axis and on its *cold* side (Figs. 3.17a–e). A well-developed composite dry slot, characteristic of developing extratropical cyclones, is clearly evident through the 700–400-hPa layer (Figs. 3.17b–e). The composite pivot zone is located near the dry slot–comma head interface and adjacent to a strong horizontal gradient of relative humidity through the 600–400-hPa layer (Figs. 3.17c–e). A strong upward decrease of relative humidity within the dry slot region implies reduced potential stability in this region. Cellular precipitation structures, suggestive of potential instability, were often observed in reflectivity mosaics on the warm sides of pivoting snowbands.

A mean warm–cold advection dipole is evident in the 850–700-hPa and 700–500-hPa layers (Figs. 3.18a,b). In contrast to the laterally quasi-stationary category composite, where a low-to-midlevel warm–cold advection dipole is oriented in the

across-isotherm (and across-band) direction (Figs. 3.11a,b), the warm–cold advection dipole in the pivoting category composite is largely oriented in the along-isotherm (and along-band) direction. The composite pivot zone is situated ~250 km west of warm advection maxima in both the 850–700-hPa and 700–500-hPa layers, with mean low-to-midlevel warm advection at the pivot zone itself and along much of the inferred band axis. Consistent with thermal wind considerations, the composite vertical wind profile at this location is characterized by pronounced deep-layer veering through >180° of azimuth (Fig. 3.19). As with the laterally translating category composite hodograph (Fig. 3.5, inset), the pivoting category composite hodograph exhibits sharp clockwise curvature below 2 km AGL, with an approximately straight mean hodograph through the 2–10-km layer (Fig. 3.19, inset). The composite thermodynamic profile at the pivot zone (Fig. 3.19) contains a DGZ whose depth (~140 hPa) exceeds that of the DGZs in both the laterally translating and laterally quasi-stationary category composites (Figs. 3.5, 3.12).

Q vector calculations reveal that the composite pivoting snowband is situated within a region of QG forcing for ascent in both the 700–500-hPa and 850–700-hPa layers (Figs. 3.20a,d). In both layers, Q_s-vector convergence is found at the composite pivot zone and along much of the inferred band axis (Figs. 3.20b,e). Composite Q_s vectors are downshear-directed (indicating positive rotational frontogenesis) along most of the band axis, with the largest Q_s vectors situated *upshear* of the pivot zone. Q_n vectors are also convergent along the inferred pivoting snowband axis in both the 700–500-hPa and 850–700-hPa layers (Figs. 3.20c,f). However, in contrast to the convergence of *frontogenetical* Q_n vectors that was previously noted along and near the composite band axes of laterally translating and laterally quasi-stationary snowbands

(Figs. 3.6c,f, 3.13c,f), Q_n-vector convergence along the composite pivoting snowband has contributions from both frontogenetical *and* frontolytical Q_n vectors. Specifically, Q_n vectors are generally frontolytical (frontogenetical) in the region upshear (downshear) of the pivot zone, resulting in coherent, band-parallel stripe of Q_n-vector convergence (Figs. 3.20c,f).

The composite fields of normalized Q_s and normalized Q_n are shown in Fig. 3.21. Normalized Q_s contributes to counterclockwise rotation of isentropes at the pivot zone within both the 700–500-hPa and 850–700-hPa layers (Figs. 3.21a,c). Further, the approximate overlap of the normalized-Q_s maximum with the largest downshear-directed Q_s vectors (Figs. 3.20b,e) indicates that these Q_s vectors also happen to receive the greatest *kinematic* contribution towards their overall magnitudes. This overlap is found upshear of the pivot zone, so that the pivot zone coincides with neither the largest downshear-directed Q_s vectors nor the greatest normalized Q_s. A dipole of positive–negative normalized Q_n, approximately oriented across the composite pivot zone, is apparent in the 700–500-hPa and 850–700-hPa layers (Figs. 3.21b,d). This configuration indicates that normalized Q_n makes the largest contribution towards frontogenesis (frontolysis) in the region generally downshear (upshear) of the pivot zone.

Composite 24-h backward kinematic trajectories ending at 11 locations along the mean pivoting snowband axis are shown in Fig. 3.22. The parcel cluster arriving at 700 hPa (Fig. 3.22a) exhibits stretching in the across-trajectory direction, consistent with the effect of time-integrated deformation within a diffluent airstream, similar to the parcel cluster arriving at 700 hPa in the laterally translating category composite (Fig. 3.8a).

Pronounced veering of trajectory orientation with height near their termini is consistent with mean 700–500-hPa warm advection depicted in Fig. 3.18b.

3.3 Case Studies

3.3.1 Laterally Translating Snowband

A laterally translating snowband extended from north-central Pennsylvania to western Long Island and adjacent coastal waters at 0600 UTC 9 December 2009 (Fig. 3.23). This band progressed northeastward at ~15 m s^{-1} and affected a broad geographic region from central Pennsylvania to east-central New York. At 0600 UTC, 0.5° reflectivity exceeded 35 dB*Z* along a significant length of the band axis, and numerous stations reported moderate snow as the band passed overhead (not shown). Consistent with the progressive cross-axis motion of the band, 24-h snowfall accumulations ending at 1200 UTC 9 December were fairly uniform (~10–15 cm) across the region swept by the band (Fig. 3.24). Per surface observations, the southeastern cutoff in snowfall accumulation was attributable to a rain–snow line.

The snowband was situated well east of a sub-988-hPa surface located over northern Illinois and near the equatorward entrance region of a 250-hPa jet streak at 0600 UTC 9 December (Fig. 3.25a). During the subsequent 12 h, the surface cyclone deepened by ~12 hPa as it moved northeastward into central Michigan (not shown). Diffluent flow was present in the middle troposphere at 0600 UTC along and near the snowband within the 850–700-hPa and 700–500-hPa layers (Figs. 3.25b,c). However, resultant deformation and frontogenesis along and near the band were stronger in the

700–500-hPa layer than in the 850–700-hPa layer. Although this band was situated near the eastern extent of near-saturation at 850 hPa (Fig. 3.26a), the band was well embedded within a region of near-saturation through the 700–300-hPa layer (Figs. 3.26b–f), far removed from a developing dry slot.

Consistent with the location of the band *east* of a surface cyclone, warm advection was present along the band axis within the 850–700-hPa and 700–500-hPa layers (Figs. 3.27a,b). In both layers, warm advection maxima were situated on the warm side of the band axis. The vertical wind profile at the band centroid veered with height (Fig. 3.28) and the corresponding hodograph exhibited clockwise curvature mainly below 3 km AGL (Fig. 3.28, inset). The band centroid also exhibited a DGZ spanning a ~95-hPa layer (Fig. 3.28).

QG forcing for ascent was present along and near the band axis within both the 700–500-hPa and 850–700-hPa layers (Figs. 3.29a,d). Within these layers, both Q_s- and Q_n-vector convergence contributed to forcing for ascent near the band axis (Figs. 3.29b,c,e,f). Q_s vectors near opposite flanks of the band were oppositely directed (Figs. 3.29b,e), while Q_n vectors along the band axis were frontogenetical (Figs. 3.29c,f) and collocated with Q_s-vector convergence.

24-h backward kinematic trajectories indicate that the parcel clusters arriving along the band at both 700 hPa and 500 hPa generally originated across the southeast U.S. (Figs. 3.30a,b). Both parcel clusters ascended from the lower troposphere, although parcels arriving at 500 hPa (Fig. 3.30b) generally originated from lower levels than those arriving at 700 hPa (Fig. 3.30a). As they ascended, both parcel clusters underwent

elongation primarily in the across-trajectory direction, consistent with time-integrated diffluence.

3.3.2 Laterally Quasi-Stationary Snowband

A laterally quasi-stationary snowband was observed at 0600 UTC 2 March 2009 extending from northern New Jersey to extreme southern Maine (Fig. 3.31). This band progressed northeastward along its axis, impacting a narrow corridor that stretched from southeastern Pennsylvania to southern Maine. 0.5° reflectivity along much of the band exceeded 30 dB*Z* at 0600 UTC, and numerous stations reported a prolonged (> 2 h) period of moderate snow as the band remained overhead. Northwest of this band, a pronounced cutoff in 0.5° reflectivity was present (Fig. 3.31). The along-axis motion of this snowband produced a distinct southwest–northeast axis of heavy snow accumulation (> 20 cm) that aligned with the corridor impacted by this snowband (Fig. 3.32). Southeast of this axis, snowfall accumulation was somewhat lighter (generally 15–20 cm) across a broad area where nonbanded precipitation was observed. However, snowfall accumulation tapered markedly on the northwest side of this axis, where many locations within ~50 km of this axis received < 4 cm of accumulation, resulting in a pronounced northwest–southeast snowfall accumulation gradient (Fig. 3.32).

At 0600 UTC 2 March, the laterally quasi-stationary snowband was located north of a sub-1004-hPa surface cyclone near the Virginia/North Carolina coast and beneath the equatorward entrance region of a 250-hPa jet streak (Fig. 3.33a). Modest deepening (< 4 hPa) of this cyclone was observed during the subsequent 12-h period as it moved

northeastward (not shown). At 0600 UTC 2 March, frontogenesis was found near the band axis within the 850–700-hPa layer, and a layer-mean col was present near the band axis (Fig. 3.33b). Farther aloft, in the 700–500-hPa layer, the band was situated in confluent southwesterly flow ahead of a short-wave trough axis (Fig. 3.33c), with weaker frontogenesis along the band axis in this layer than in the underlying 850–700-hPa layer (Figs. 3.33b,c). The band was also situated northeast of a 700–400-hPa dry slot (Figs. 3.34b–e) and adjacent to a distinct horizontal gradient of relative humidity at 850 and 700 hPa (Figs. 3.34a,b). This horizontal relative humidity gradient was consistent with the observed cutoff in radar reflectivity along the cold (northwestern) side of the snowband at 0600 UTC (Fig. 3.31).

Weak/neutral temperature advection was present along the band axis in the 850–700-hPa layer (Fig. 3.35a). Within this layer, the band axis broadly delineated regions of opposite-sign temperature advection, with warm (cold) advection generally on the warm (cold) sides of the snowband. Farther aloft, weak warm advection was present along the band axis in the 700–500-hPa layer (Fig. 3.35b), but the temperature advection pattern nonetheless broadly resembled that of the 850–700-hPa layer (Fig. 3.35a). The hodograph at the band centroid was approximately straight and radially oriented through the ~0–5-km AGL layer (Fig. 3.36, inset), and accordingly, winds in this layer exhibited no pronounced backing or veering with height (Fig. 3.36). This hodograph shape is consistent with thermal wind considerations, given that the band centroid was collocated with weak/neutral low-to-midlevel temperature advection in a baroclinic environment (Fig. 3.35a,b). A DGZ spanning ~100 hPa was also present at the band axis (Fig. 3.36).

QG forcing for ascent was present along most of the band within the 700–500-hPa and 850–700-hPa layers (Figs. 3.37a,d), although QG forcing for descent was present near the band centroid. Q_s vectors were generally small along the band axis in the 700–500-hPa and 850–700-hPa layers (Figs. 3.37b,e), indicating weak rotational frontogenesis by the nondivergent wind. Q_n vectors along the band axis in these layers were frontogenetical and contributed to band-parallel regions of Q_n-vector convergence (Figs. 3.37c,f).

24-h backward kinematic trajectories for parcels arriving along the band at both 700 and 500 hPa (Figs. 3.38a,b) depict parcel clusters that elongated mainly in the along-trajectory direction (more noticeably in Fig. 3.38b), consistent with the effect of time-integrated confluence. Similar to the parcels associated with the 9 December 2009 laterally translating snowband case, the parcels arriving at 500 hPa generally originated from lower levels than those arriving at 700 hPa (Figs. 3.30a,b and 3.38a,b).

3.3.3 Pivoting Snowband

At 1200 UTC 12 February 2006, a pivoting snowband extended from Chesapeake Bay to far southeastern New Hampshire (Fig. 3.39). Animated 0.5° reflectivity mosaics indicated that this band rotated counterclockwise while translating northeastward, and at 1200 UTC, the pivot zone of this snowband was located over northern Connecticut (Fig. 3.39). 0.5° reflectivity exceeded 35 dB*Z* along some segments of this band, and several stations traversed by the band reported heavy snow for > 5 h. The plot of 24-h snowfall accumulation ending at 1800 UTC 12 February 2006 (Fig. 3.40) indicates that some of

the heaviest accumulation (locally exceeding 50 cm) was observed near the 1200 UTC pivot zone location, where snowband residence time had been prolonged. A southwest–northeast axis of heavy accumulation is also apparent, with accumulation tapering sharply on its northwest side, where many locations within ~40 km of this axis received < 10 cm of snowfall. This snowfall distribution yielded a pronounced northwest–southeast gradient of snowfall accumulation (Fig. 3.40).

The pivot zone of the snowband at 1200 UTC 6 February was situated north-northwest of a sub-992-hPa surface cyclone off the mid-Atlantic coast and near the inflection of an "S"-shaped thickness field (Fig. 3.41a). The entire snowband was situated along the cyclonic-shear side of a 250-hPa jet axis, and the exit region of an embedded jet streak overlay the surface cyclone (Fig. 3.41a). During the subsequent 12-h period, this cyclone deepened by ~8 hPa as it moved northeastward (not shown). In the middle troposphere, frontogenesis was present near the band axis within both the 850–700-hPa and 700–500-hPa layers at 1200 UTC (Figs. 3.41b,c), with an approximately upright axis of maximum frontogenesis spanning these layers. A closed cyclonic circulation extended upward to a position south (southwest) of the pivot zone in the 850–700-hPa layer (700–500-hPa layer) (Figs 3.41b,c). Relative humidity plots indicate that the snowband axis was adjacent to a slot–comma head interface through the 700–400-hPa layer (Figs. 3.42b–e) that sloped upward towards colder air.

A distinct warm–cold advection dipole, oriented in the along-isotherm and along-band direction, was present in the 850–700-hPa and 700–500-hPa layers at 1200 UTC (Fig. 3.43a,b). Within these layers, warm advection was present at the pivot zone and along most of the band, and warm advection maxima were positioned at the warm side of

the band axis. Consistent with thermal wind considerations, the pivot zone was characterized by pronounced veering wind with height (Fig. 3.44), and clockwise hodograph curvature was present through much of the 0–5-km AGL layer (Fig. 3.44, inset). A DGZ extended through a ~300-hPa layer (Fig. 3.44), contributing to the observed heavy snow at the pivot zone.

QG forcing for ascent was present along the snowband axis at 1200 UTC 6 February (Figs. 3.45a,d), more extensively in the 700–500-hPa layer (Fig. 3.45a). Q_s vectors in the 700–500-hPa and 850–700-hPa layers were downshear-directed and convergent at the pivot zone and along most of the band axis, with the largest Q_s vectors situated *upshear* of the pivot zone (Figs. 3.45b,e). A band-parallel region of Q_n-vector convergence was also present in both layers, with mainly frontolytical (frontogenetical) Q_n vectors in the region upshear (downshear) of the pivot zone (Figs. 3.45c,f).

24-h backward kinematic trajectories for parcels arriving along the band at both 700 and 500 hPa (Figs. 3.46a,b) are consistent with pronounced veering wind with height near the snowband. Time-integrated diffluence is also implied by the parcel cluster arriving at 700 hPa (Fig. 3.46a). Unlike the trajectories associated with the laterally translating and laterally quasi-stationary snowband cases, where parcels arriving at 500 hPa generally originated from lower levels than those arriving at 700 hPa (Figs. 3.30a,b and 3.38a,b), parcels arriving along the pivoting snowband at 500 hPa generally originated from *higher* levels than those arriving at 700 hPa (Figs. 3.46a,b).

3.3.4 Hybrid Snowband

A hybrid snowband was observed at 1200 UTC 12 December 2008 extending from central Pennsylvania to far eastern Ontario (Fig. 3.47). Animated 0.5° reflectivity mosaics indicated that this snowband moved northeastward with simultaneous along- and cross-axis motion that satisfied the classification criterion for hybrid snowbands (see section 2.2.1 and Fig. 2.3). Subtle counterclockwise rotation of the band axis was also observed, as evident by comparing the orientations of the band axis at 1100 and 1300 UTC in Fig. 3.47. However, no pivot zone existed at 1200 UTC, since an earth-relative center of rotation along the band axis was not observed, thereby precluding band classification as a *pivoting* band. Within the region swept by this band—from northern Pennsylvania to western New York—no pronounced snowfall accumulation gradients are evident in the 24-h snowfall accumulation plot ending at 1800 UTC 12 December 2008 (Fig. 3.48). The absence of a distinct snowfall accumulation gradient is consistent with the progressive cross-axis motion component associated with this snowband.

At 1200 UTC 12 December, the band was situated in the northwest quadrant of a sub-996-hPa surface cyclone near Long Island and beneath the entrance region of a 250-hPa jet streak (Fig. 3.49a). In the 850–700-hPa layer, the band axis was located adjacent to a region of frontogenesis along a sharp trough axis (Fig. 3.49b). Further aloft, in the 700–500-hPa layer, frontogenesis was present along the band axis amid confluent southwesterly flow (Fig. 3.49c). Relative humidity plots indicate that the band was positioned within the cyclone comma head region that sloped upward toward colder air in the 700–400-hPa layer (Figs. 3.50b–e).

Cold advection was present along the band axis within both the 850–700-hPa and 700–500-hPa layers at 1200 UTC 12 December (Figs. 3.51a,b). Both layers exhibited a

warm–cold advection dipole oriented in the along-isotherm and along-band direction (more noticeably at 850–700-hPa; Fig. 3.51a). Consistent with thermal wind considerations, winds backed with height at the band centroid in the middle troposphere (Fig. 3.52). A DGZ spanning ~200-hPa was also present at the band centroid.

The band axis was situated at the western extent of QG forcing for ascent in the 700–500-hPa layer (Fig. 3.53a) and in a region of QG forcing for descent in the 850–700-hPa layer (Fig. 3.53d). Q_s vectors were downshear-directed along the band axis in both layers (Figs. 3.53b,e), indicating counterclockwise rotation of isentropes that was consistent with the observed rotation of the band axis (Fig. 3.47). Q_n vectors along the band in both layers were frontogenetical and contributed to band-parallel regions of Q_n-vector convergence (Figs. 3.53c,f).

24-h backward kinematic trajectories indicate that parcels arrived along the band axis at 700 hPa with a history of descent (Fig. 3.54a). Parcels arriving at 500 hPa, however, underwent gradual ascent as they approached from the southwest (Fig. 3.54b). Backing flow with height near the band axis within the 700–500-hPa layer is implied by these respective clusters of trajectories.

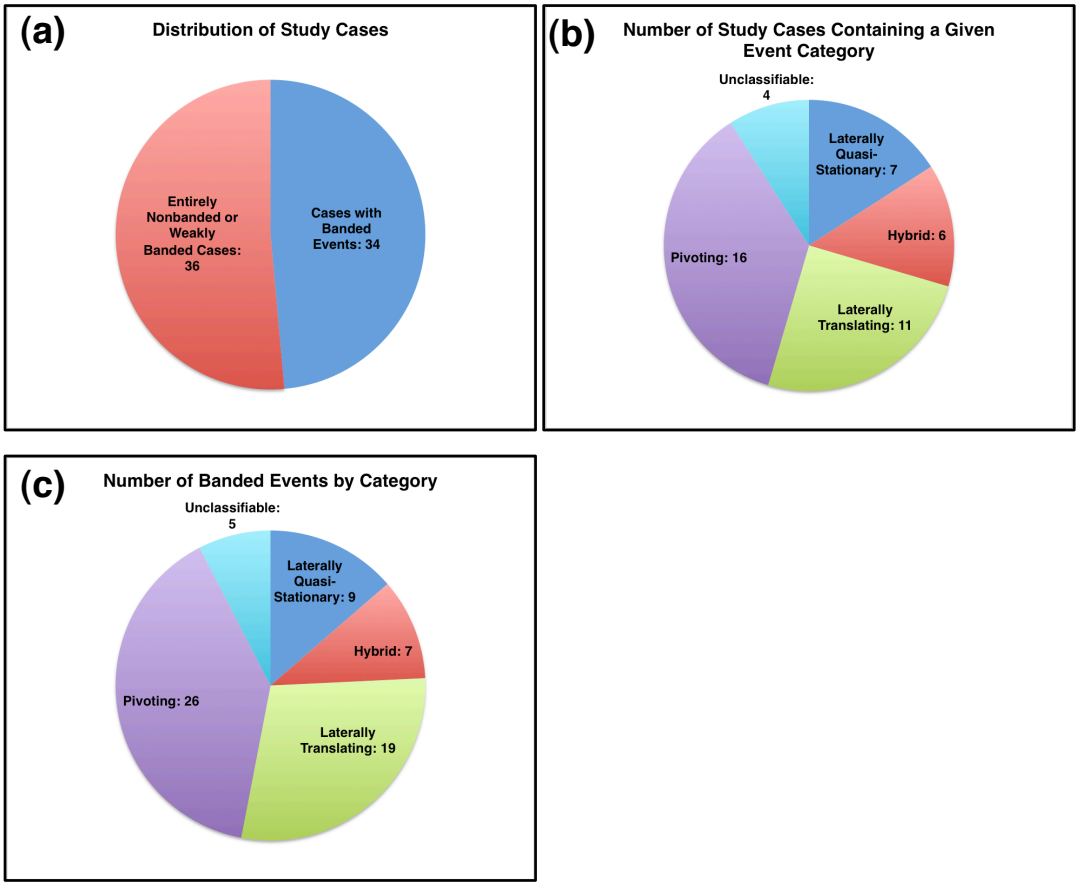

Fig. 3.1. (a) Distribution of the 70 study cases between those with and without banded events. (b) The number of study cases across which a given banded event category was manifested. (c) The distribution of banded events by category, summed across all study cases.

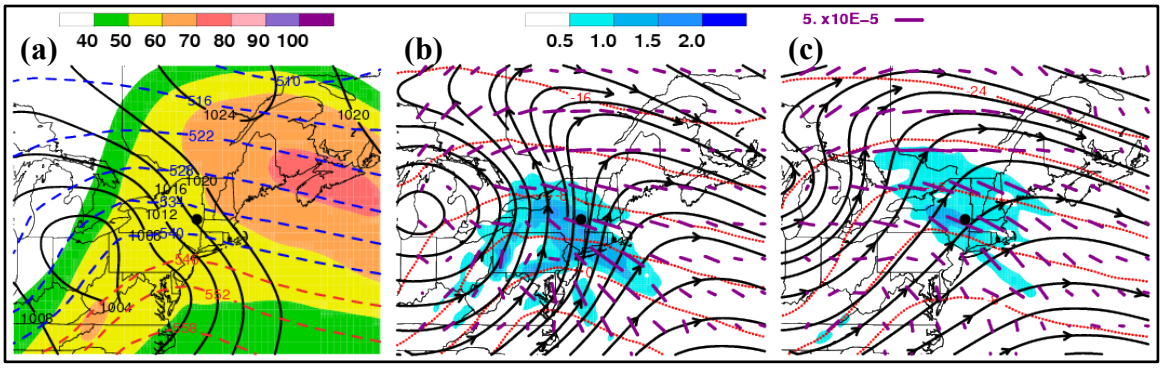

Fig. 3.2. Laterally translating category composite (N = 17) (a) MSLP (black contours, hPa), 1000–500-hPa thickness (dashed contours, dam), and 250-hPa wind speed (fills, m s^{-1}); (b) 850–700-hPa layer-mean streamlines (black contours), temperature (red contours, °C), axes of dilatation [purple tick marks, length scaled by resultant deformation, reference axis (5×10^{-5} s^{-1}) at top right], and Petterssen frontogenesis [fills, K $(100\ km)^{-1}$ $(3\ h)^{-1}$]; (c) as in (b), except for the 700–500-hPa layer. In all panels, the heavy black dot marks the composite band centroid.

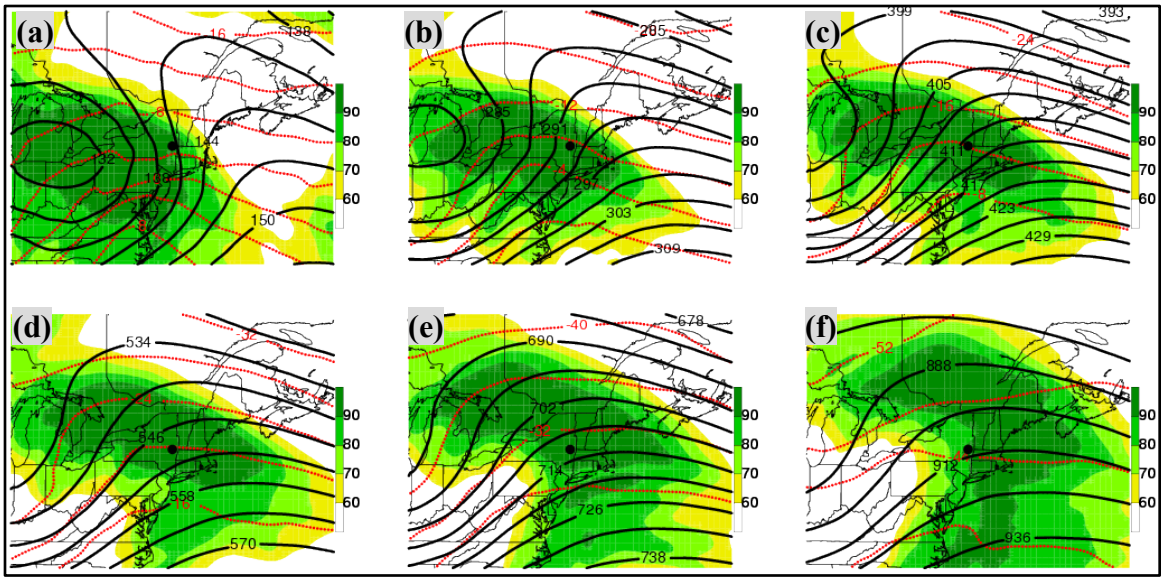

Fig. 3.3. Laterally translating category composite (N = 17) geopotential height (black contours, dam), temperature (red contours, °C), and relative humidity (fills, percent w.r.t. water, ice, or mixed phase, as determined by CFSR) at (a) 850 hPa; (b) 700 hPa; (c) 600 hPa; (d) 500 hPa; (e) 400 hPa; and (f) 300 hPa. In all panels, the heavy black dot marks the composite band centroid.

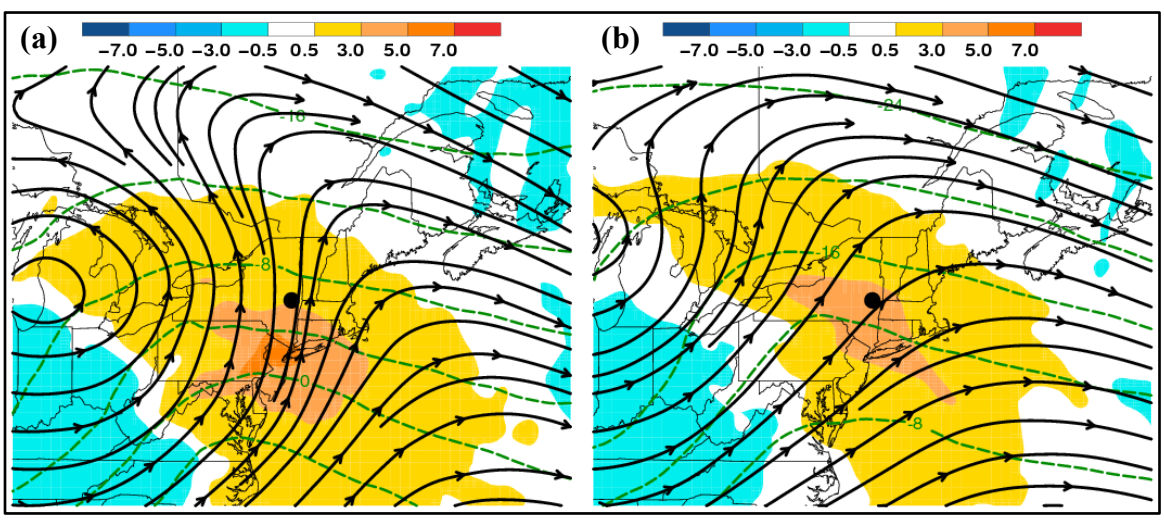

Fig. 3.4. Laterally translating category composite (N = 17) layer-mean streamlines (black contours), temperature (green contours, °C), and temperature advection [fills, K (3 h)$^{-1}$] for the (a) 850–700-hPa layer and (b) 700–500-hPa layer. In both panels, the heavy black dot marks the composite band centroid.

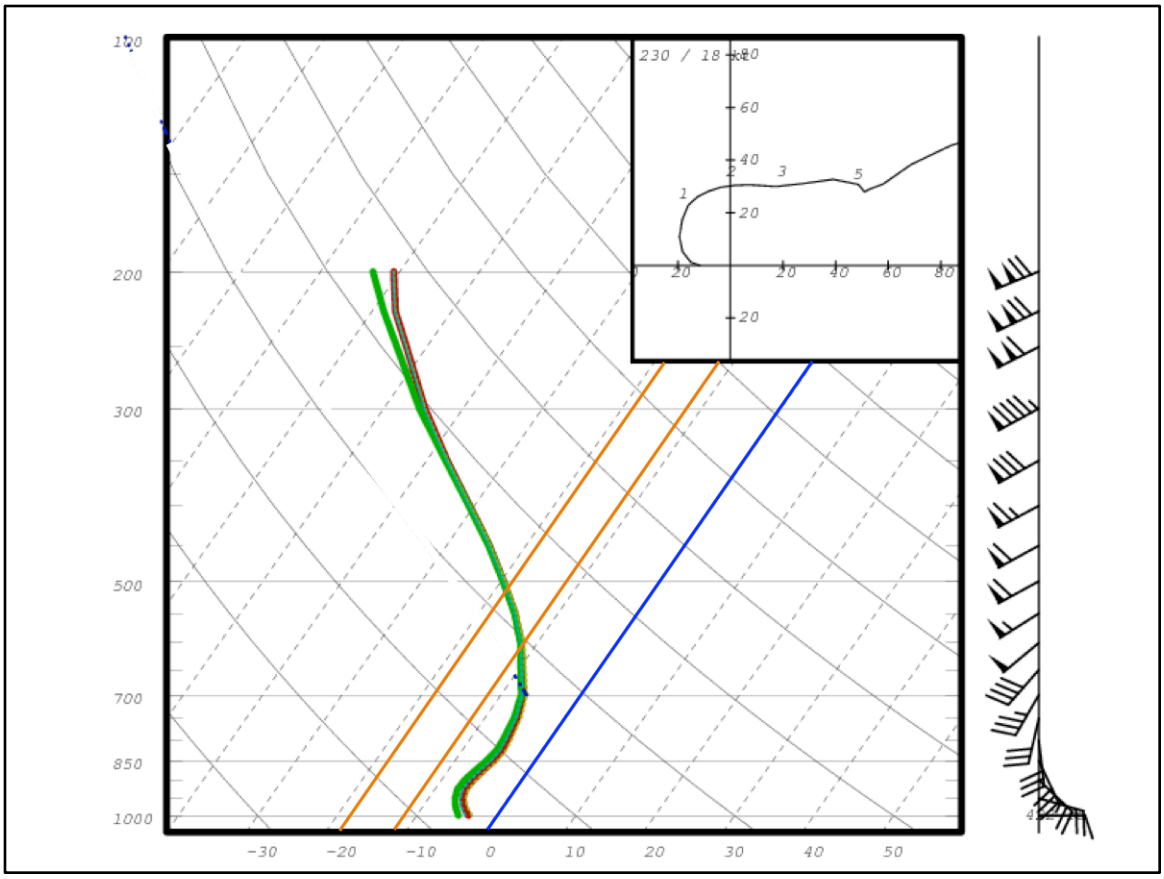

Fig. 3.5. Profile at the band centroid of the laterally translating category composite (N = 17) plotted on a skew *T*–log*p* diagram. Orange isotherms outline the dendritic growth zone (DGZ, defined as the layer of near-saturation between the −12 and −18°C isotherms). The associated hodograph is inset at top right with the curve labeled in km MSL and the axes labeled in kt. Corresponding wind barbs (standard convention, in kt) are shown at right.

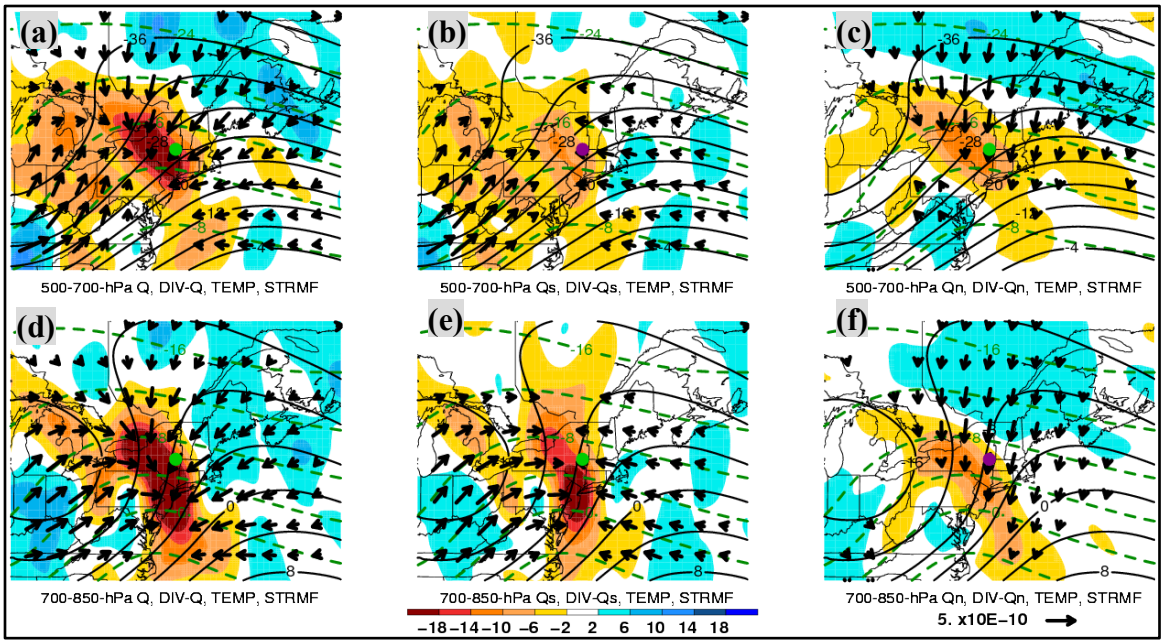

Fig. 3.6. Laterally translating category composite (N = 17) 700–500-hPa layer-mean (a) Q vectors (arrows, magnitudes $\geq 1 \times 10^{-10}$ K m^{-1} s^{-1}, reference vector at bottom right), Q-vector divergence (fills, 10^{-16} K m^{-2} s^{-1}), streamfunction (black contours, 10^6 m^2 s^{-1}), and temperature (green contours, °C); (b) as in (a) except for Q_s vectors; (c) as in (a), except for Q_n vectors; (d)–(f) as in (a)–(c), respectively, except for the 850–700-hPa layer mean. In all panels, the heavy dot (green or purple) marks the composite band centroid.

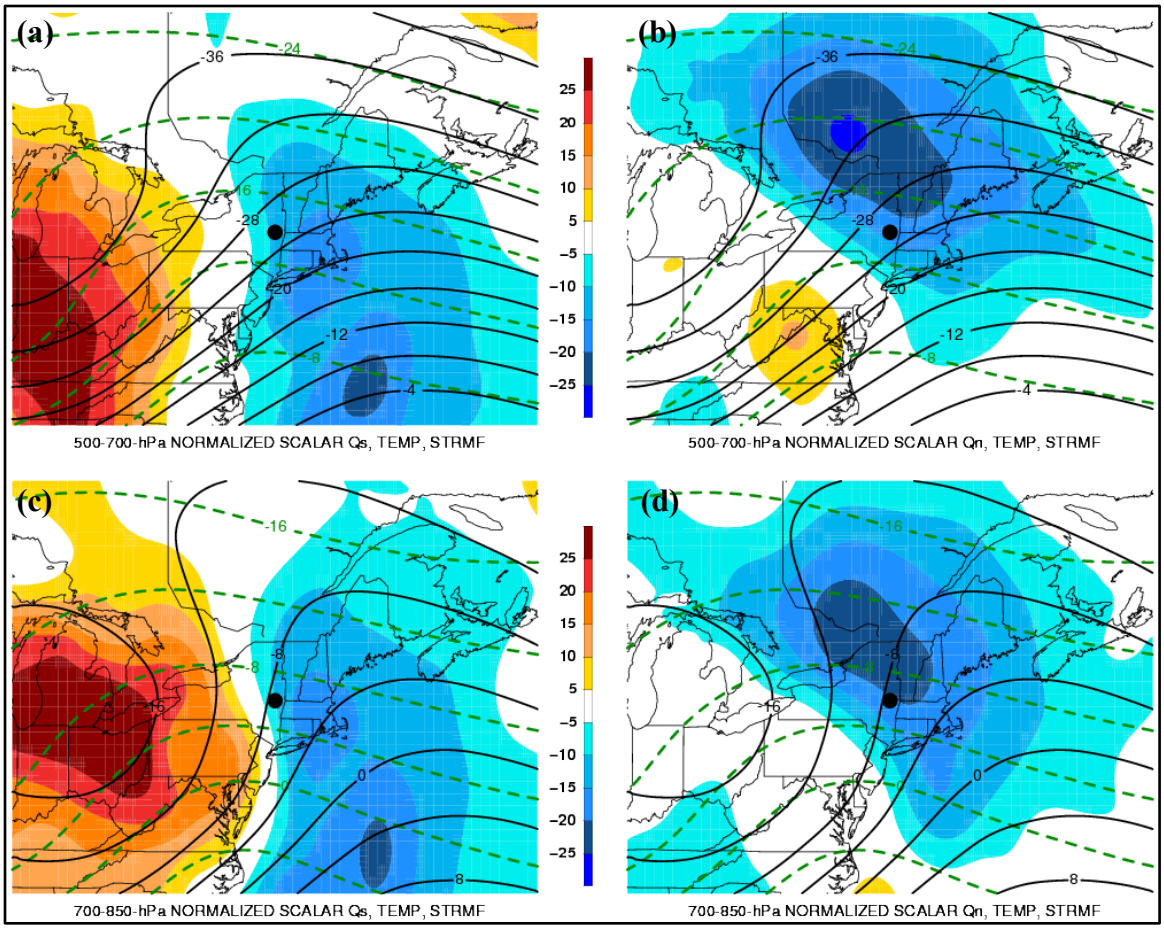

Fig. 3.7. Laterally translating category composite (N = 17) (a) 700–500-hPa layer-mean normalized Q_s (fills, 10^{-6} s^{-1}), temperature (dashed green contours, °C), and streamfunction (black contours, 10^6 m^2 s^{-1}); (b) as in (a), except for normalized Q_n; (c) and (d) as in (a) and (b), respectively, except for the 850–700-hPa layer mean. In all panels, the heavy black dot marks the composite band centroid.

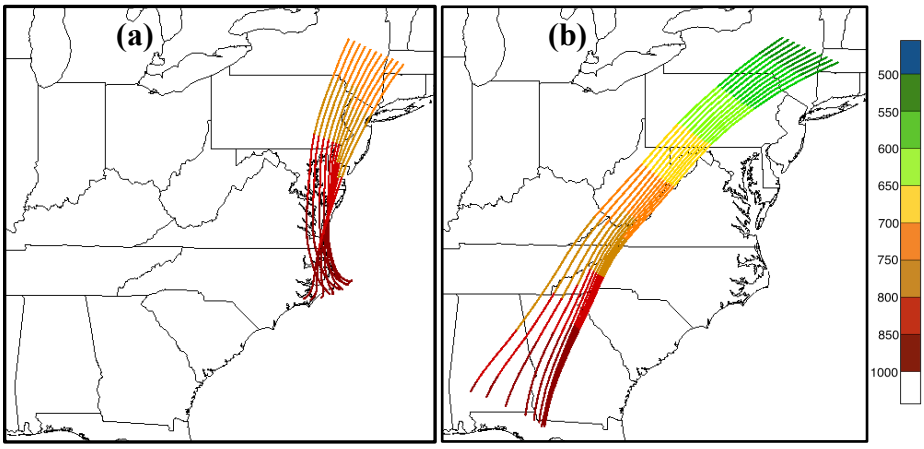

Fig. 3.8. Laterally translating category composite (N = 17) 24-h backward kinematic trajectories arriving along the mean band axis at (a) 700 hPa and (b) 500 hPa. Trajectory pressure (hPa) is shown according to color bar.

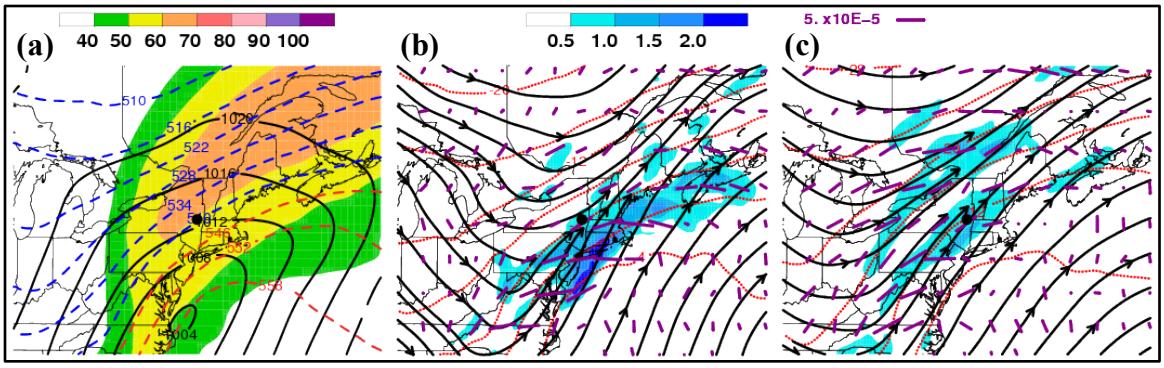

Fig. 3.9. As in Fig. 3.2, except for the laterally quasi-stationary category composite (N = 8).

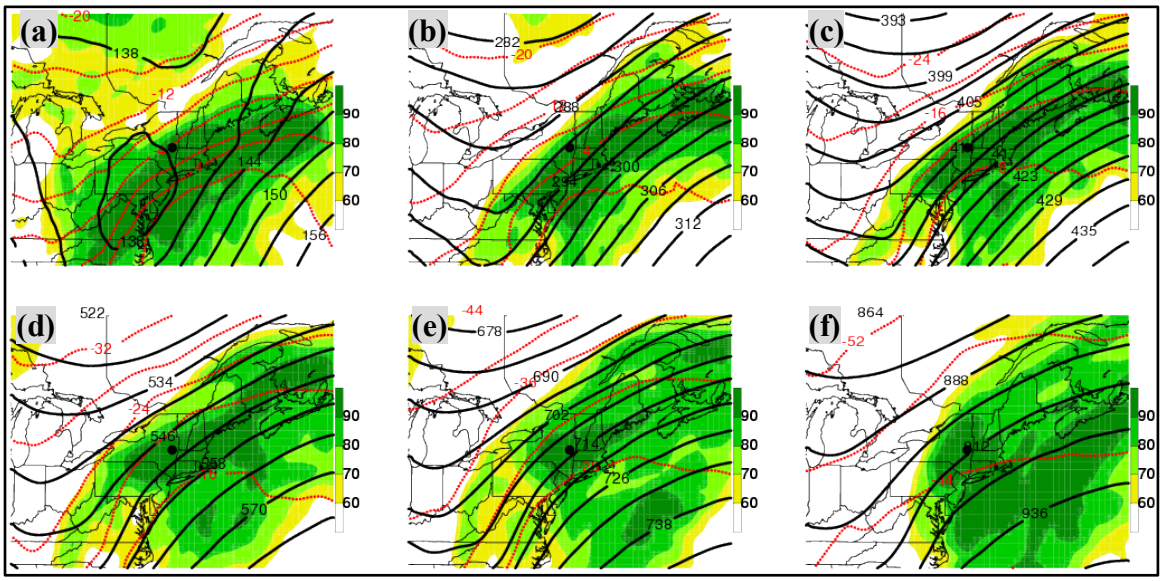

Fig. 3.10. As in Fig. 3.3, except for the laterally quasi-stationary category composite (N = 8).

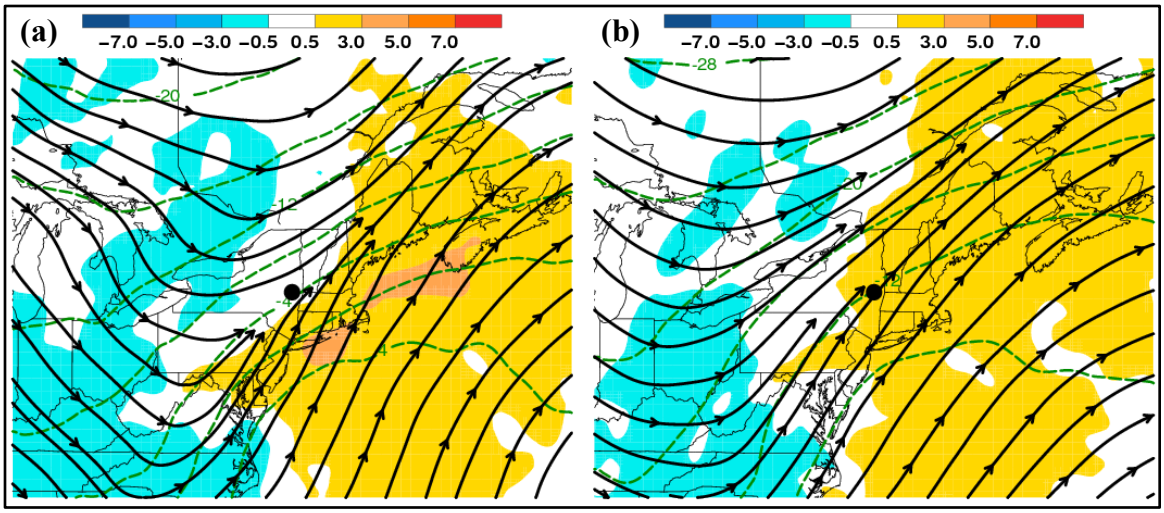

Fig. 3.11. As in Fig. 3.4, except for the laterally quasi-stationary category composite (N = 8).

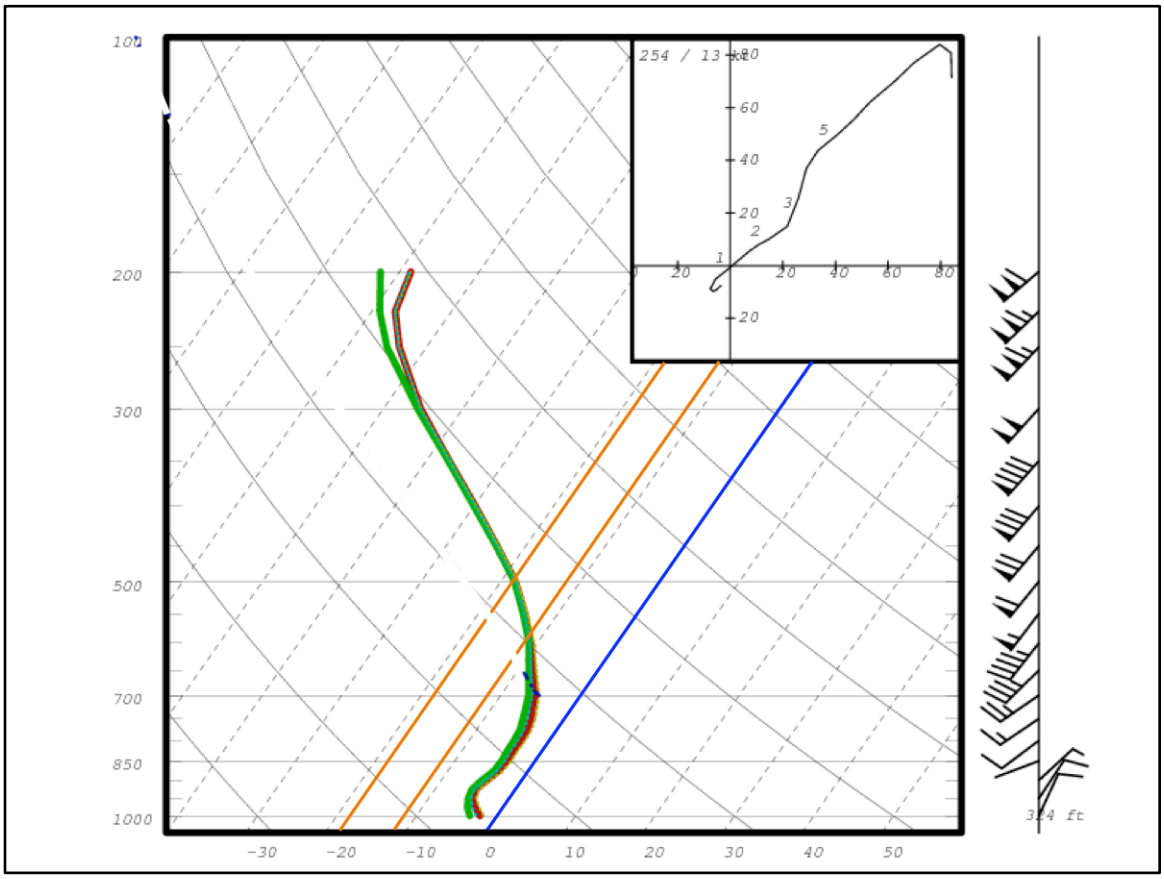

Fig. 3.12. As in Fig. 3.5, except for the laterally quasi-stationary category composite (N = 8).

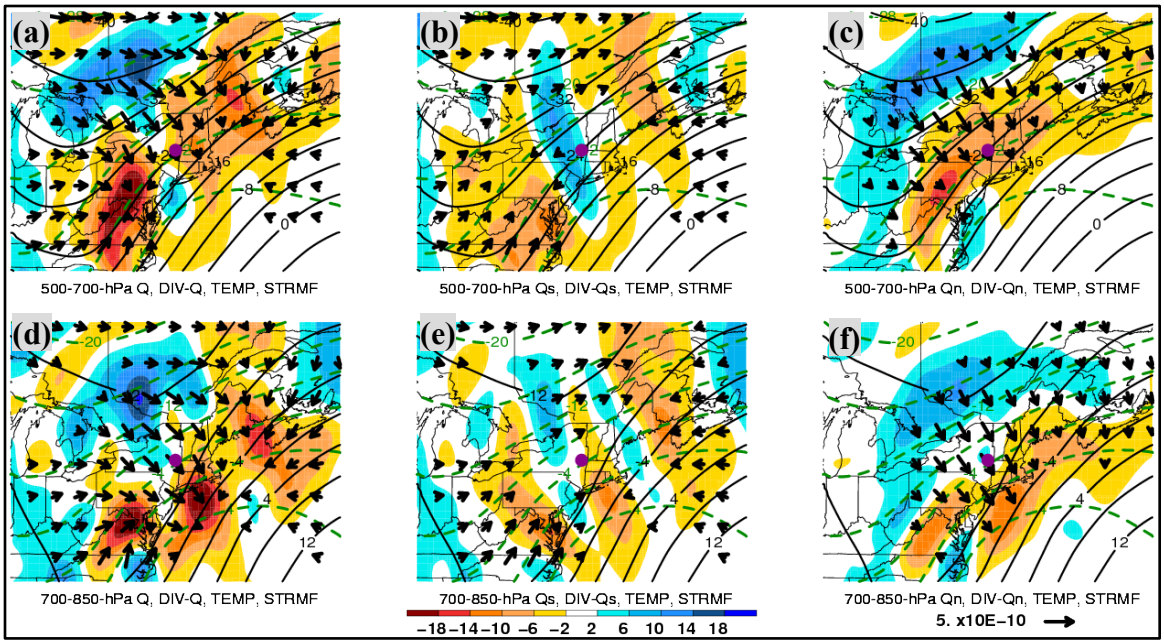

Fig. 3.13. As in Fig. 3.6, except for the laterally quasi-stationary category composite (N = 8).

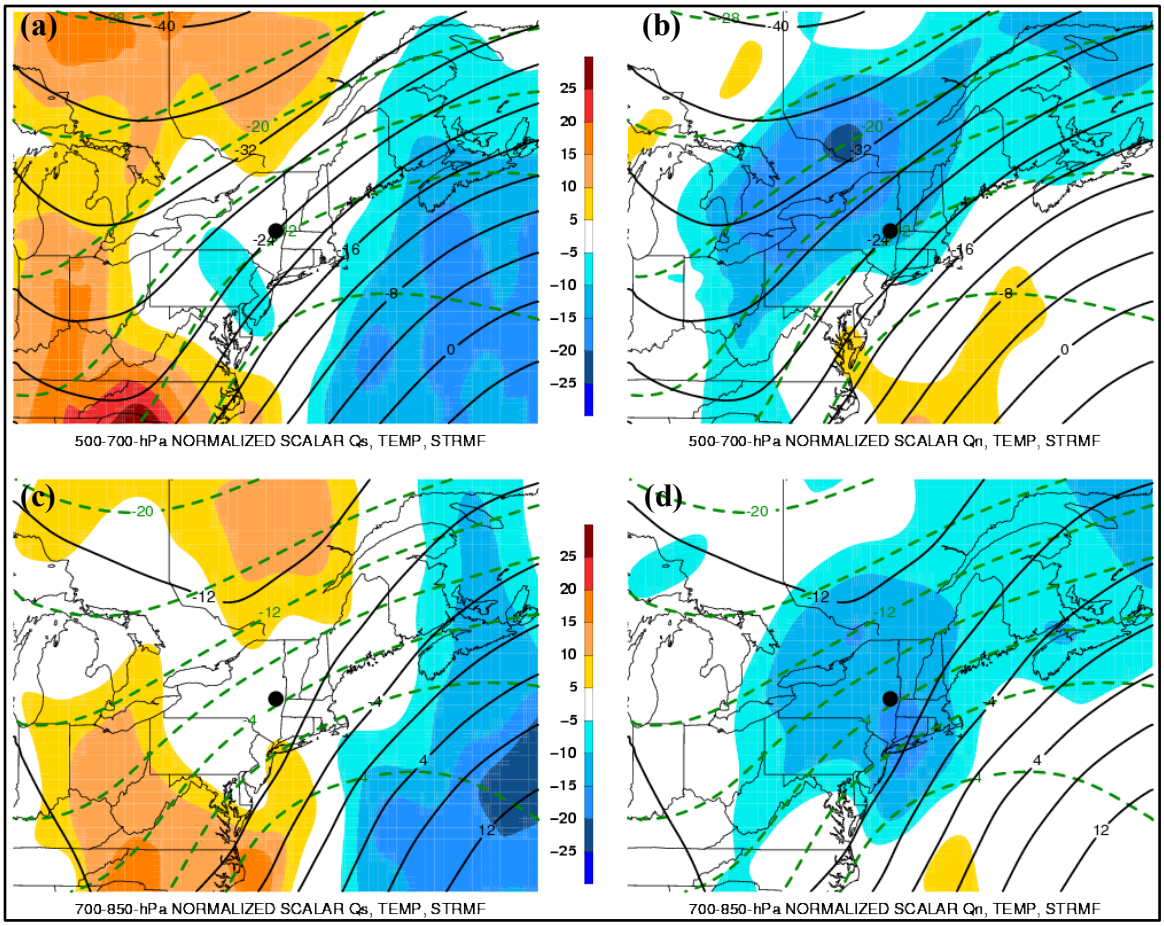

Fig. 3.14. As in Fig. 3.7, except for the laterally quasi-stationary category composite (N = 8).

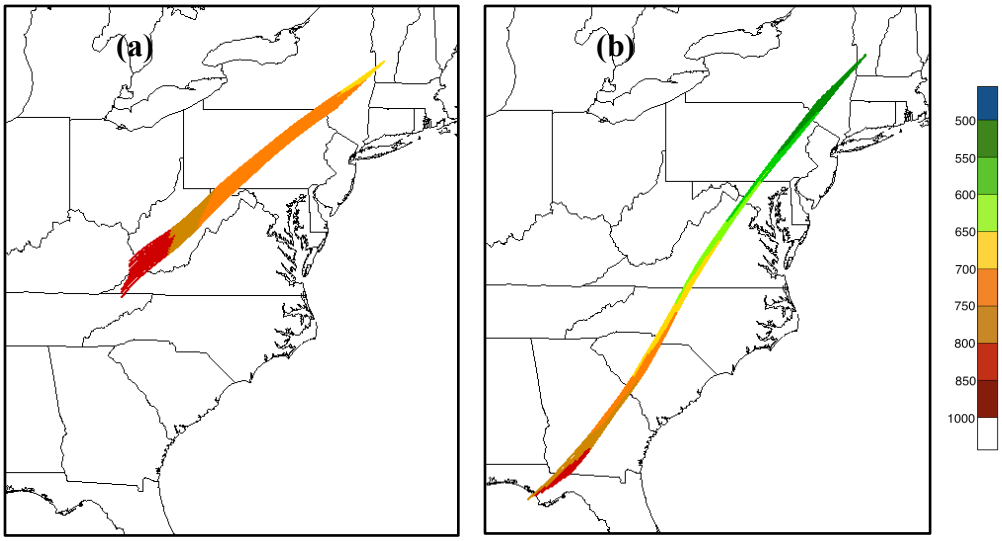

Fig. 3.15. As in Fig. 3.8, except for the laterally quasi-stationary category composite (N = 8).

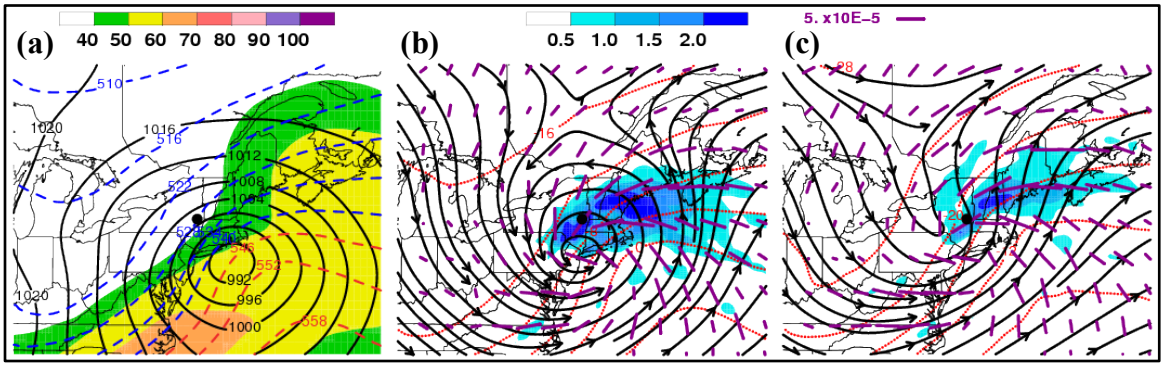

Fig. 3.16. As in Fig. 3.2, except for the pivoting category composite (N = 18). In all panels, the heavy black dot marks the composite pivot zone.

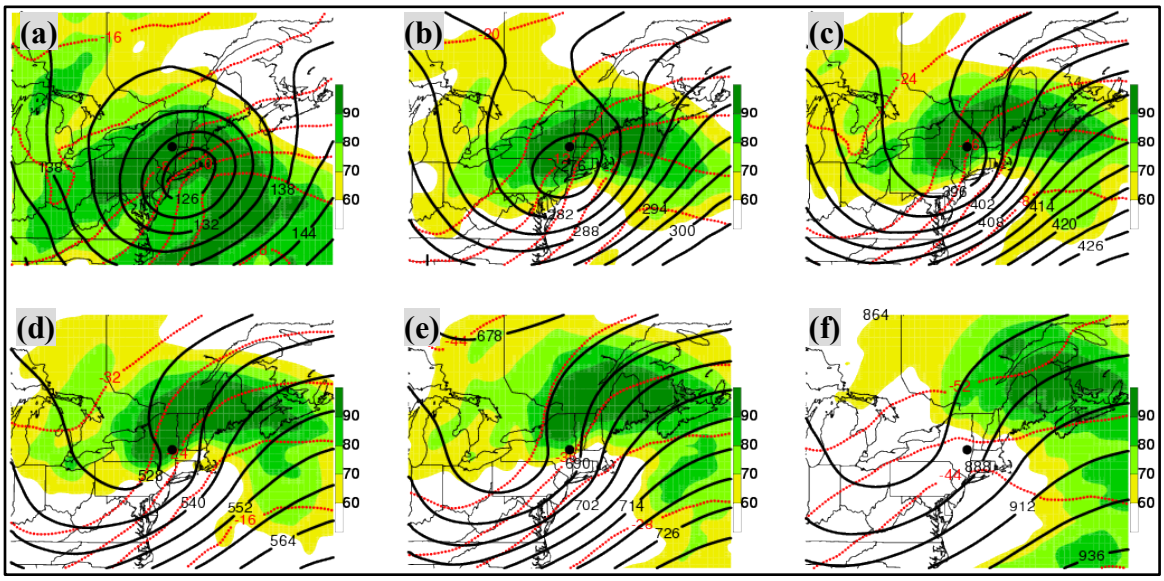

Fig. 3.17. As in Fig. 3.3, except for the pivoting category composite (N = 18). In all panels, the heavy black dot marks the composite pivot zone.

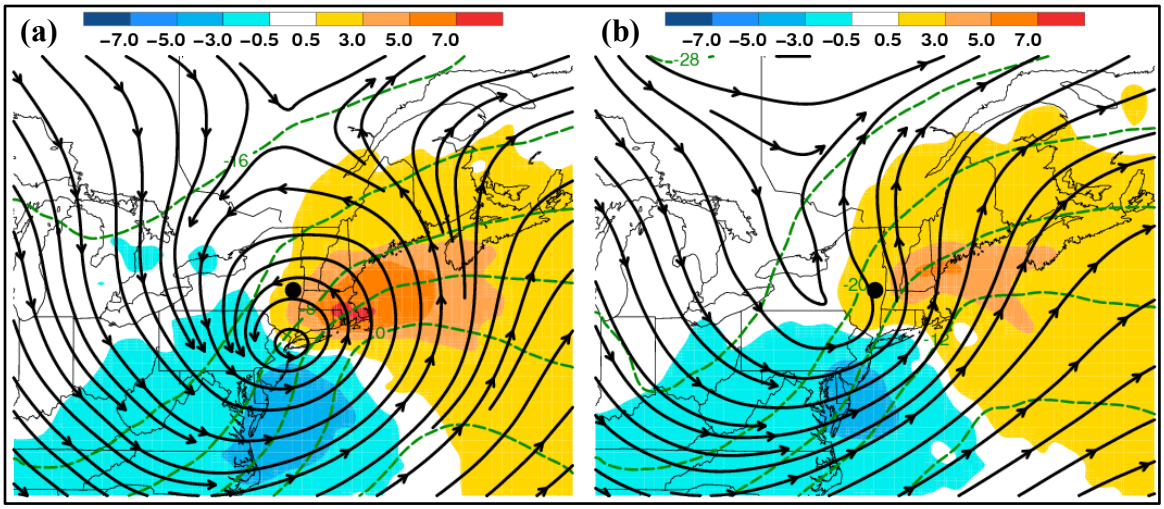

Fig. 3.18. As in Fig. 3.4, except for the pivoting category composite (N = 18). In both panels, the heavy black dot marks the composite pivot zone.

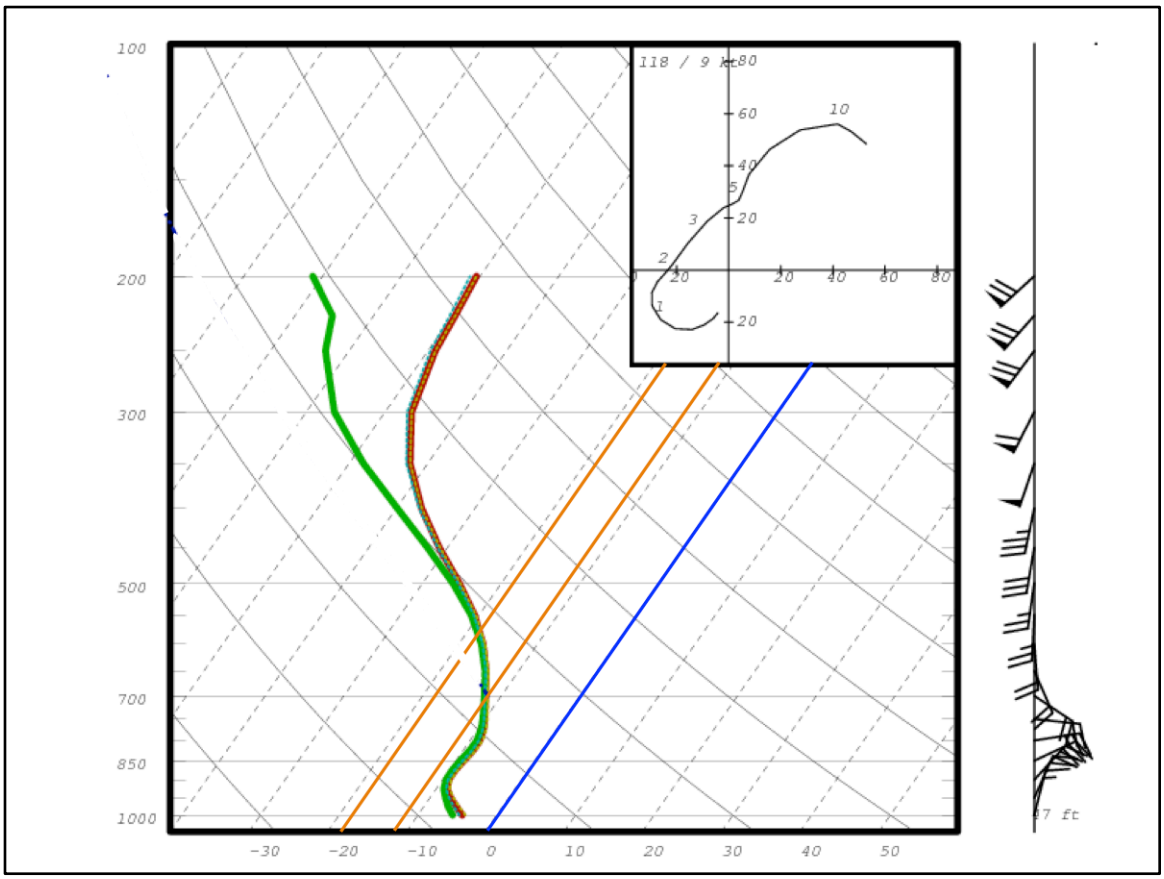

Fig. 3.19. As in Fig. 3.5, except for the pivoting category composite (N = 18).

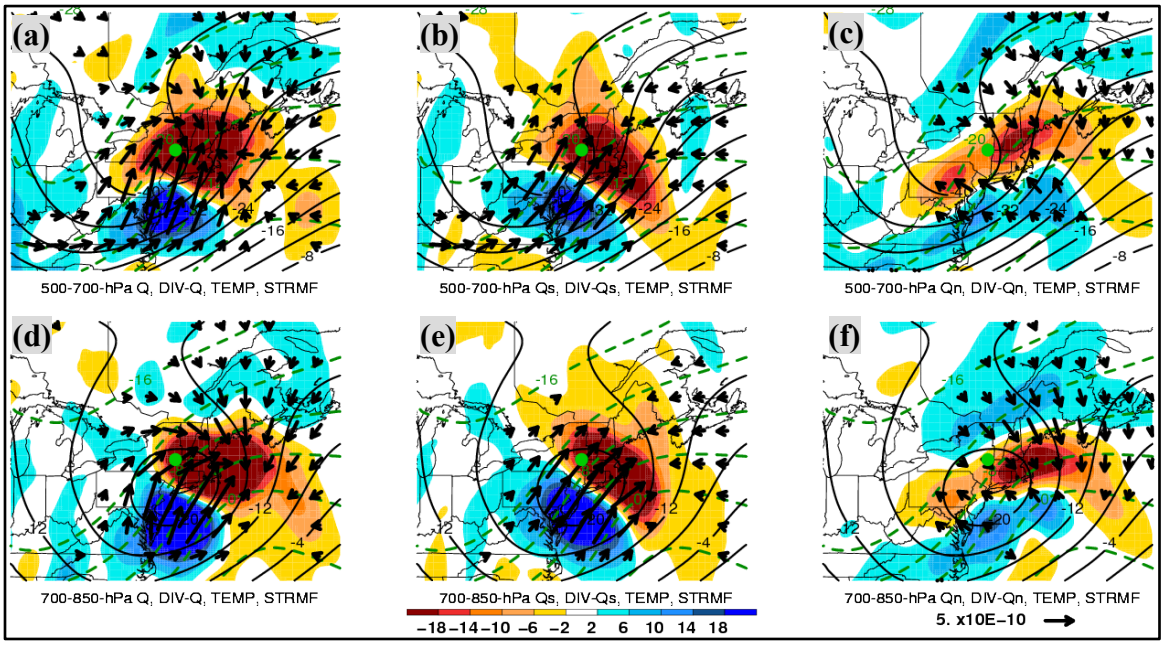

Fig. 3.20. As in Fig. 3.6, except for the pivoting category composite (N = 18). In all panels, the heavy green dot marks the composite pivot zone.

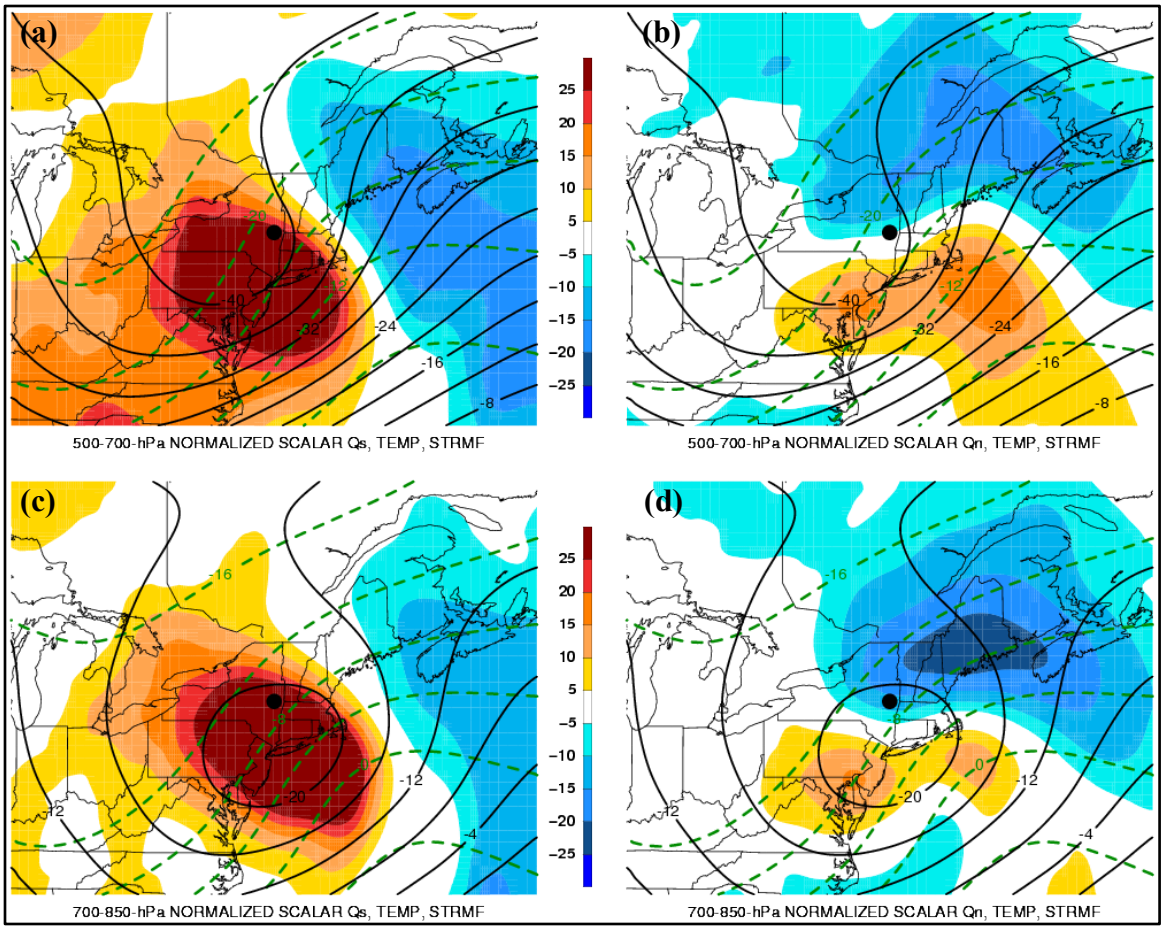

Fig. 3.21. As in Fig. 3.7, except for the pivoting category composite (N = 18). In all panels, the heavy black dot marks the composite pivot zone.

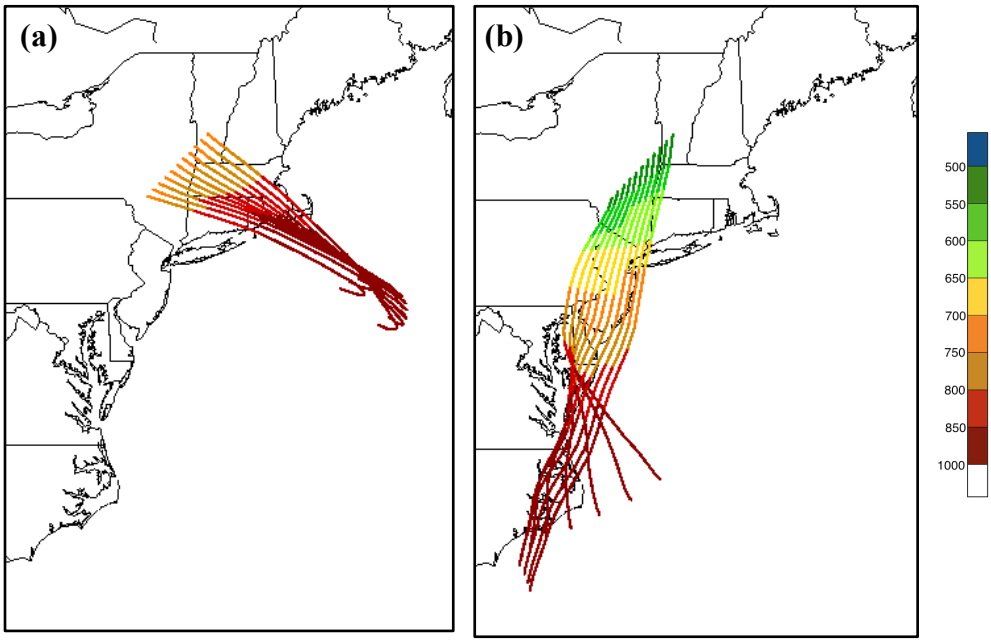

Fig. 3.22. As in Fig. 3.8, except for the pivoting category composite (N = 18).

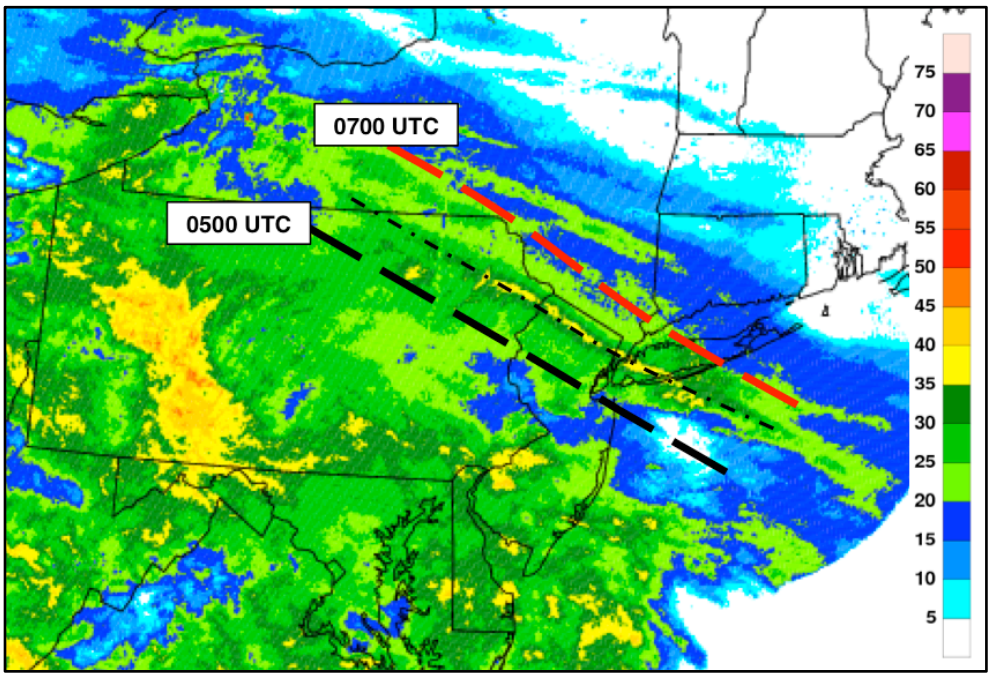

Fig. 3.23. Radar reflectivity (dB*Z*) at 0600 UTC 9 Dec 2009. Dash–dot pattern denotes the axis of the laterally translating snowband discussed in the text. The axis of the same snowband 1 h before (1 h after) the mosaic time is shown in dashed black (dashed red), as labeled.

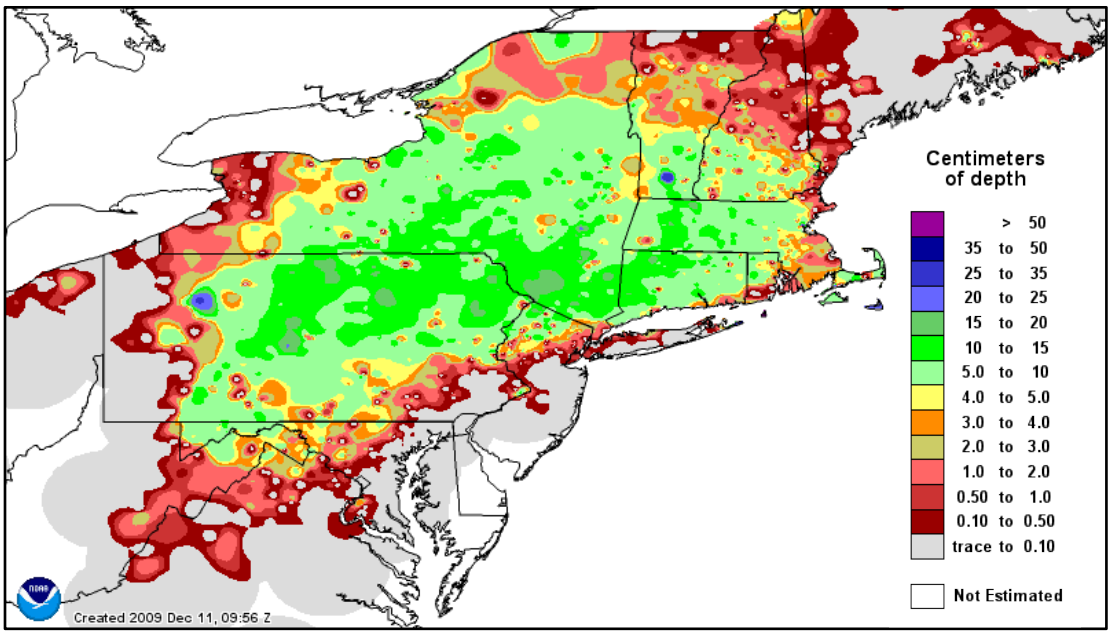

Fig. 3.24. 24-h snowfall accumulation (cm) ending at 1200 UTC 9 Dec 2009.

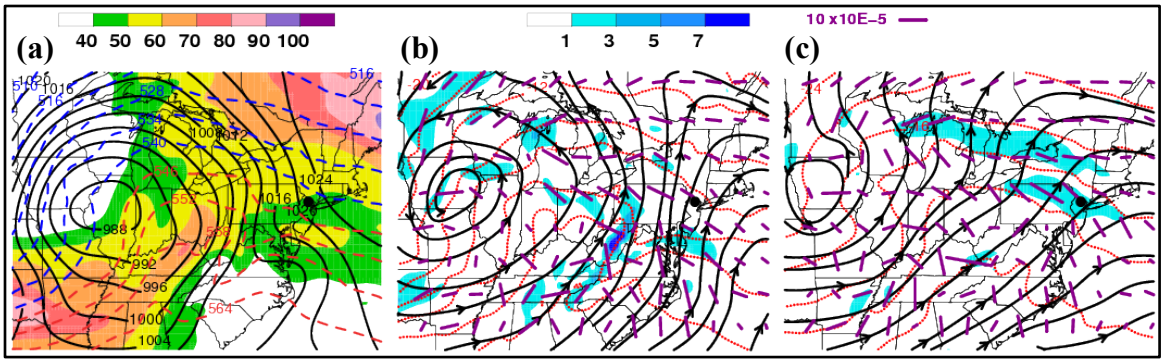

Fig. 3.25. As in Fig. 3.2, except at 0600 UTC 9 Dec 2009. The reference axis of dilatation (top right) represents resultant deformation of $10 \times 10^{-5}\ s^{-1}$. In all panels, the heavy black dot marks the centroid of the laterally translating snowband.

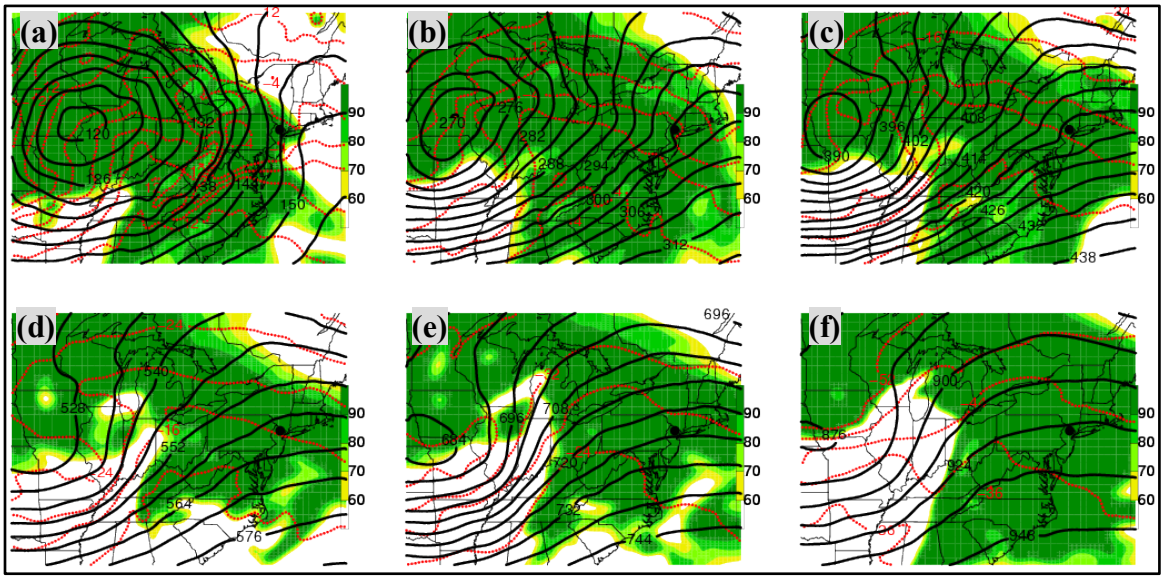

Fig. 3.26. As in Fig. 3.3, except at 0600 UTC 9 Dec 2009. In all panels, the heavy black dot marks the centroid of the laterally translating snowband.

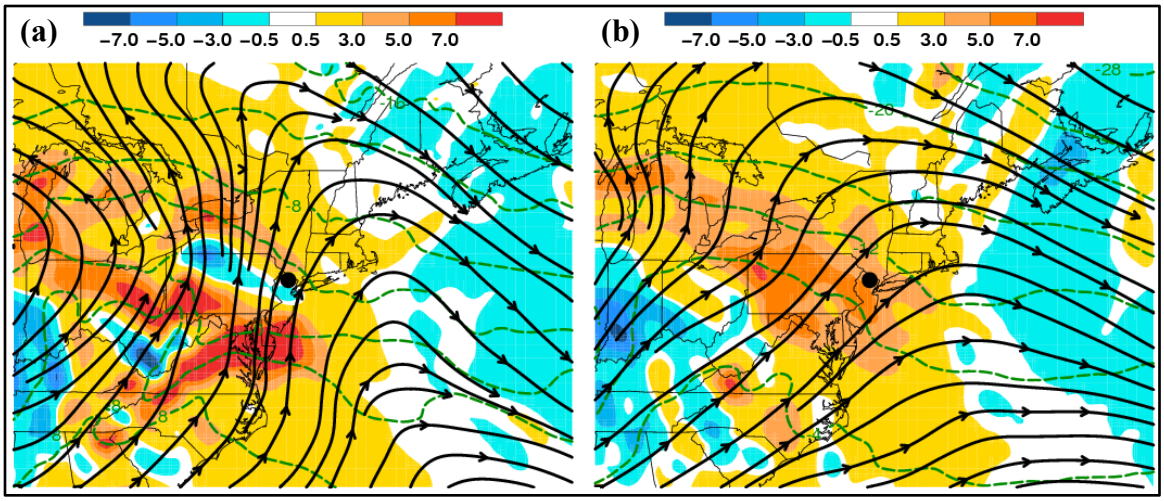

Fig. 3.27. As in Fig. 3.4, except at 0600 UTC 9 Dec 2009. In both panels, the heavy black dot marks the centroid of the laterally translating snowband.

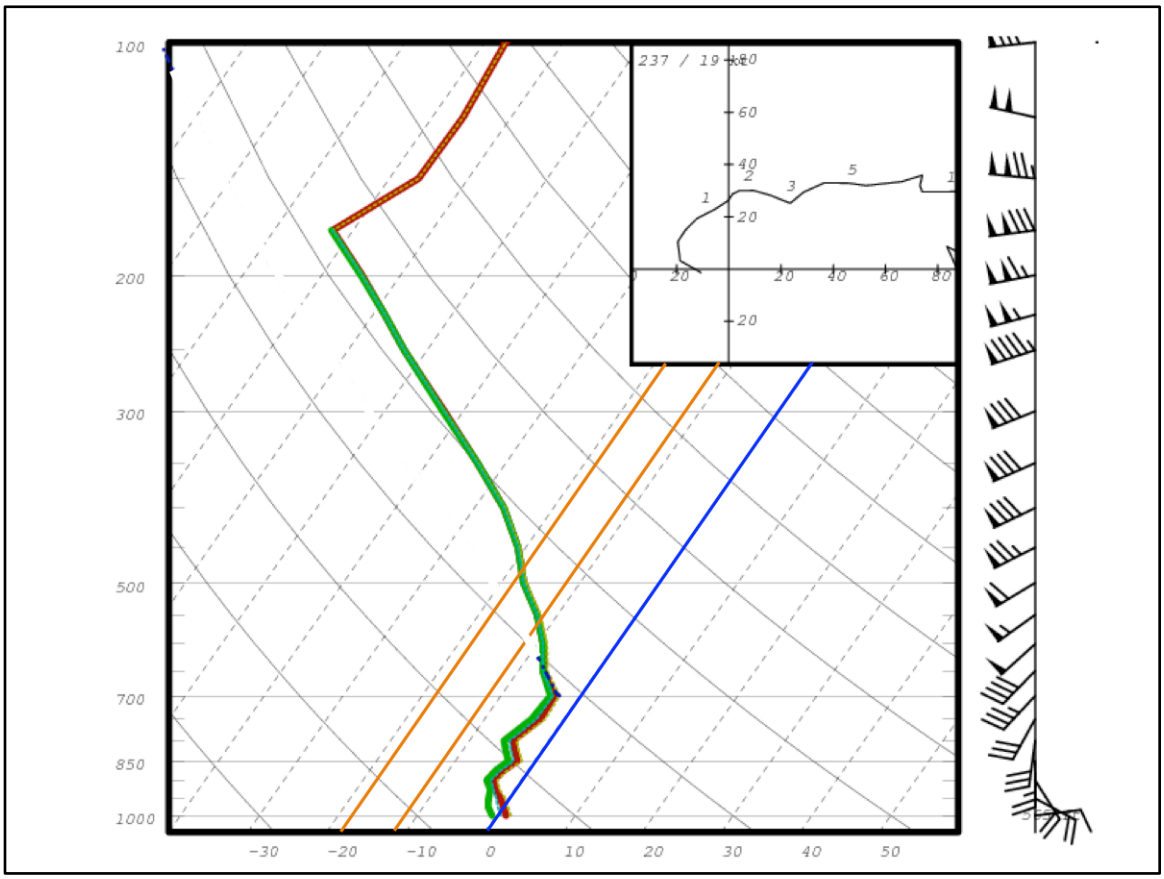

Fig. 3.28. As in Fig. 3.5, except at the centroid of the laterally translating snowband at 0600 UTC 9 Dec 2009. Centroid location is shown by black dots in Figs. 3.25–3.27.

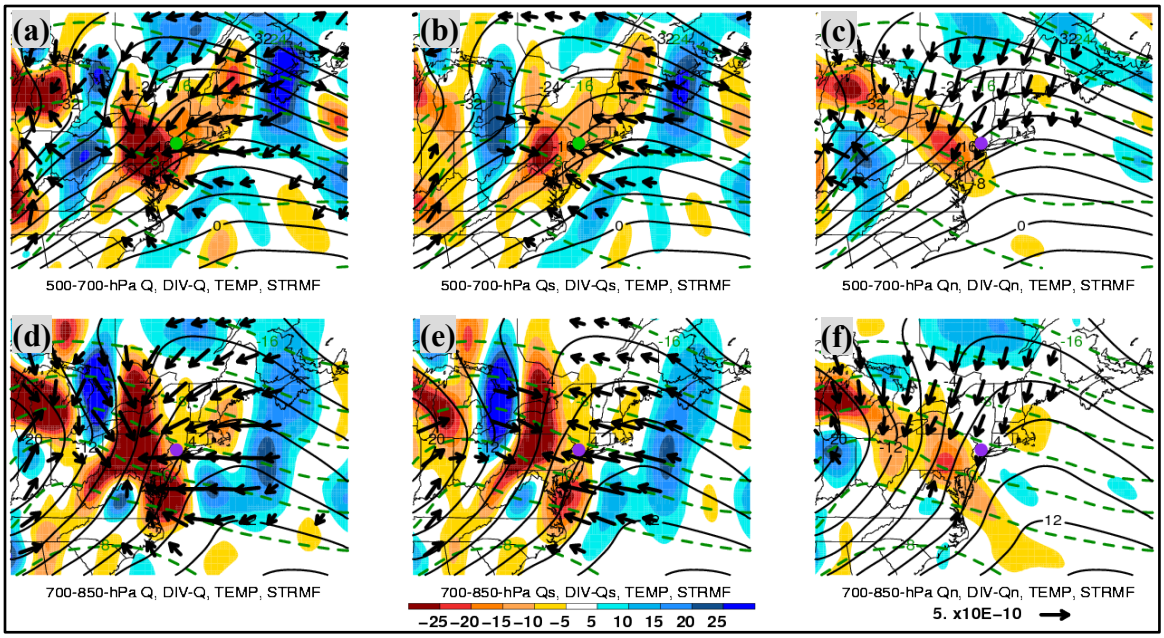

Fig. 3.29. As in Fig. 3.6, except at 0600 UTC 9 Dec 2009. Q vectors with magnitudes $\geq 2 \times 10^{-10}$ K m^{-1} s^{-1} are plotted. In all panels, the heavy dot (green or purple) marks the centroid of the laterally translating snowband.

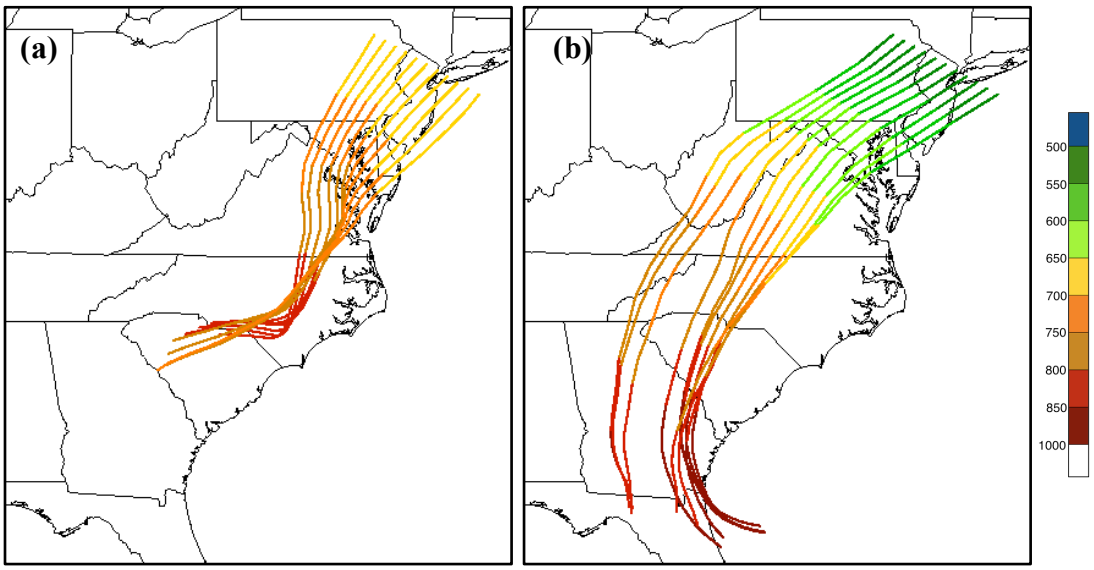

Fig. 3.30. As in Fig. 3.8, except for parcels arriving along the laterally translating snowband at 0600 UTC 9 Dec 2009.

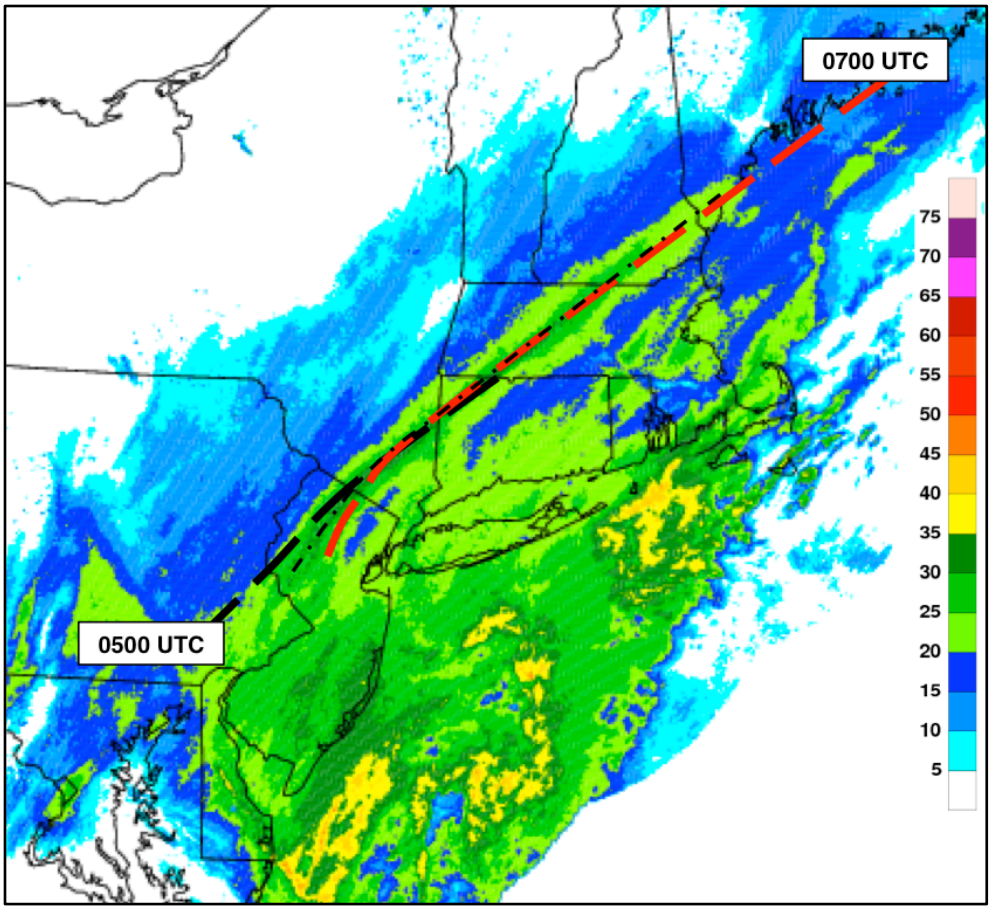

Fig. 3.31. Radar reflectivity (dB*Z*) at 0600 UTC 2 Mar 2009. Dash–dot pattern denotes the axis of the laterally quasi-stationary snowband discussed in the text. The axis of the same snowband 1 h before (1 h after) the mosaic time is shown in dashed black (dashed red), as labeled.

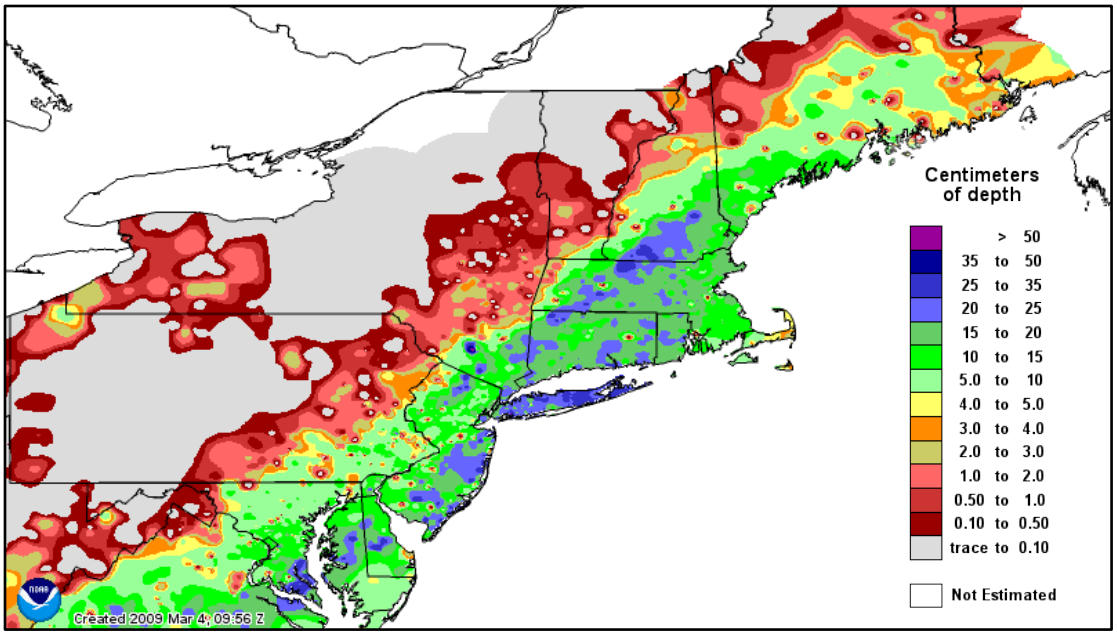

Fig. 3.32. 24-h snowfall accumulation (cm) ending at 1200 UTC 2 Mar 2009.

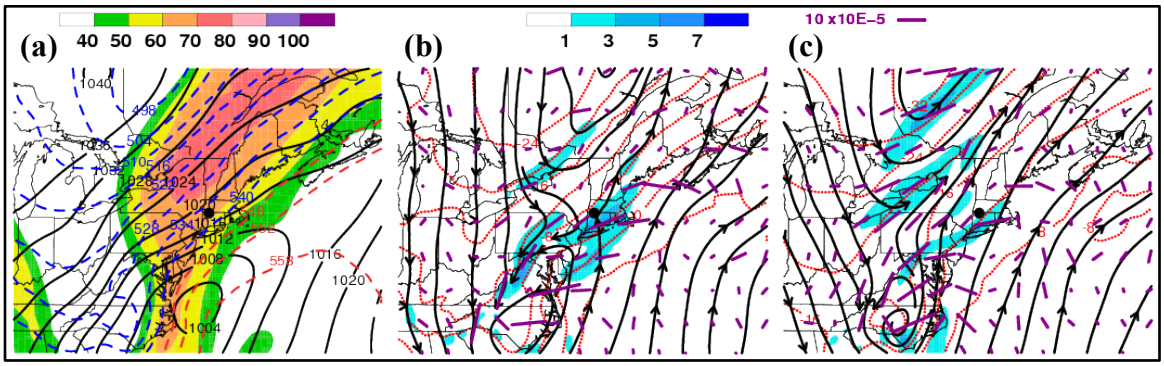

Fig. 3.33. As in Fig. 3.2, except at 0600 UTC 2 Mar 2009. The reference axis of dilatation (top right) represents resultant deformation of $10 \times 10^{-5}\ s^{-1}$. In all panels, the heavy black dot marks the centroid of the laterally quasi-stationary snowband.

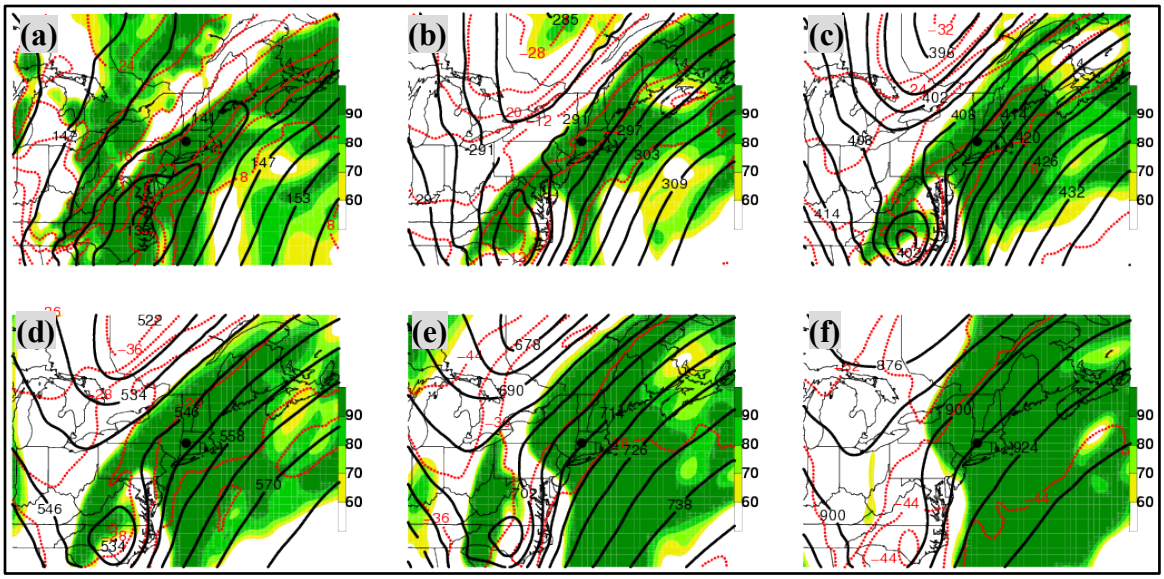

Fig. 3.34. As in Fig. 3.3, except at 0600 2 Mar 2009. In all panels, the heavy black dot marks the centroid of the laterally quasi-stationary snowband.

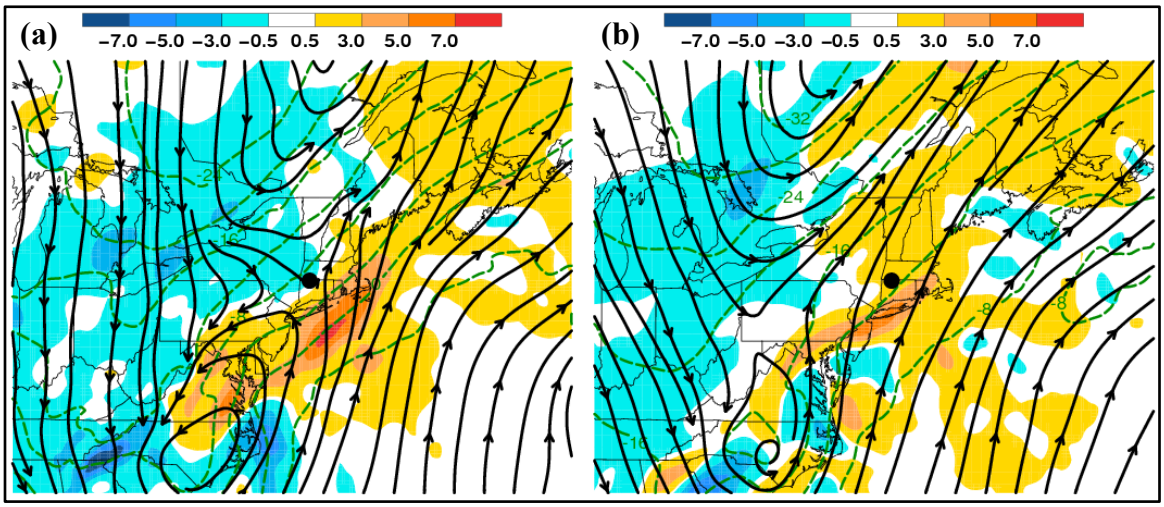

Fig. 3.35. As in Fig. 3.4, except at 0600 2 Mar 2009. In both panels, the heavy black dot marks the centroid of the laterally quasi-stationary snowband.

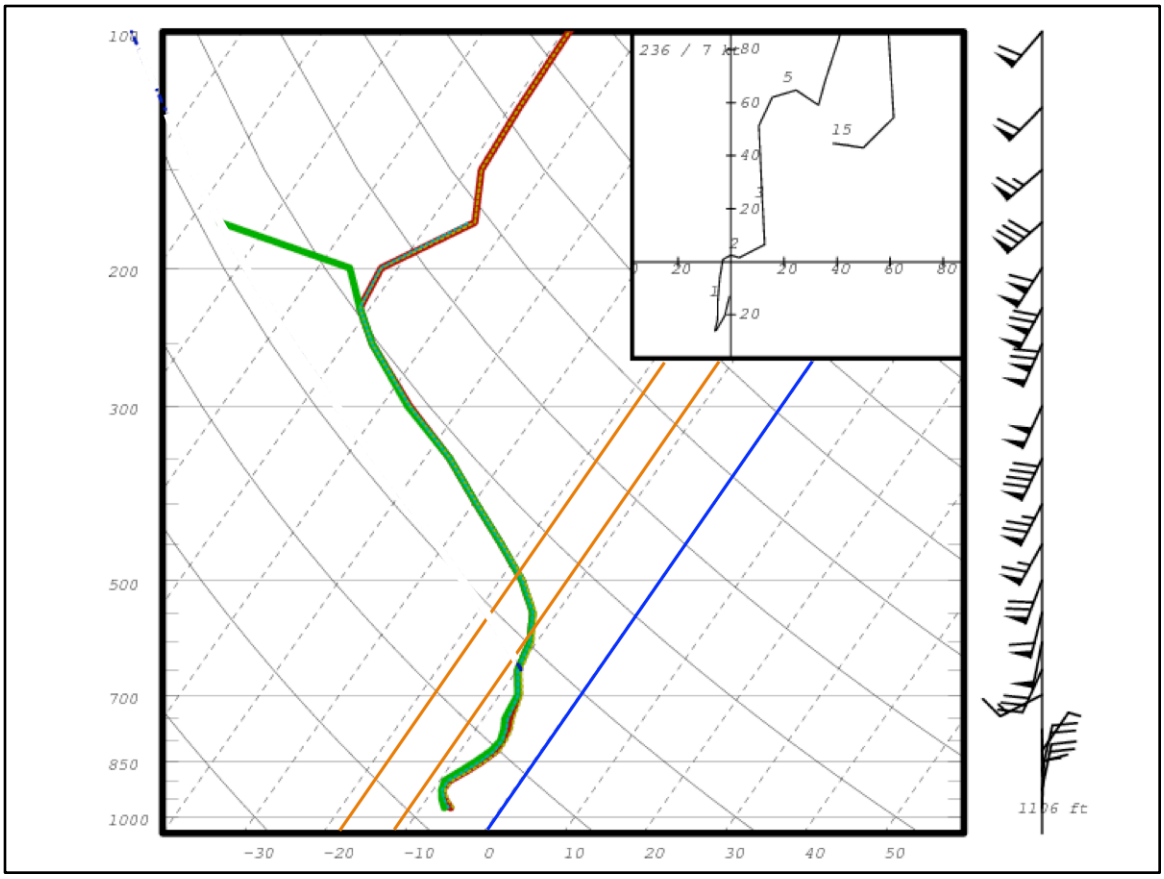

Fig. 3.36. As in Fig. 3.5, except at the centroid of the laterally quasi-stationary snowband at 0600 UTC 2 Mar 2009. Centroid location is shown by black dots in Figs. 3.33–3.35.

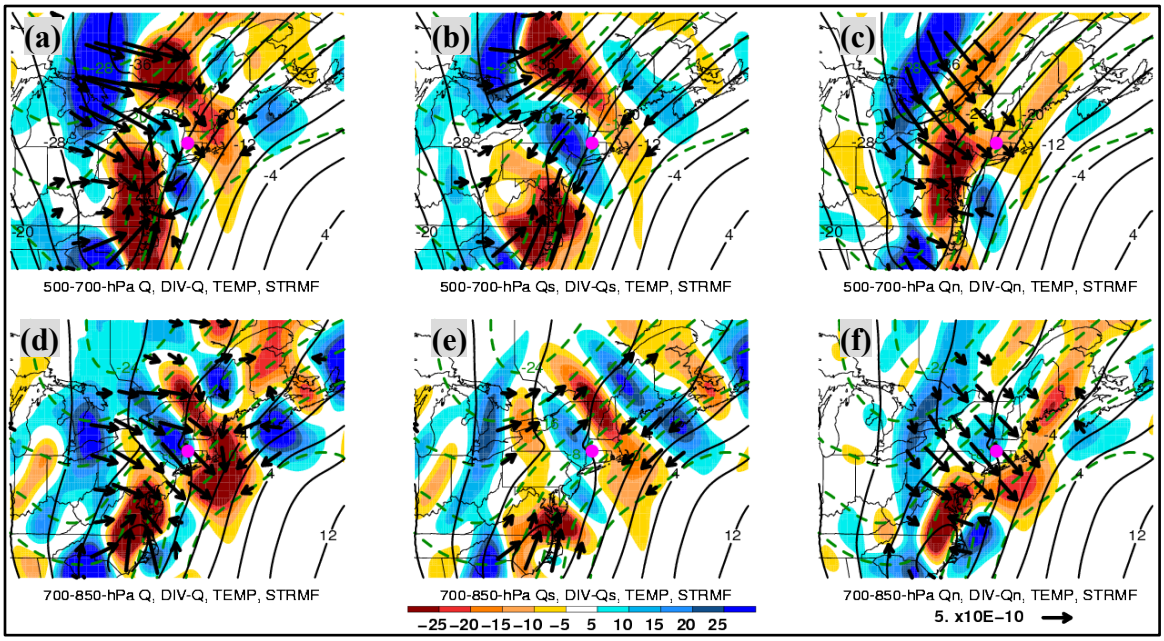

Fig. 3.37. As in Fig. 3.6, except at 0600 UTC 2 Mar 2009. Q vectors with magnitudes $\geq 2 \times 10^{-10}$ K m^{-1} s^{-1} are plotted. In all panels, the heavy pink dot marks the centroid of the laterally quasi-stationary snowband.

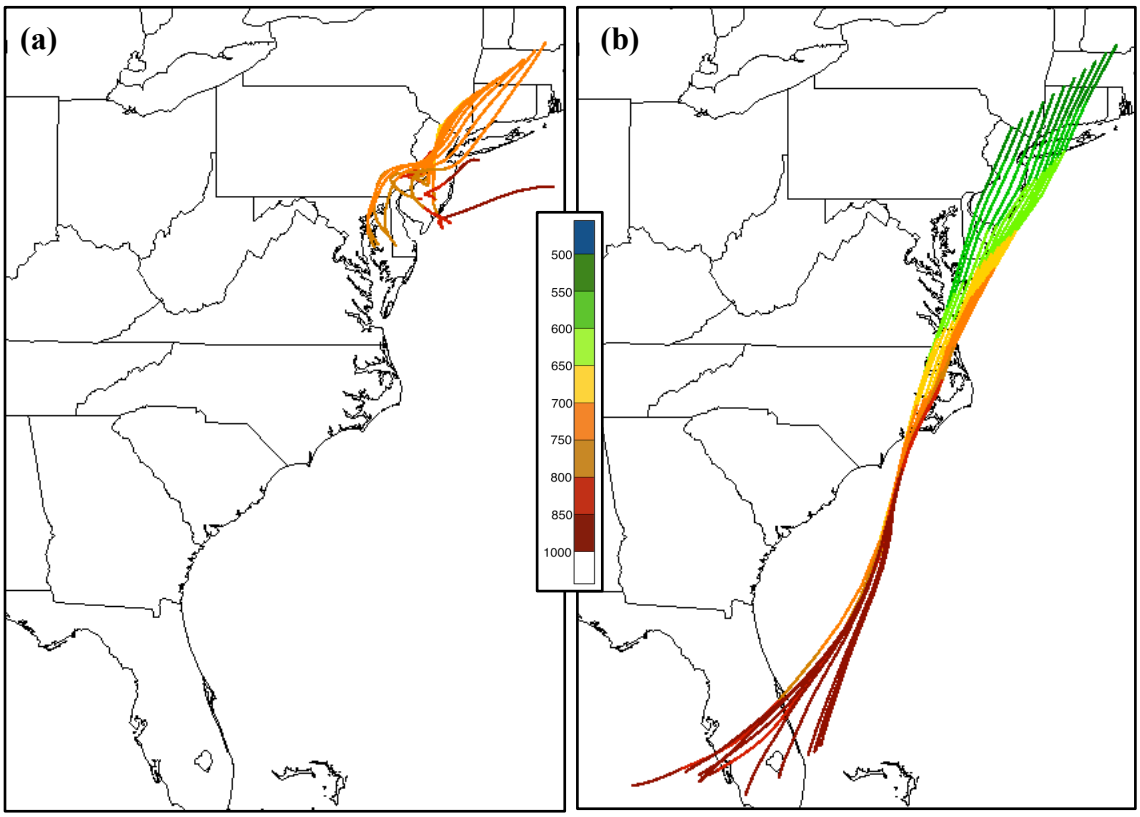

Fig. 3.38. As in Fig. 3.8, except for parcels arriving along the laterally quasi-stationary snowband at 0600 UTC 2 Mar 2009.

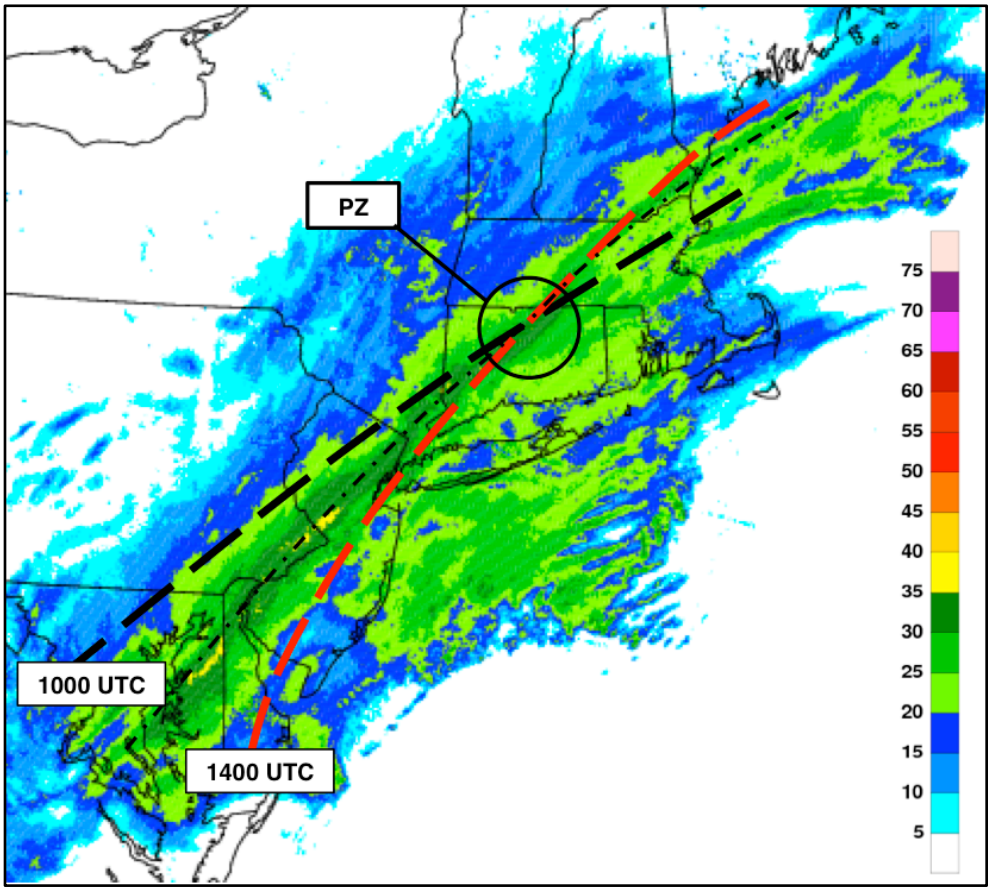

Fig. 3.39. Radar reflectivity (dB*Z*) at 1200 UTC 12 Feb 2006. Dash–dot pattern denotes the axis of the pivoting snowband discussed in the text. The axis of the same snowband 2 h before (2 h after) the mosaic time is shown in dashed black (dashed red), as labeled. The pivot zone (labeled "PZ") at 1200 UTC is encircled in black.

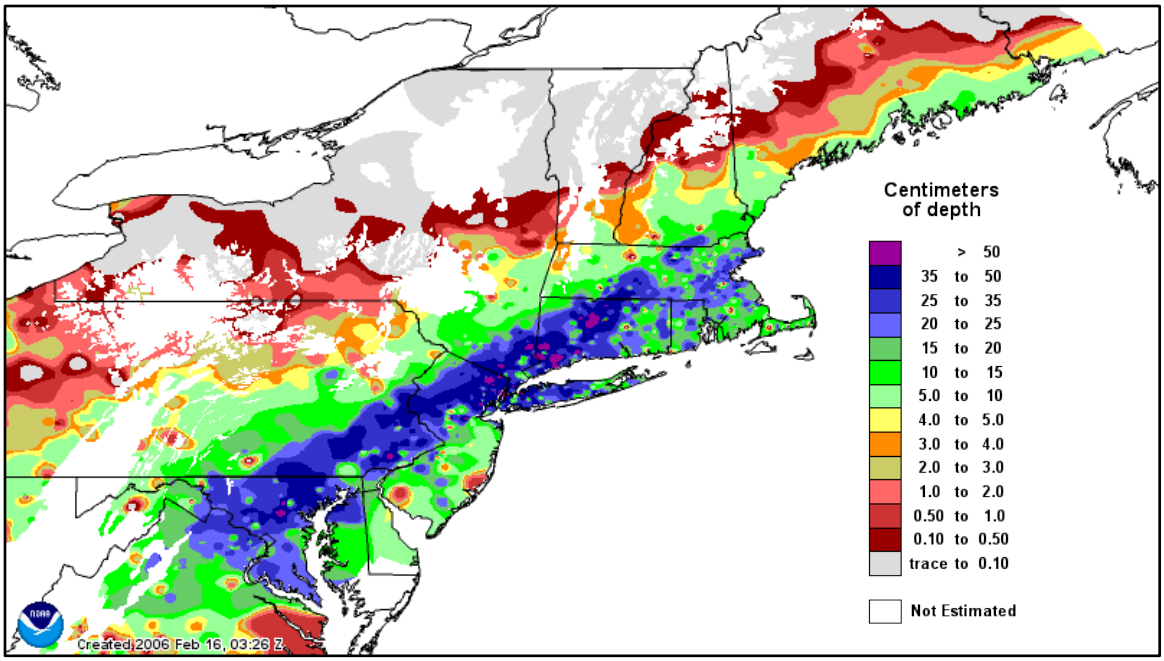

Fig. 3.40. 24-h snowfall accumulation (cm) ending at 1800 UTC 12 Feb 2006.

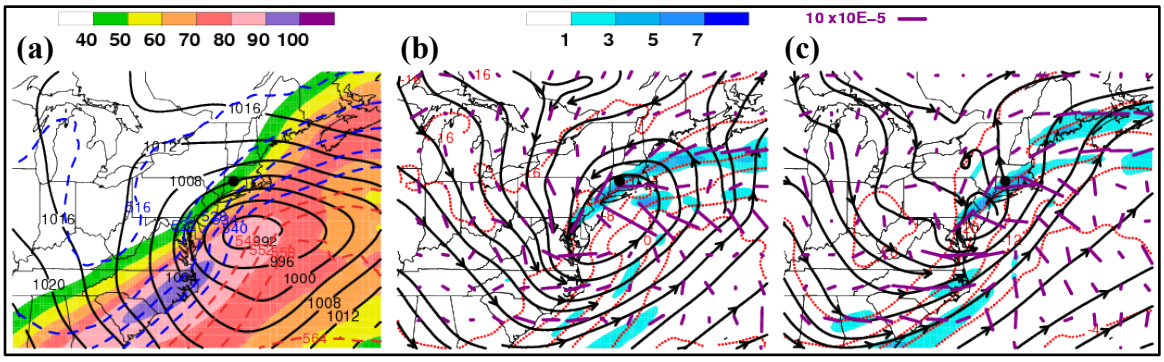

Fig. 3.41. As in Fig. 3.2, except at 1200 UTC 12 Feb 2006. The reference axis of dilatation (top right) represents resultant deformation of $10 \times 10^{-5}\,s^{-1}$. In all panels, the heavy black dot marks the pivot zone of the pivoting snowband.

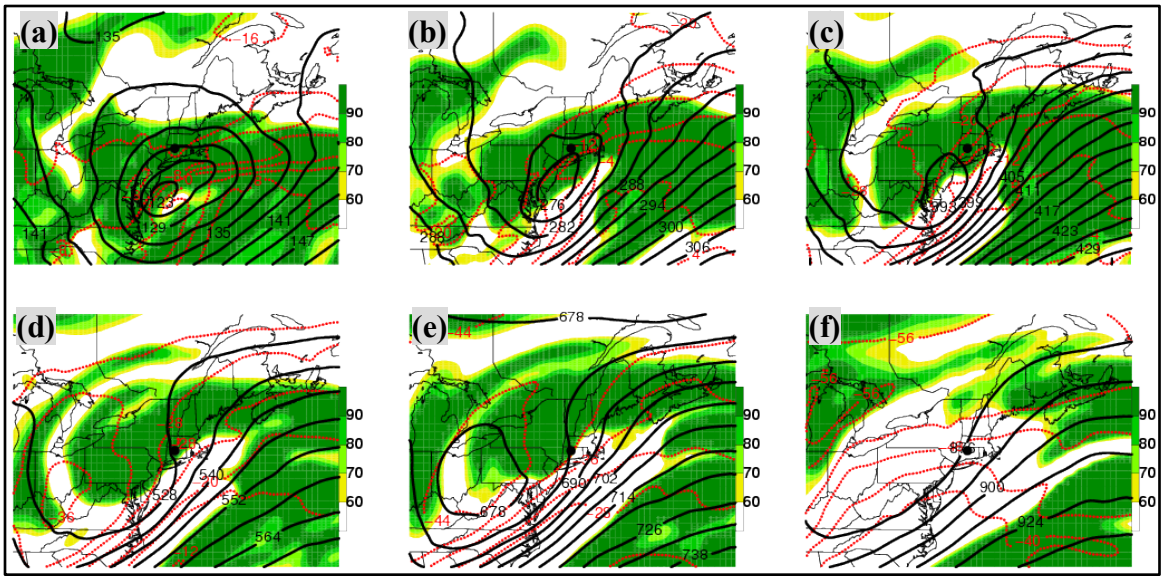

Fig. 3.42. As in Fig. 3.3, except at 1200 UTC 12 Feb 2006. In all panels, the heavy black dot marks the pivot zone of the pivoting snowband.

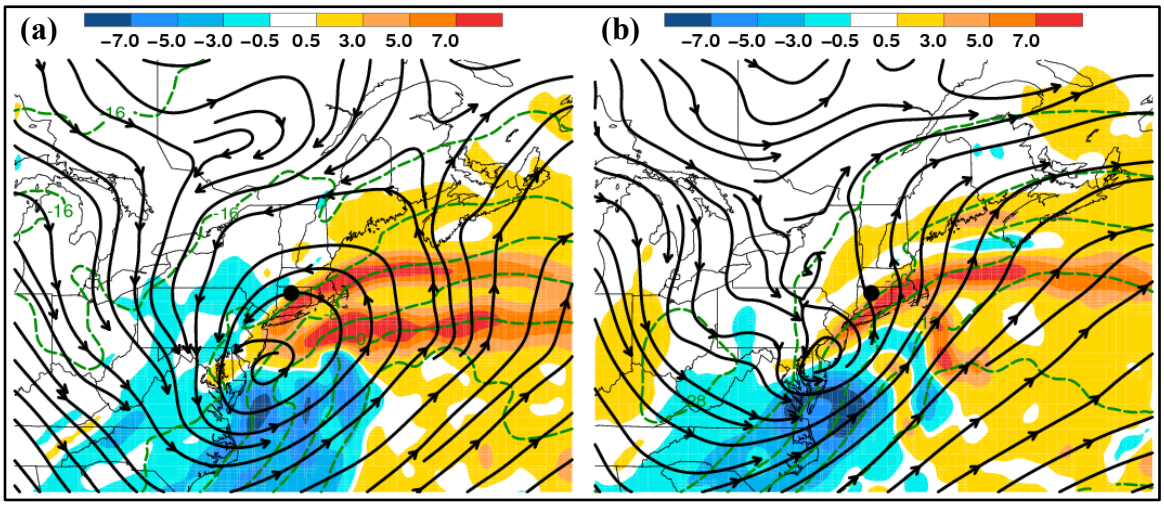

Fig. 3.43. As in Fig. 3.4, except at 1200 UTC 12 Feb 2006. In both panels, the heavy black dot marks the pivot zone of the pivoting snowband.

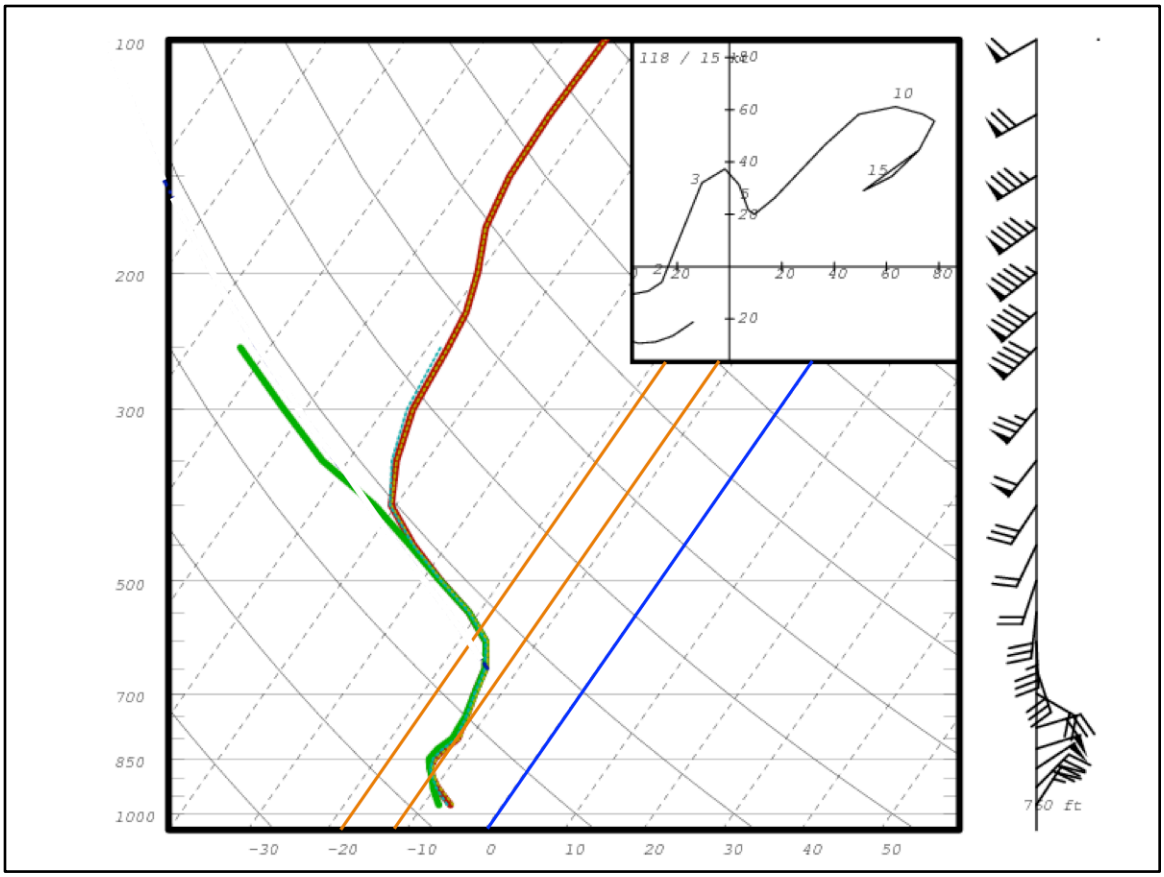

Fig. 3.44. As in Fig. 3.5, except at the pivot zone of the pivoting snowband at 1200 UTC 12 Feb 2006. Pivot zone location is shown by black dots in Figs. 3.41–3.43.

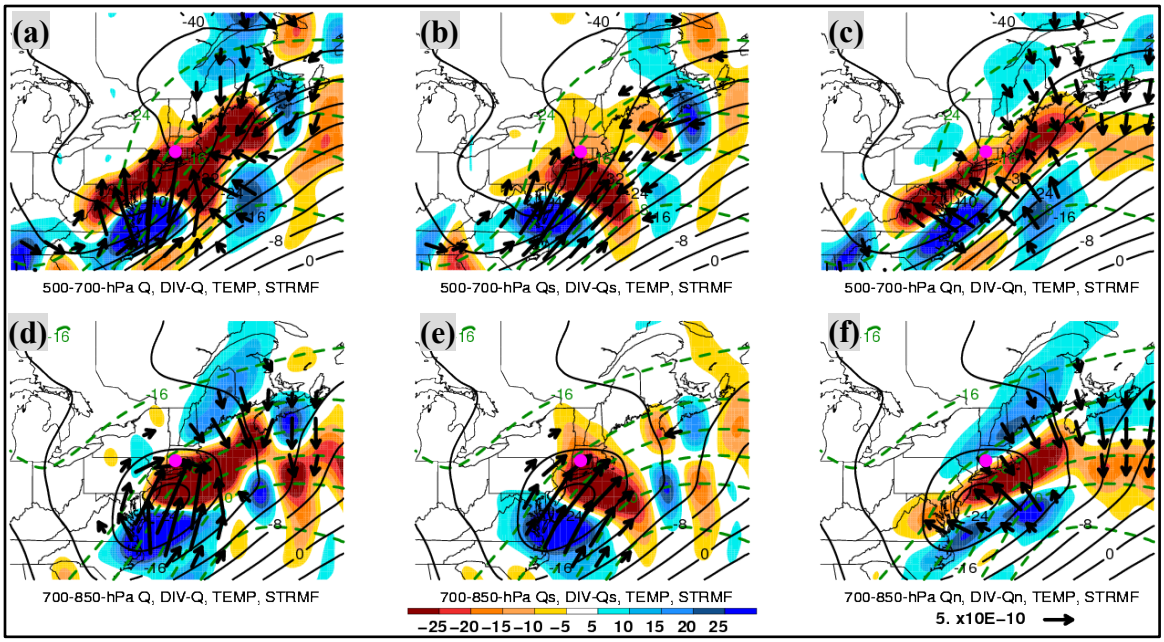

Fig. 3.45. As in Fig. 3.6, except at 1200 UTC 12 Feb 2006. *Q* vectors with magnitudes ≥ 2×10^{-10} K m^{-1} s^{-1} are plotted. In all panels, the heavy pink dot marks the pivot zone of the pivoting snowband.

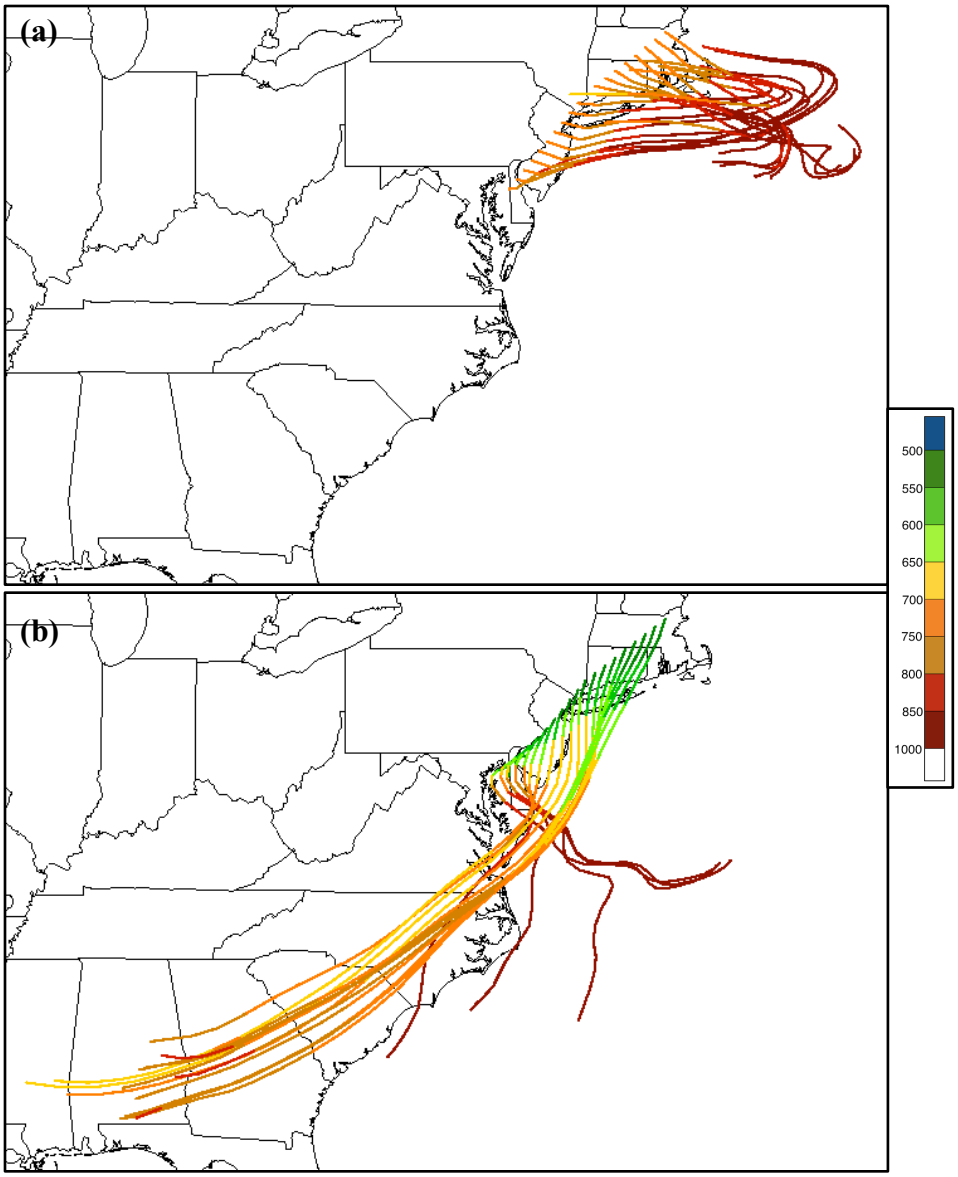

Fig. 3.46. As in Fig. 3.8, except for parcels arriving along the pivoting snowband at 1200 UTC 12 Feb 2006.

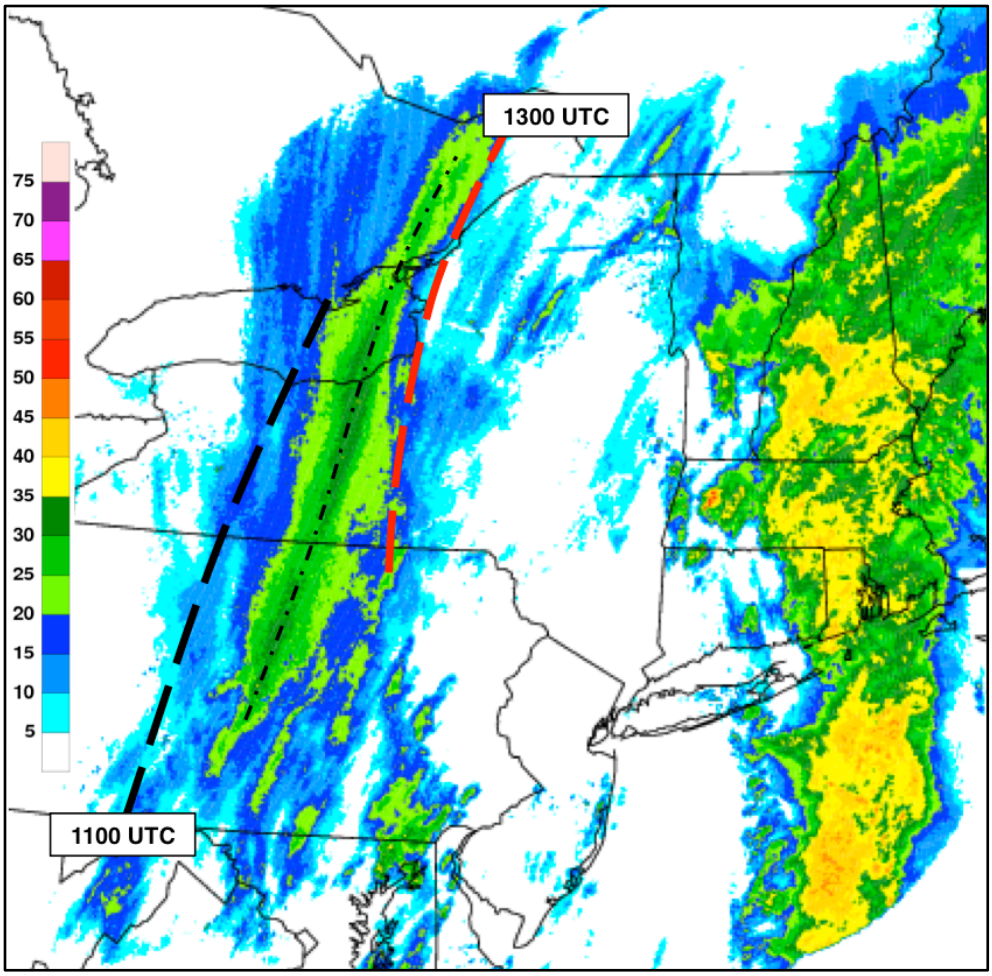

Fig. 3.47. Radar reflectivity (dB*Z*) at 1200 UTC 12 Dec 2008. Dash–dot pattern denotes the axis of the hybrid snowband discussed in the text. The axis of the same snowband 1 h before (1 h after) the mosaic time is shown in dashed black (dashed red), as labeled.

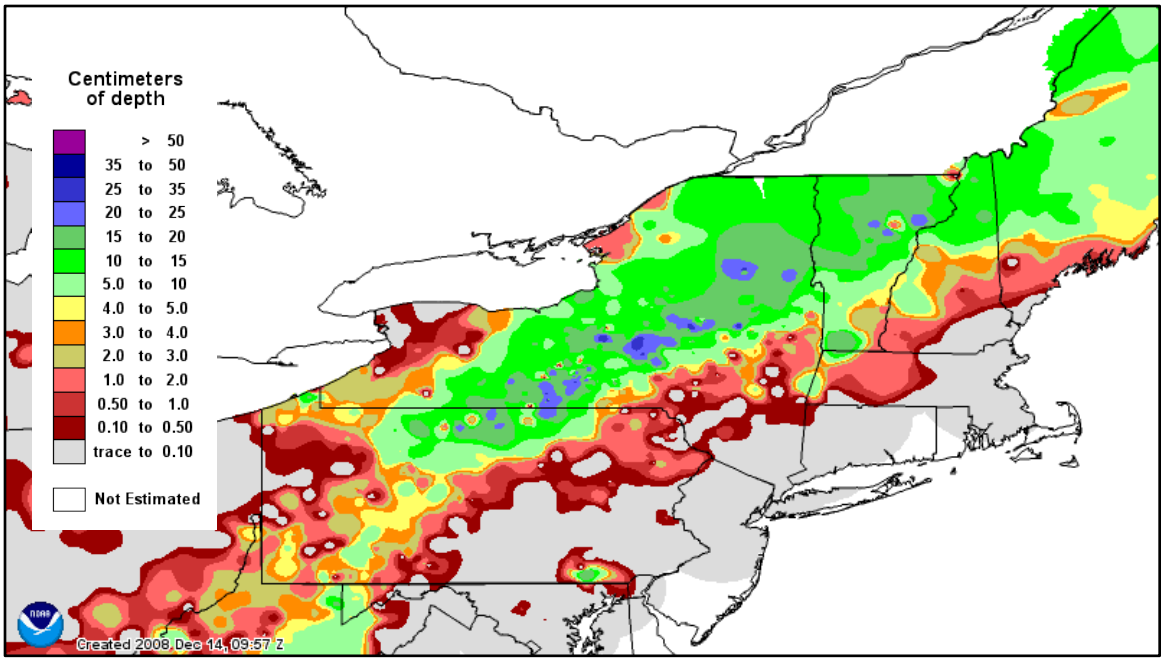

Fig. 3.48. 24-h snowfall accumulation (cm) ending at 1800 UTC 12 Dec 2008.

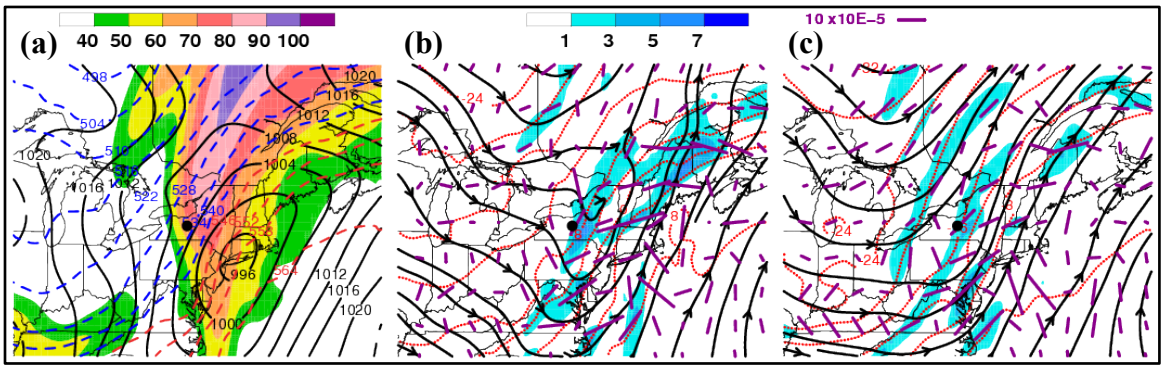

Fig. 3.49. As in Fig. 3.2, except at 1200 UTC 12 Dec 2008. The reference axis of dilatation (top right) represents resultant deformation of $10 \times 10^{-5}\ s^{-1}$. In all panels, the heavy black dot marks the centroid of the hybrid snowband.

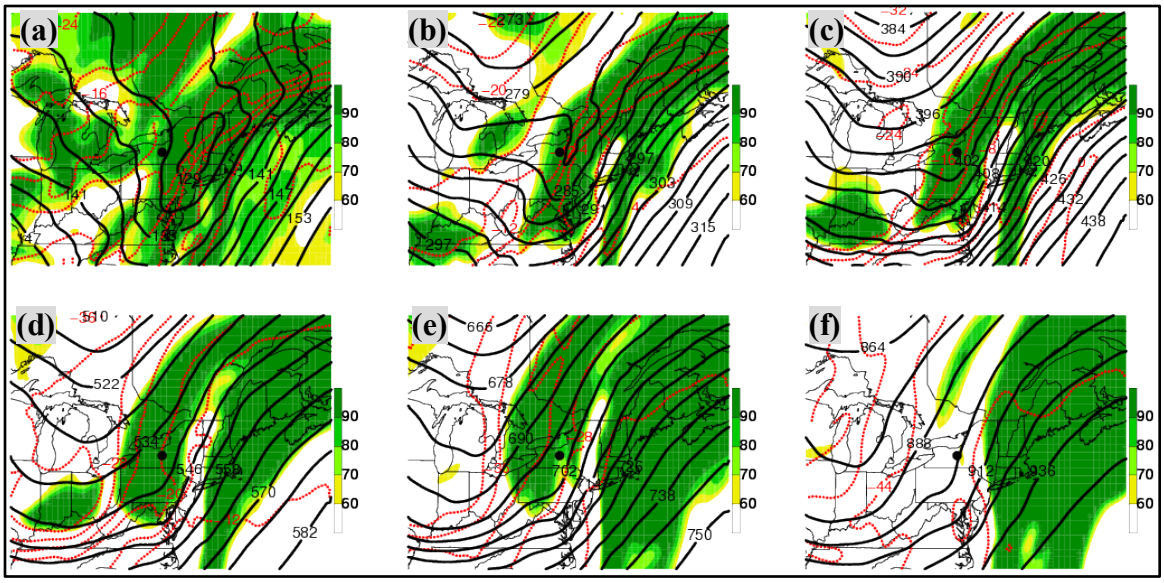

Fig. 3.50. As in Fig. 3.3, except at 1200 UTC 12 Dec 2008. In all panels, the heavy black dot marks the centroid of the hybrid snowband.

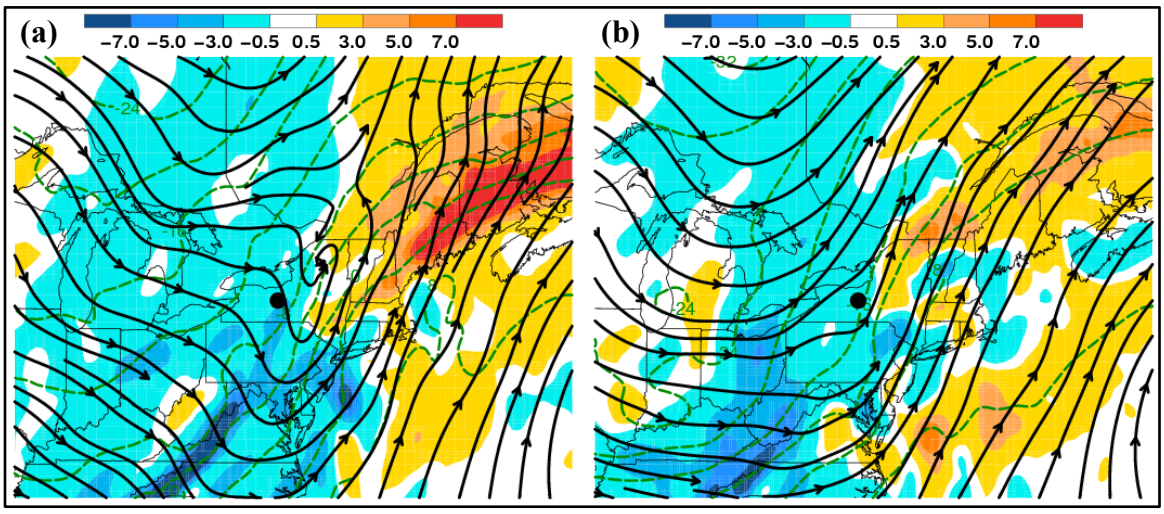

Fig. 3.51. As in Fig. 3.4, except at 1200 UTC 12 Dec 2008. In both panels, the heavy black dot marks the centroid of the hybrid snowband.

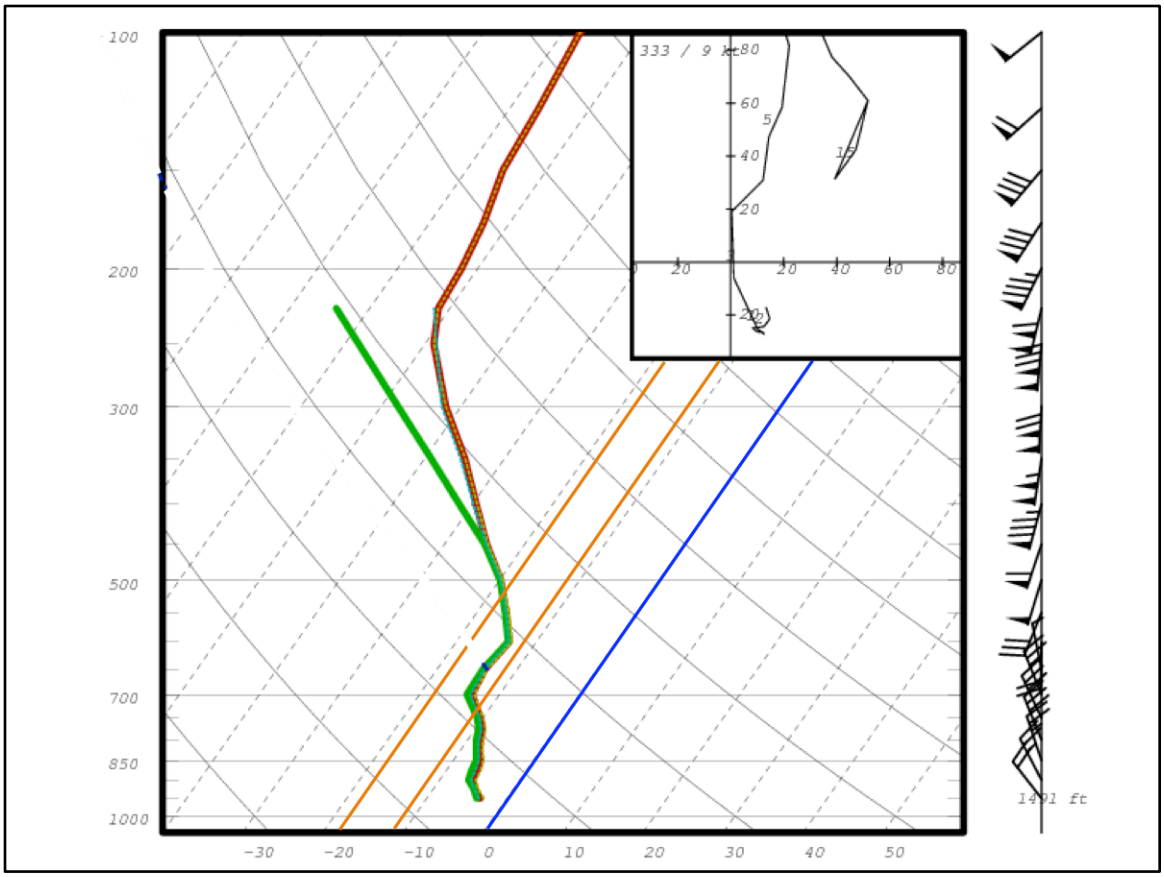

Fig. 3.52. As in Fig. 3.5, except at the centroid of the hybrid snowband at 1200 UTC 12 Dec 2008. Centroid location is shown by black dots in Figs. 3.49–3.51.

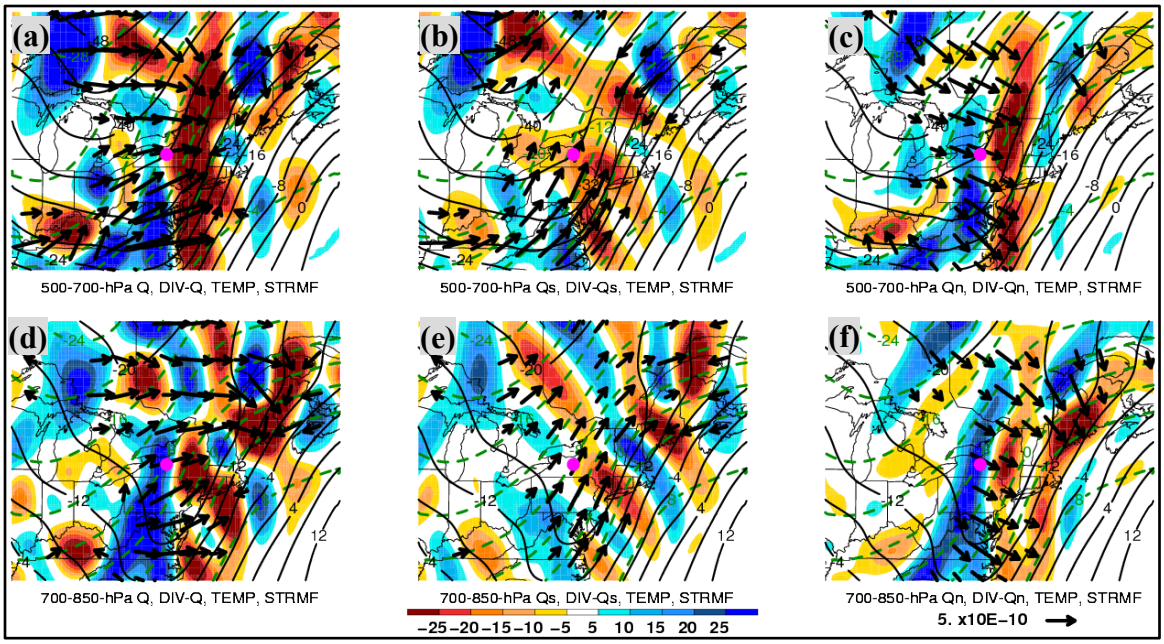

Fig. 3.53. As in Fig. 3.6, except at 1200 UTC 12 Dec 2008. *Q* vectors with magnitudes $\geq 2 \times 10^{-10}$ K m^{-1} s^{-1} are plotted. In all panels, the heavy pink dot marks the centroid of the hybrid snowband.

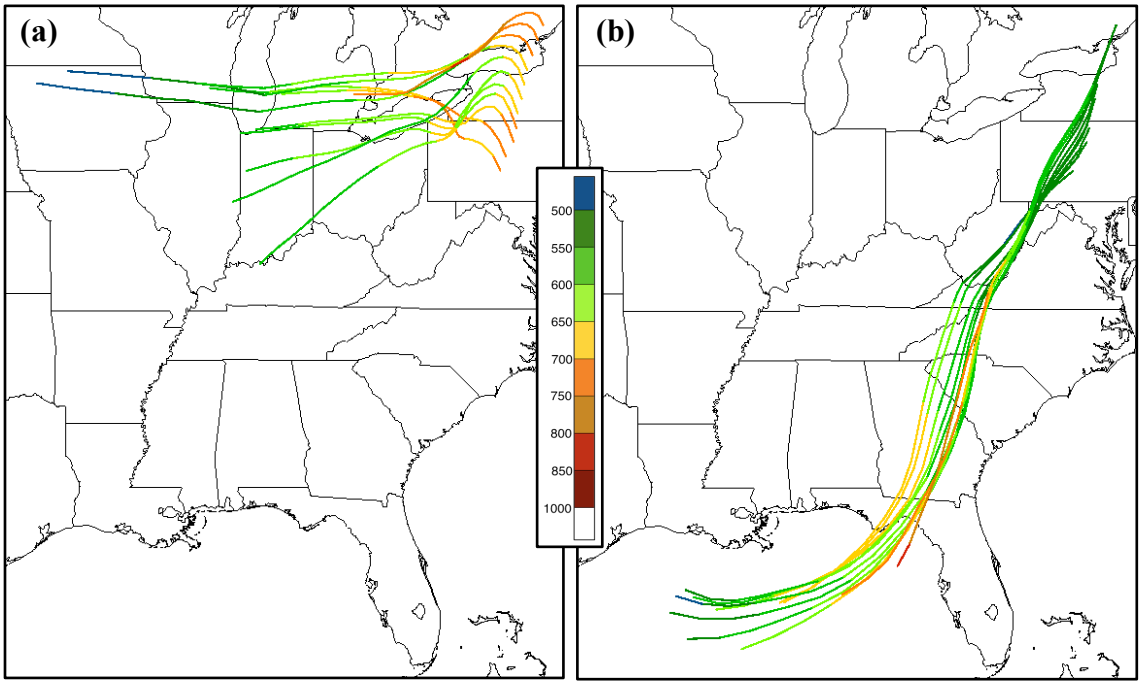

Fig. 3.54. As in Fig. 3.8, except for parcels arriving along the hybrid snowband at 1200 UTC 12 Dec 2008.

4. Discussion, Conclusions, and Suggestions for Future Work

4.1 Discussion

4.1.1 Composite Analysis

The composite results of the present study are complementary in several respects to those of Novak (2002). In classifying mesoscale precipitation bands in the northeast U.S., Novak (2002) included a "northwest" class that encompassed so-called "single bands" located in the northwest quadrant of surface cyclones. The pivoting category composite of the present study, like the northwest class composite of Novak (2002) (not shown), describes a band oriented southwest–northeast and situated (1) in a region of midlevel frontogenesis northwest of a surface cyclone (Figs. 3.16a,c), (2) west of an upper-level jet axis (Fig. 3.16a) and low-level warm advection maximum (Fig. 3.18a), and (3) east of a negatively tilted midlevel trough axis (Fig. 3.18b). As noted in section 1.2.4, Novak (2002) observed that 62% of northwest class bands exhibited distinct "pivot point" in radar observations. This observation, given the composite similarities noted above, suggests that pivoting snowbands and northwest class bands are complementary descriptions of similar phenomena in northeast U.S. winter storms. Moreover, 15 of the 18 events (83%) in the pivoting category composite occurred near a PV hook structure at 300 or 400 hPa. As noted in section 1.1.2, Martin (1998a) suggests that an upper-level PV hook is a manifestation of an underlying warm occlusion and trowal. Thus, although trowals were not directly identified in this study, the common presence of upper-level PV hooks near pivoting snowbands suggests that these bands frequently occurred in conjunction with trowals. This inference is consistent with Novak et al. (2010), who

found that 61% of snowbands in the comma-head region of northeast U.S. cyclones occurred near upper-level PV hook structures, and who included a trowal in their conceptual model of these band environments (see Fig. 1.6).

Analogous to northwest class bands, Novak (2002) included an "east" class that encompassed single bands in the eastern quadrant of surface cyclones. The laterally translating category composite of the present study is similar to the east class composite of Novak (2002) (not shown) in describing a band oriented west-northwest–east-southeast and located (1) in a region of midlevel frontogenesis and diffluence beneath the equatorward entrance region of an upper-level jet (Figs. 3.2a,c), (2) east of a low-level cyclone (Figs. 3.2a,b), and (3) north of a low-level warm advection maximum (Fig. 3.4a). Novak (2002) noted that 80% of east class bands moved northeastward (i.e., in the cross-axis direction), suggesting that laterally translating snowbands and east class bands are complementary descriptions of similar phenomena.

The laterally quasi-stationary category composite of the present study exhibits similarities to the "nonbanded" composite of Novak (2002) (not shown). In both composites, midlevel frontogenesis is situated in confluent flow east of a short-wave trough axis and beneath the equatorward entrance region of a southwest–northeast-oriented upper-level jet (Figs. 3.9a,c). However, compared to the Novak (2002) nonbanded composite, the laterally quasi-stationary category composite exhibits a more amplified short-wave trough. Although frontogenesis was present in the nonbanded composite, Novak (2002) noted that this frontogenesis was weaker, more gently sloped in the vertical, and embedded in greater conditional stability than in banded event composites. The similarities between the nonbanded composite of Novak (2002) and the

laterally quasi-stationary category composite of the present study suggests a potential forecasting challenge. Namely, in situations where frontogenesis is expected in advance of confluent midlevel short-wave troughs, snowband development may be uncertain, but if band development occurs, a distinct snowfall accumulation gradient may result.

Although along-band variations in DGZ depth were not documented, composite thermodynamic profiles (Figs. 3.5, 3.12, and 3.19) provide evidence that pivoting snowbands may generally be associated with deeper DGZs, and possibly heavier snowfall rates, than laterally translating and laterally quasi-stationary snowbands.

4.1.2 Case Studies

Diagnostic fields associated with the laterally translating snowband of 9 December 2009 closely resembled those of the laterally translating category composite. For instance, the laterally translating snowband was situated east of a surface cyclone and near the equatorward entrance region of an upper-level jet streak (Fig. 3.25a), similar to the composite (Figs 3.2a). Low-to-midlevel diffluence was associated with deformation and frontogenesis near the band (Figs. 3.25b,c), although frontogenesis was less coherent in the vertical between the 850–700-hPa and 700–500-hPa layers than in the composite (Figs. 3.2b,c). Similar to the composite (Figs. 3.4a,b), low-to-midlevel warm advection was present along the band (Figs. 3.27b,c) and the maximum warm advection in the 850–700-hPa layer was located on the warm side of the band (Fig. 3.27a). At the band centroid, winds veered with height and the hodograph exhibited low-level clockwise curvature (Fig. 3.28, inset) resembling the composite (Fig 3.5, inset). Along most of the

band axis, the collocation of Q_s-vector convergence (Figs. 3.29b,e) with frontogenetical Q_n vectors (Figs. 3.29c,f) was also apparent in the composite (Figs. 3.6b,c,e,f). Moreover, similar to the composite (Figs. 3.8a,b), time-integrated diffluence was implied by the parcel clusters that arrived along the snowband at 700 and 500 hPa (Figs. 3.30a,b).

Numerous aspects of the laterally quasi-stationary snowband event of 2 March 2009 resembled the corresponding composite. For example, similar to the composite (Fig. 3.9a), the snowband was located north of a surface cyclone and in the equatorward entrance region of an upper-level jet streak (Fig. 3.33a). Frontogenesis was present near the band in the 700–500-hPa layer amid confluent southwesterly flow (Fig. 3.33c) that resembled the composite (Fig. 3.9c). Further, weak/neutral low-to-midlevel temperature advection along the band axis (Fig. 3.35a,b) was associated with an approximately straight and radially oriented hodograph at the band centroid (Fig. 3.36, inset), as in the composite (Figs. 3.11a,b and 3.12, inset). Lastly, the along-trajectory elongation of the parcel cluster that arrived along the band at 500 hPa implied time-integrated confluence (Fig. 3.38b), similar to the composite (Fig. 3.15b).

Some differences between the laterally quasi-stationary snowband case study and category composite are notable. First, the snowband in the 2 March 2009 case study was situated near an 850–700-hPa layer-mean col (Fig. 3.35a), whereas the inferred composite band is situated in confluent southwesterly flow (Fig. 3.11a). This difference may be reconciled by noting that the *confluent asymptote* that intercepted the col in the 2 March 2009 case was aligned southwest–northeast, approximately parallel to the snowband (Fig. 3.35a). Thus, the laterally quasi-stationary band in the case study, like the composite, was characterized by weak cross-band flow in the 850–700-hPa layer.

Second, the fields of total Q-vector divergence near the 2 March 2009 laterally quasi-stationary snowband (Figs. 3.37a,d) were less coherent than in the corresponding composite (Figs. 3.13a,d). However, in both the case study (Figs. 3.37b,c,e,f) and composite (Figs. 3.13b,c,ef), Q_s vectors were generally small along the band axis, and band-parallel regions of Q_n-vector convergence were present.

Diagnostic fields associated with the pivoting snowband of 12 February 2006 exhibited a close correspondence with those in the pivoting category composite. Similar to the composite (Fig. 3.16a), the pivot zone was located in the northwestern quadrant of a surface cyclone and west of the axis of an upper-level jet (Fig. 3.41a). In the 850–700-hPa layer, a closed cyclonic circulation was centered ~350 km south-southwest of the pivot zone (Fig. 3.41b), and a negatively tilted 700–500-hPa short-wave trough axis was located west of the pivot zone (Fig. 3.41c), both of which are present in the composite (Figs. 3.16b,c). A dipole of low-to-midlevel warm–cold advection, oriented in the along-isotherm direction, was present near the snowband (Figs. 3.43a,b), and the pivot zone was west of a warm advection maximum, similar to the composite (Figs. 3.18a,b). In both the case study (Fig. 3.44) and composite (Fig. 3.19), veering winds with height were found at the pivot zone, consistent with warm advection at this location. In the case study (Figs. 3.45b,e), downshear-directed Q_s vectors were present along much of the band, and the largest Q_s vectors were found upshear of the pivot zone, as in the composite (Figs. 3.20b,e). Additionally, Q_n vectors in the case study (Figs. 3.45c,f), like the composite (Figs. 3.20c,f), were generally frontolytical (frontogenetical) in the region upshear (downshear) of the pivot zone and contributed to a region of Q_n-vector convergence near

the band. Lastly, similar to the composite (Fig. 3.22a), time-integrated diffluence was implied by the parcel cluster arriving at 700 hPa (Fig. 3.46a).

Although hybrid snowband category composites were not calculated, diagnostic fields associated with the hybrid snowband event of 12 December 2008 can be compared with those associated with the laterally translating, laterally quasi-stationary, and pivoting band events. Collectively, the diagnostic fields of the hybrid snowband event did not resemble those of the other events. For instance, the position of the hybrid snowband in the northwestern quadrant of a surface cyclone (Fig. 3.49a) resembled that of the pivoting snowband (Fig. 3.41a). However, the jet-relative position of the hybrid band in the entrance region of a southwest–northeast upper-level jet (Fig. 3.49a) was similar to that of the laterally quasi-stationary band (Fig. 3.33a). Downshear-directed Q_s vectors along the hybrid band (Figs. 3.53b,e) resembled those along the pivoting snowband (Figs. 3.45b,e). However, Q_n vectors along the hybrid band were frontogenetical (Figs. 3.53c,f), whereas Q_n vectors along the pivoting snowband were frontolytical (frontogenetical) near its upshear (downshear) flank. These results suggest that band-relative patterns in a *single* diagnostic field may be associated with multiple modes of band motion. Therefore, band motion should be anticipated by considering multiple diagnostic fields (as have been described).

4.1.3 Diagnostic Methods

A variety of diagnostic fields have been discussed in relation to mesoscale snowbands and their motion characteristics. Among these diagnostics, vertical wind

shear profiles (i.e., hodographs) and partitioned Q_s and Q_n vectors are not customarily employed in assessing mesoscale snowband environments. For this reason, the application of these diagnostics in this work warrants brief discussion.

Hodograph evaluation appears to provide some utility in identifying environments favoring laterally quasi-stationary snowbands. As noted in section 1.2.4, Banacos (2003) observed that environments near stationary mesoscale precipitation bands are often characterized by straight, radially oriented hodographs that intercept the origin (e.g., the hodographs labeled "Nc" and "Nf" in Fig. 1.8). Note that the hodograph at the composite laterally quasi-stationary band centroid (Fig. 3.12, inset) is consistent with the Banacos (2003) hodograph description for environments near stationary bands. However, hodographs at the centroids of some composite-member bands did not pass within 5 m s^{-1} of the origin. Therefore, it is appropriate to describe the typical hodograph at laterally quasi-stationary snowband centroids as approximately straight and radially oriented, *with or without* an approximate origin intercept.

Composites of rotational frontogenesis in the nondivergent framework (i.e., Q_s vectors) appear consistent with observed snowband motion characteristics. Given that mesoscale bands are typically oriented approximately parallel to midlevel isentropes (see section 1.2.2), the nonrotating, axis-parallel motion of laterally quasi-stationary snowbands is consistent with weak rotational frontogenesis along their axes (Figs. 3.13b,e), and Q_s vectors smaller than 3×10^{-10} K m^{-1} s^{-1} in the 850–700-hPa and 700–500-hPa layers were generally present along the member bands in the laterally quasi-stationary category composite. In contrast, the pronounced counterclockwise rotation of pivoting snowbands necessitates counterclockwise rotational frontogenesis (Figs.

3.20b,e), and large Q_s vectors (~10×10^{-10} K m^{-1} s^{-1}) in the 850–700-hPa and 700–500-hPa layers were generally present at the upshear flanks of composite-member pivoting snowbands. However, as noted in section 3.2.3, the composite pivot zone does not coincide with either the largest downshear-directed Q_s vectors or a maximum of normalized Q_s. Also note that QG forcing for ascent from both Q_n- and Q_s-vector convergence is present at the band centroid in the laterally translating category composite (Figs. 3.6b,e) and at the pivot zone in the pivoting category composite (Figs. 3.20b,e), suggesting that mesoscale bands forced by frontogenesis are observed even when collocated with Q_s-vector convergence.

Whereas Q_n vectors in the laterally translating and laterally quasi-stationary category composites are frontogenetical along the inferred bands (Figs. 3.6c,f and 3.13c,f), Q_n vectors are generally frontolytical (frontogenetical) in the region upshear (downshear) of the composite pivot zone (Figs. 3.20c,f). Inspection of pivoting events indicates that 16 of the 18 (89%) member bands in the pivoting category composite were associated with frontolytical Q_n vectors at or near the upshear band flank in the 850–700-hPa and/or 700–500-hPa layers. The possible role of this along-band Q_n-vector reversal in contributing to the formation and/or maintenance of a pivot zone is not certain, but this diagnostic signature may be useful in anticipating pivoting snowbands.

4.1.4 Applications of Research to Operational Forecasting

The case studies presented in section 3.3 provide evidence that snowband motion characteristics may influence the geographic distribution of snowfall accumulation.

Therefore, as discussed in section 1.1, forecaster anticipation and recognition of band motion characteristics may help to inform warning decisions.

The identification of low-to-midlevel frontogenesis collocated with moisture and weak moist symmetric stability will often aid in determining a region and timeframe in which mesoscale snowbands are most likely to develop (Novak et al. 2006). Anticipating the surface position of a snowband with respect to a frontogenesis region is not always straightforward, as frontogenesis is often vertically sloped, and the horizontal scale of the ensuing transverse ageostrophic circulation is modulated by the moist symmetric stability. However, even if band location is uncertain, snowband motion can be anticipated by considering certain environmental attributes near a frontogenesis region.

Conceptual models for laterally translating, laterally quasi-stationary, and pivoting snowbands are shown in Figs. 4.1a–c. By summarizing the common environmental attributes associated with these band types, the conceptual models provide a basis for "pattern recognition" prior to band occurrence. A conceptual model for hybrid snowbands is not presented, since hybrid band motion was observed in varied synoptic-scale patterns.

Laterally quasi-stationary and pivoting snowbands may produce sharp snowfall accumulation gradients in the across-band direction. For this reason, if these band motion characteristics are expected, band placement uncertainty in the across-isotherm direction may contribute to large errors in forecasts of snowfall accumulation.

4.2 Conclusions

This research investigated environmental attributes associated with particular modes of snowband motion that are observed in northeast U.S. winter storms. Using radar reflectivity data, snowband events during a 6-yr period were subjectively identified and categorized according to a band motion classification scheme, wherein bands were classified as laterally translating, laterally quasi-stationary, pivoting, or hybrid. Composite analysis was utilized to ascertain the environmental attributes associated with laterally translating, laterally quasi-stationary, and pivoting bands. Case studies were performed for all four modes of band motion.

Laterally translating snowbands are characterized by predominant cross-axis motion. Composite analysis indicates that these bands are typically observed in the eastern quadrant of surface cyclones and near the equatorward entrance regions of upper-level jet streaks. Low-to-midlevel diffluent frontogenetical flow and warm advection are typically present along the band axis, and a low-level warm advection maximum is often located on the warm side of the band. Additionally, low-to-midlevel Q_s-vector convergence is usually collocated with frontogenetical Q_n vectors along most of the band. Owing to their progressive cross-axis motion, laterally translating snowbands do not favor distinct snowfall accumulation gradients along their paths.

Laterally quasi-stationary snowbands exhibit near-zero cross-axis motion, and for this reason, may yield pronounced snowfall accumulation gradients. Composite analysis reveals that these bands are typically situated in the northern quadrant of surface cyclones and in the equatorward entrance region of upper-level jet streaks with confluent midlevel frontogenetical flow. Weak/neutral low-to-midlevel temperature advection is often present along the band, and temperature advection may reverse sign across the band axis,

with warm (cold) advection generally on its warm (cold) side. Consistent with thermal wind considerations, the hodograph near the band centroid is often approximately straight and radially oriented. Along the band axis, low-to-midlevel Q_n vectors are frontogenetical and Q_s vectors are typically small.

Pivoting snowbands are characterized by pronounced counterclockwise rotation such that a segment of the band near the center of rotation (the *pivot zone*) exhibits near-zero cross-axis motion. Composite analysis indicates that pivoting snowbands are often located in the northwestern quadrant of surface cyclones, near the comma head–dry slot interface, and west of upper-level jet axes. A closed 850–700-hPa cyclonic circulation is often present immediately south of the pivot zone, and a negatively tilted 700–500-hPa trough axis is usually located west of the band. The pivot zone typically resides in a region of low-to-midlevel warm advection east of a warm advection maximum, and a dipole of warm–cold advection is often oriented in the along-isotherm direction. Low-to-midlevel Q_s vectors are downshear-directed and convergent along most of the band, with the largest Q_s vectors located upshear of the pivot zone. Q_n vectors are generally frontolytical (frontogenetical) in the region upshear (downshear) of the pivot zone and contribute to a coherent region of Q_n-vector convergence near the band. Heavy snowfall accumulation is favored near the pivot zone, where band residence time is prolonged, and a nearby snowfall accumulation gradient may result.

Hybrid snowbands exhibit predominant along-axis motion, but with a concurrent cross-axis component of motion. Hybrid snowband events were the most rarely observed and were found in varied synoptic-scale contexts, such that no composites were

calculated for this category. Owing to their progressive cross-axis motion, hybrid bands do not favor sharp gradients of snowfall accumulation.

4.3 Suggestions for Future Work

In this study, diagnostics of frontogenesis and rotational frontogenesis using Q_n and Q_s vectors, respectively, were motivated by the linkage of these vector fields to QG forcing for vertical motion. Additional insight into the formation and maintenance of pivot zones may be afforded by also considering diagnostics of frontogenesis and rotational frontogenesis that account for the total horizontal flow, the total three-dimensional flow, and/or diabatic heating and cooling.

Hydrometeor trajectories near snowbands that exhibit different motion characteristics may be insightful. Novak et al. (2008) noted that horizontal hydrometeor drift near snowbands can displace a radar reflectivity maximum horizontally by ~25 km between 3 km AGL and the surface. Additionally, Stark et al. (2013) observed variations in both ice crystal habit and snow–liquid density ratios near a pivoting snowband on 19–20 December 2009. Whether certain modes of band motion are associated with preferred ice crystal habits or snow–liquid density ratios is not known.

Quantifying numerical model QPF errors that are associated with different band motion characteristics may help to improve forecasts of heavy snowfall. Snowfall accumulation near laterally quasi-stationary and pivoting bands is hypothesized to be less predictable than near laterally translating bands, but additional investigation is needed to address this hypothesis. Lastly, although hodograph shapes associated with different

modes of band motion have been described, it is not known whether sharp and/or deep-layer hodograph curvature is detrimental to transverse ageostrophic circulations and band organization.

(a)

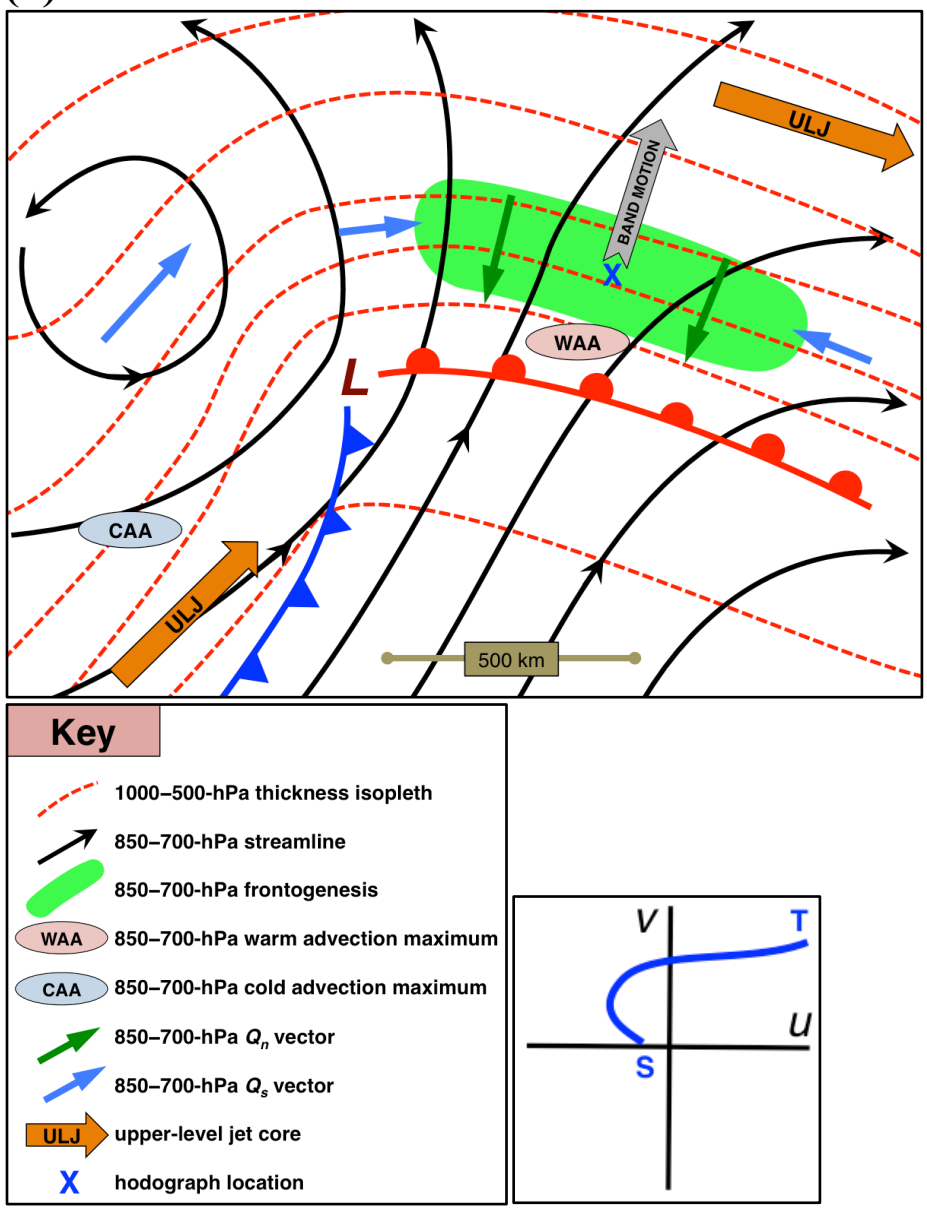
ULJ
BAND MOTION
X
WAA
L
CAA
ULJ
500 km
Key
1000–500-hPa thickness isopleth
850–700-hPa streamline
850–700-hPa frontogenesis
WAA
850–700-hPa warm advection maximum
CAA
850–700-hPa cold advection maximum
850–700-hPa Q_n vector
850–700-hPa Q_s vector
ULJ
upper-level jet core
X
hodograph location
V
T
U
S

(b)

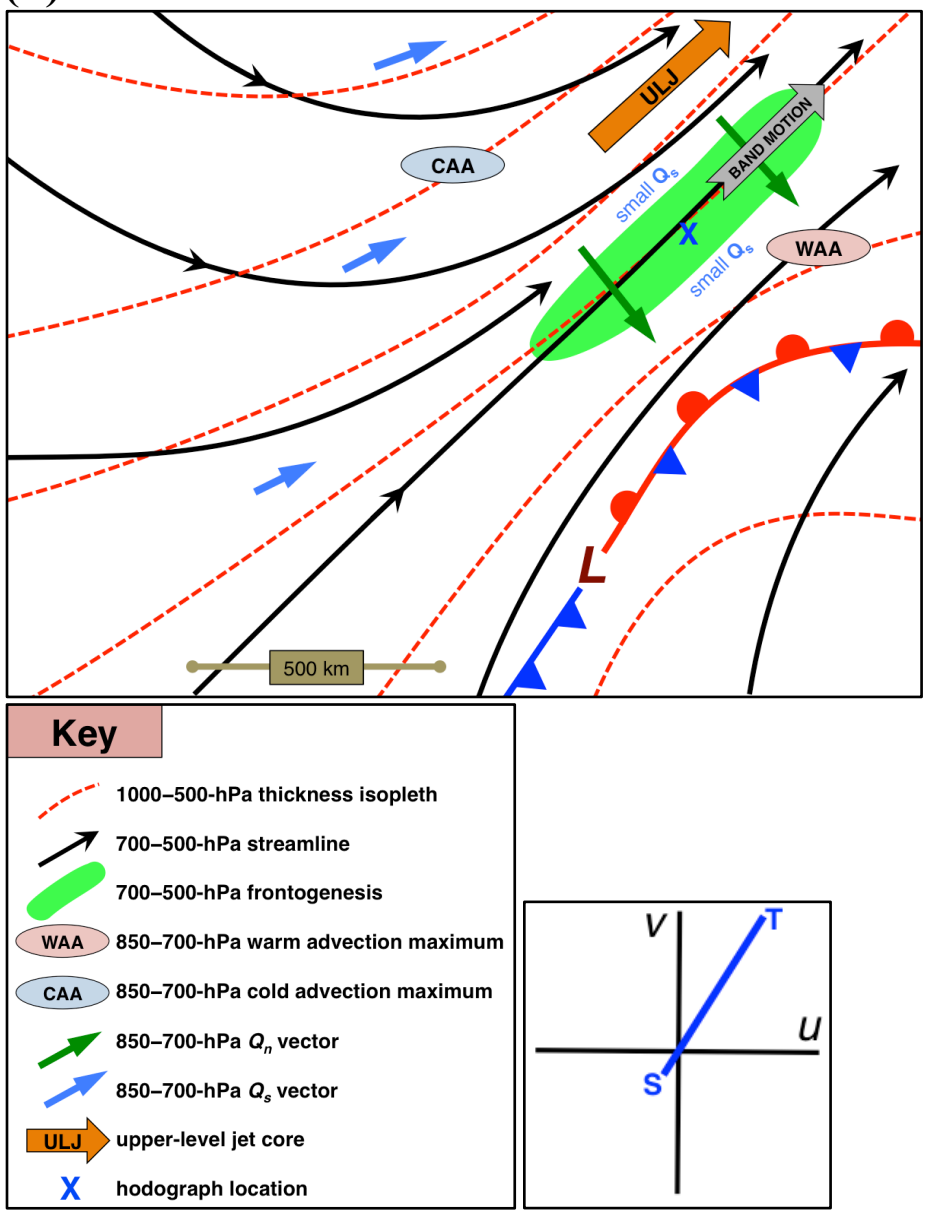
ULJ
BAND MOTION
CAA
small Q_s
X
small Q_s
WAA
L
500 km
Key
1000–500-hPa thickness isopleth
700–500-hPa streamline
700–500-hPa frontogenesis
WAA
850–700-hPa warm advection maximum
CAA
850–700-hPa cold advection maximum
850–700-hPa Q_n vector
850–700-hPa Q_s vector
ULJ
upper-level jet core
X
hodograph location
V
T
U
S

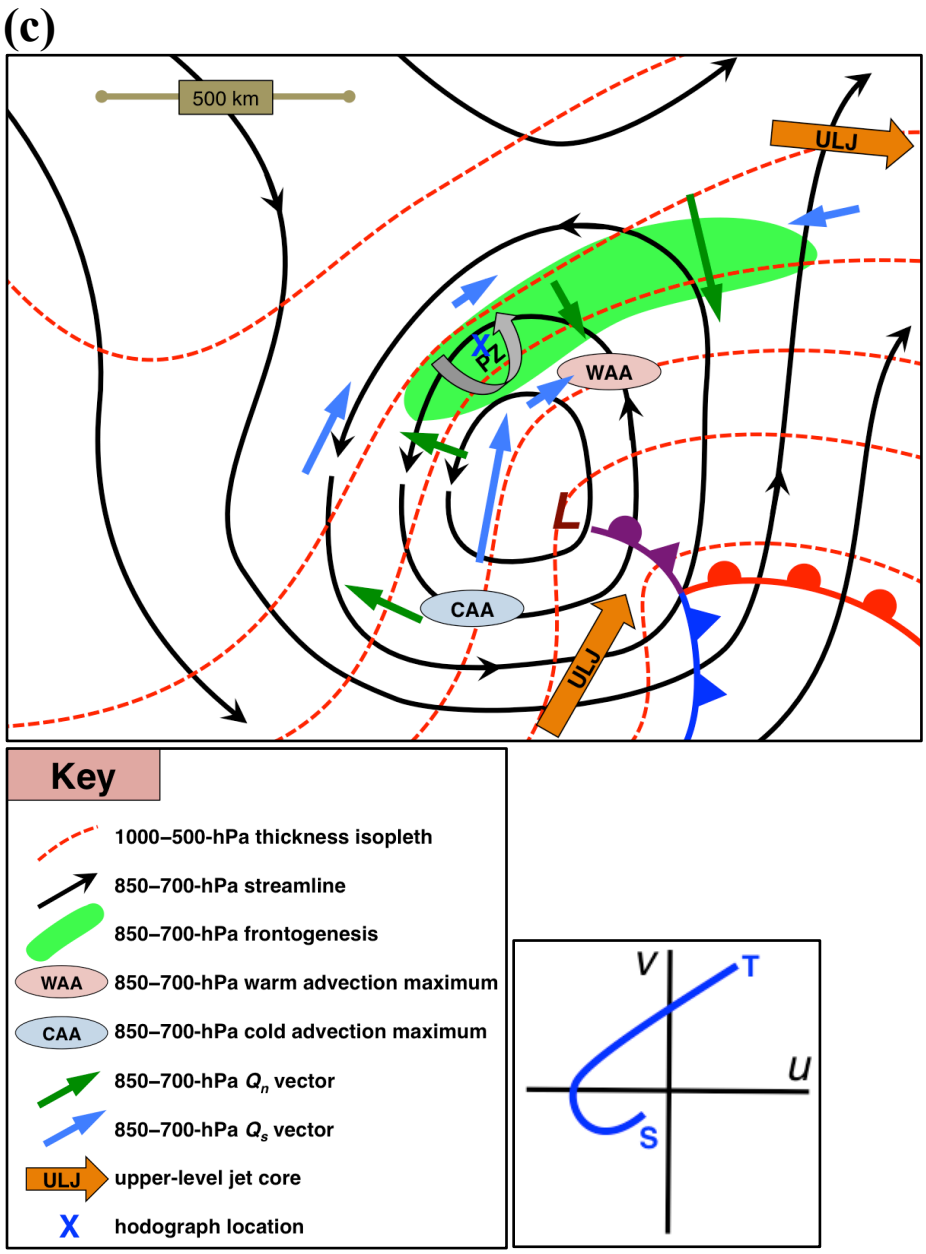

Fig. 4.1. Conceptual models for (a) laterally translating snowbands, (b) laterally quasi-stationary snowbands, and (c) pivoting snowbands. Features are shown according to keys accompanying each panel; other symbols are conventional. Sense of band motion is shown by grey arrows in (a) and (b). "PZ" in (c) denotes pivot zone location, and encircling grey arrow indicates sense of band rotation. Note that streamlines and frontogenesis are depicted for the 850–700-hPa layer in (a) and (c), but for the 700–500-hPa layer in (b). In each panel, hodographs at locations marked "X" are shown at bottom right, where "S" and "T" correspond to surface and tropopause, respectively.

REFERENCES

Banacos, P. C., 2003: Short range prediction of banded precipitation associated with deformation and frontogenetical forcing. Preprints, *10th Conf. on Mesoscale Processes*, Portland, OR, Amer. Meteor. Soc., P1.7.

Bennetts, D. A., and B. J. Hoskins, 1979: Conditional symmetric instability—A possible explanation for frontal rainbands. *Quart. J. Roy. Meteor. Soc.,* **105,** 945–962.

Carlson, T. N., 1980: Airflow through midlatitude cyclones and the comma cloud pattern. *Mon. Wea. Rev.,* **108,** 1498–1509.

Clark, J. H. E., R. P. James, and R. H. Grumm, 2002: A reexamination of the mechanisms responsible for banded precipitation. *Mon. Wea. Rev.*, **130**, 3074–3086.

desJardins, M. L., K. F. Brill, and S. S. Schotz, 1991: Use of GEMPAK on UNIX workstations. *Proc. Seventh Int. Conf. on Interactive Information and Processing Systems for Meteorology, Oceanography, and Hydrology,* New Orleans, LA, Amer. Meteor. Soc., 449–453.

Doswell, C. A., III, H. E. Brooks, and R. A. Maddox, 1996: Flash flood forecasting: An ingredients based methodology. *Wea. Forecasting,* **11,** 560–581.

Eliassen, A., 1962: On the vertical circulation in frontal zones. *Geophys. Publ*., **24**, 147–160.

Emanuel, K.A., 1985: Frontal circulations in the presence of small moist symmetric stability. *J. Atmos. Sci*., **42**, 1062–1071.

Evans, M. and M. L. Jurewicz, 2009: Correlations between analyses and forecasts of banded heavy snow ingredients and observed snowfall. *Wea. Forecasting*, **24**, 337–350.

Galloway, J. L., 1958: The three front model: Its philosophy, nature, construction and use. *Weather,* **13,** 3–10.

——, 1960: The three front model, the developing depression and the occluding process. *Weather,* **15,** 293–301.

Galarneau, T. J., and D. Keyser, 2008: Use of the nondivergent wind for diagnosing banded precipitation systems. *10th Northeast Regional Operational Workshop,* Albany, NY. [Available at http://cstar.cestm.albany.edu/nrow/nrowx/presentations/GALARNEAU/galarneau.ppt]

Greenstein, M. D., 2006: Mesoscale structure of precipitation regions in northeast winter storms. M.S. thesis, Dept. of Atmospheric and Environmental Sciences, University at Albany, State University of New York, 116 pp.

Houze, R. A. Jr., P. V. Hobbs, K. R. Biswas, and W. M. Davis, 1976: Mesoscale rainbands in extratropical cyclones. *Mon. Wea. Rev*., **104**, 868–879.

Jurewicz, M. L., and M. S. Evans, 2004: A comparison of two banded heavy snowstorms with very different synoptic settings. *Wea. Forecasting*, **19**, 1011–1028.

Keyser, D., M. J. Reeder, and R. J. Reed, 1988: A generalization of Petterssen's frontogenesis function and its relation to the forcing of vertical motion. *Mon. Wea. Rev.,* **116,** 762–780.

Martin, J. E., 1998a: The structure and evolution of a continental winter cyclone. Part I: Frontal structure and the occlusion process. *Mon. Wea. Rev*., **126**, 303–328.

——,1998b: The structure and evolution of a continental winter cyclone. Part II: Frontal forcing of an extreme snow event. *Mon. Wea. Rev*., **126**, 329–348.

Moore, J. T., and T. Lambert, 1993: The use of equivalent potential vorticity to diagnose regions of conditional symmetric instability. *Wea. Forecasting*, **8**, 301–308.

——, C. E. Graves, S. Ng, and J. L. Smith, 2005: A process oriented methodology toward understanding the organization of an extensive mesoscale snowband: A diagnostic case study of 4–5 December 1999. *Wea. Forecasting*, **20**, 35–50.

Nicosia, D. J., and R. H. Grumm, 1999: Mesoscale band formation in three major northeastern United States snowstorms. *Wea. Forecasting*, **14**, 346–368.

Novak, D. R., 2002: A climatological and composite study of cold season banded precipitation in the northeast United States. M.S. thesis, Dept. of Atmospheric and Environmental Sciences, University at Albany, State University of New York, 182 pp.

——, L. F. Bosart, D. Keyser, and J. S. Waldstreicher, 2004: An observational study of cold season banded precipitation in northeast U.S. cyclones. *Wea. Forecasting*, **19**, 993–1010.

——, J. S. Waldstreicher, D. Keyser, and L. F. Bosart, 2006: A forecast strategy for anticipating cold season mesoscale band formation within eastern U.S. cyclones. *Wea. Forecasting*, **21**, 3–23.

——, B. A. Colle, and S. E. Yuter, 2008: A high resolution observational and modeling study of an intense mesoscale snowband over the northeast United States. *Mon. Wea. Rev.*, **136**, 1433–1456.

——, ——, and R. McTaggart-Cowan, 2009: The role of moist processes in the formation and evolution of mesoscale snowbands within the comma head of northeast U.S. cyclones. *Mon. Wea. Rev.*, **137,** 2662–2686.

——, ——, and A. R. Aiyyer, 2010: Evolution of mesoscale precipitation band environments within the comma head of northeast U.S. Cyclones. *Mon. Wea. Rev.*, **138**, 2354–2374.

Sanders, F. and L. F. Bosart, 1985: Mesoscale structure in the megalopolitan snowstorm of 11 12 February 1983. Part I: Frontogenetical forcing and symmetric instability. *J. Atmos. Sci*., **42**, 1050–1061.

Sawyer, J. S., 1956: The vertical circulation at meteorological fronts and its relation to frontogenesis. *Proc. R. Soc. London*, **A234**, 346–362.

Schultz, D. M., 2004: Cold fronts with and without prefrontal wind shifts in the central United States. *Mon. Wea. Rev.*, **132**, 2040–2053.

——, and P. N. Schumacher, 1999: The use and misuse of conditional symmetric instability. *Mon. Wea. Rev*., **127**, 2709–2732.

Seltzer, M. A., R. E. Passarelli, and K. A. Emanuel, 1985: The possible role of symmetric instability in the formation of precipitation bands. *J. Atmos. Sci.*, **42**, 2207–2219.

Stark, D., B. A. Colle, and S. E. Yuter, 2013: Observed microphysical evolution for two East Coast winter storms and the associated snow bands. *Mon. Wea. Rev.*, **141**, 2037–2057.

Thorpe, A. J., and K. A. Emmanuel, 1985: Frontogenesis in the presence of small stability to slantwise convection. *J. Atmos. Sci.,* **42,** 1809–1824.

Xu, Q., 1992: Formation and evolution of frontal rainbands and geostrophic potential vorticity anomalies. *J. Atmos. Sci*., **49**, 629–648.

APPENDIX

Banded Event Catalog

Events outlined in red were excluded from their respective category composite calculations due to their band azimuthal orientations.

LATERALLY TRANSLATING

Date	Time (UTC)	Band centroid location (lat, lon) (°N,°W)	Azimuthal orientation of band at centroid (degrees clockwise from local meridian)	δ (degrees)
28 Feb 2005	1800	39.6, 74.2	110	70
1 Mar 2005	0000	41.4, 71.6	80	80
	0600	43.2, 69.2	60	80
9 Dec 2005	0600	42.4, 75.8	115	70
2 Mar 2007	1200	44.8, 70.0	120	80
16 Dec 2007	1800	45.2, 68.2	110	70
2 Feb 2008	0000	46.4, 66.8	120	90
13 Feb 2008	0600	44.4, 70.8	120	90
	1200	46.2, 67.0	110	70
27 Feb 2008	0000	43.6, 70.2	115	90
	0600	44.8, 67.2	90	90
2 Mar 2008	0000	46.6, 66.8	100	90
21 Dec 2008	1200	43.6, 75.2	120	80
9 Dec 2009	0600	41.0, 74.4	120	80
	1800	45.4, 69.2	120	80
5 Feb 2010	1800	39.8, 80.4	105	80
	1800	38.2, 79.4	120	80
6 Feb 2010	0000	39.6, 75.4	120	80
	0000	38.0, 75.4	125	80
category mean (all bands):			**109**	
category mean (composited bands):			**114**	

LATERALLY QUASI-STATIONARY

Date	Time (UTC)	Band centroid location (lat, lon) (°N,°W)	Azimuthal orientation of band at centroid (degrees clockwise from local meridian)	δ (degrees)
16 Mar 2007	1200	41.4, 73.2	50	< 10
13 Feb 2008	1200	41.0, 80.2	40	< 10
	1200	42.8, 76.6	40	< 10
22 Feb 2008	1800	40.8, 80.4	70	< 10
23 Feb 2008	0000	42.0, 73.8	65	< 10
8 Mar 2008	1200	43.8, 78.2	40	< 10
12 Dec 2008	0600	44.4, 75.2	45	< 10
3 Feb 2009	1200	41.6, 70.4	35	< 10
2 Mar 2009	0600	42.0, 73.0	50	< 10
category mean (all bands):			**48**	
category mean (composited bands):			**46**	

HYBRID

Date	Time (UTC)	Azimuthal orientation of band at centroid (degrees clockwise from local meridian)	δ (degrees)
8 Mar 2005	1800	20	30
6 Dec 2007	0000	60	50
6 Feb 2008	0600	80	30
	1200	90	30
12 Dec 2008	1200	10	40
28 Jan 2009	0600	120	40
2 Mar 2009	1800	10	20

PIVOTING

Date	Time (UTC)	Pivot zone location (lat, lon) (°N,°W)	Azimuthal orientation of band at pivot zone (degrees clockwise from local meridian)
20 Jan 2005	1200	45.8, 68.2	10
	1800	45.8, 67.0	50
22 Jan 2005	1800	43.4, 79.2	75
23 Jan 2005	1200	43.6, 69.2	60
1 Mar 2005	1200	43.8, 71.0	40
9 Dec 2005	1800	43.8, 69.8	55
12 Feb 2006	0600	39.0, 77.4	40
	1200	41.8, 72.8	50
	1800	43.0, 70.8	50
2 Mar 2006	1800	42.6, 74.8	100
14 Feb 2007	1800	42.0, 75.2	35
17 Mar 2007	0600	43.4, 75.8	40
16 Apr 2007	0600	41.0, 76.2	0
14 Jan 2008	1800	44.4, 69.8	40
27 Feb 2008	1200	46.2, 67.2	45
22 Dec 2008	0000	44.6, 71.0	45
23 Feb 2009	0600	45.2, 69.6	50
19 Dec 2009	1200	38.6, 80.2	55
20 Dec 2009	0600	41.4, 72.4	40
	1200	42.8, 71.2	25
6 Feb 2010	0600	41.0, 80.4	105
	1800	40.4, 73.4	75
26 Dec 2010	1800	37.8, 75.6	30
27 Dec 2010	0000	39.6, 74.4	0
	0600	41.2, 74.2	20
	1200	45.0, 70.4	40
category mean (all bands):			**45**
category mean (composited bands):			**44**